

Institute für Ionenstrahlphysik und Materialforschung

Helmholtz-Zentrum Dresden-Rossendorf

**The interplay between localization and magnetism in  
III-Mn-V dilute ferromagnetic semiconductors**

Dissertation

Zur Erlangung des akademischen Grades

Doctor rerum naturalium (Dr. rer. nat.)

Vorgelegt der Fakultät Mathematik und Naturwissenschaften  
der Technischen Universität Dresden

von

Ye Yuan

geboren am 23. 11. 1987 in China

Eingereicht am

Verteidigt am

Gutachter:

1. Prof. Dr. Manfred Helm (TU-Dresden and HZDR)
2. Dr. Shengqiang Zhou (HZDR)

## Acknowledgements

If someone offered me an opportunity to rebuild the past four years, all what I want is just repeating. I am grateful to my past four years' experience. I have to say that a degree is not the most crucial harvest when compared with the patience, skill, and vision which I have obtained from my PhD study. Most importantly, in Dresden, a peaceful life leaves me enough space to explore my mind: What kind of life is my favorite.

I am grateful to my wife. It is her patience leaving a peaceful space for me to finish my PhD work. I would like to thank my daughter. It is her cute face encouraging me to go through every dilemma. I thank my parents. By learning from them, I can understand how important a family is.

I have to show the greatest appreciations to my boss Shengqiang. He is the best leader I have seen in my life. His experience enables me to realize that EQ is as crucial as IQ to one's carrier. As a group leader, he shows that how important patience, humble, and politeness are. Moreover, from him, I learn how to balance my work and life. I would never have such progress without his help to my work and life. Wish him and his family all the best.

I am thankful to my supervisor Prof. Manfred Helm. His helpful discussion and critical comments largely improve my understanding on the topic. His approachability lets me know the necessary condition of being a successful director.

I would like to thank Prof. Maciej Sawicki and Prof. Tomasz Dietl in Warsaw. I am lucky to have such an opportunity to work with two top scientists in the field, and that one month staying in Warsaw is my most valuable experience, encouraging me to follow their trace for the rest of my life.

All my colleagues in HZDR are highly appreciated. I can not finish my work without their help. Thank Dr. Wolfgang Skorupa and all group members, the experience in your department is unforgettable. Thanks for the discussion with Dr. Anna Semisalova and Dr. Slawomir Prucnal. Thanks for the TEM measurements by Dr. Rene Huebner. Thanks for the help from the crew in the ion beam center, particularly Dr. Roman Böttger.

I want to show my appreciations to all my friends in Germany, Yanda, Kun, Chuangui, Yu, Zhitao, Tian, Pengnan, Yonder, Yutian, Hua, Jingyue, Fang, Chi, Mao, Jin, Changan, etc... Taste and colorful life comes from your accompany.

Finally, I would like to thank my past six study years in Harbin Institute of Technology. I thank all the people there, particularly my previous supervisor Prof. You Wang. Your influence is with me all my life.

Actually, this acknowledgement was started to be organized when I began to write this thesis. However, it is the last finished part. The only reason is that I did not know how to fully express my appreciations although I have so many words to say and so many people to thank. But anyway I have to stop now, because time never pauses for anyone.

**See you, my student life...**



# Abstract

III-Mn-V dilute ferromagnetic semiconductors (DFSs) have been treated as a candidate material for semiconductor spintronics due to their intrinsic ferromagnetism mediated by holes.

In this thesis, three different Mn doped III-V DFSs, (In,Mn)As, (Ga,Mn)As, and (Ga,Mn)P, have been produced by ion implantation and pulsed laser melting. The comparison of magnetic anisotropy, magnetization, Curie temperature, as well as the electrical property is performed between three different materials to understand the nature of hole-mediated ferromagnetism in DFSs.

An in-plane magnetic easy axis is observed in (Ga,Mn)As and (Ga,Mn)P, while an out-of-plane magnetic easy axis is found in (In,Mn)As due to the contribution of different inner strain resulting from the lattice mismatch between the DFS layer and the corresponding substrate. Most importantly, the direct proof of interplay between localization and magnetism is provided by a systematic comparison between (Ga,Mn)As and (In,Mn)As. When the Mn concentration is increased in the regime of the insulator-metal transition, the long-range ferromagnetic coupling is gradually built up accompanied with the appearance of metallic features. The generation of long-range global ferromagnetism is strongly influenced by the  $p-d$  coupling between hole and Mn local spins: The global ferromagnetism (metallic feature) happens at lower Mn concentration in (In,Mn)As than in (Ga,Mn)As due to the stronger  $p-d$  coupling from the smaller lattice parameter of GaAs. Moreover, for the case of (Ga,Mn)P with the strongest  $p-d$  coupling in comparison with (In,Mn)As and in (Ga,Mn)As, the super-exchange model has to be considered, since metallic features does not appear at the highest obtainable Mn concentration.

Through the comparison between three different DFS materials, our findings strongly advocate for the heterogeneous model of electronic states at the localization boundary and point to the crucial role of weakly localized holes in mediating efficient spin-spin interactions even on the insulator side of the insulator-metal transition at least for (In,Mn)As and in (Ga,Mn)As.



# Contents

## Chapter 1 Introduction

1.1 Dilute ferromagnetic semiconductors (DFSs).....	4
1.2 Hole-mediated magnetism in DFS.....	5
1.2.1 Zener model.....	5
1.2.2 Super-exchange interaction.....	6
1.3 Mn doped III-V DFSs.....	7
1.3.1 (Ga,Mn)As.....	8
1.3.2 (In,Mn)As.....	10
1.3.3 (Ga,Mn)P.....	12
1.3.4 Some other III-Mn-V DFSs.....	13
1.4 Spin-related phenomena in III-Mn-V DFSs.....	15
1.4.1 Anomalous Hall effect (AHE).....	15
1.4.2 Tunneling magnetoresistance (TMR).....	16
1.4.3 Current-induced spin-transfer and spin-orbit torque.....	18
1.5 Organization of this thesis.....	19

## Chapter 2 Experimental Methods

2.1 Sample preparation.....	22
2.1.1 Ion implantation.....	22
2.1.2 Pulsed laser melting (PLM).....	24
2.2 Physical property measurements.....	25
2.2.1 Magnetic properties measurement: SQUID.....	25
2.2.2 Electrical properties measurement: HMS.....	27
2.2.3 Micro-Raman spectroscopy.....	29

## **Chapter 3**

### **Ferromagnetic (Ga,Mn)P prepared by ion implantation and pulsed laser annealing**

3.1 Introduction.....	31
3.2 Experimental section.....	32
3.3 Results and discussion.....	32
3.3.1 Magnetism.....	32
3.3.2 Magnetic anisotropy.....	33
3.3.3 Electrical behavior.....	34
3.3.4 Raman spectra.....	35
3.4 Conclusion.....	36

## **Chapter 4**

### **Ferromagnetic Mn-implanted GaP: Microstructures vs. magnetic properties**

4.1 Introduction.....	38
4.2 Experimental section.....	39
4.2.1 Sample Preparation.....	39
4.2.2 Sample Characterization.....	39
4.2.3 Magnetic Properties Measurements.....	40
4.3 Results and discussion.....	41
4.3.1 Structures.....	41
4.3.2 Magnetic properties.....	47
4.4 Conclusion.....	51

## **Chapter 5**

### **High $T_C$ and PMA in homo-epitaxial (In,Mn)As films**

5.1 Introduction.....	52
5.2 Experiment section.....	53
5.3 Results and discussion.....	54
5.3.1 Magnetism.....	54
5.3.2 Magnetic anisotropy.....	56
5.3.3 Structures.....	58
5.3.4 X-ray magnetic circular dichroism (XMCD) .....	59
5.4 Conclusion.....	60



## **Chapter 6**

### **Interplay between magnetization and localization in (Ga,Mn)As and (In,Mn)As**

6.1 Introduction.....	62
6.2 Methods.....	63
6.3 Results.....	64
6.4 Discussion.....	77

## **Chapter 7**

### **Summary and outlook**

7.1 Summary.....	78
7.2 Outlook.....	79

<b>Bibliography.....</b>	<b>82</b>
--------------------------	-----------

<b>Appendix A .....</b>	<b>93</b>
-------------------------	-----------

<b>Appendix B.....</b>	<b>96</b>
------------------------	-----------



# Chapter 1

## Introduction

### 1.1 Dilute ferromagnetic semiconductors (DFSs)

It has been a long dream to implement both the spin and charge properties of electron simultaneously in semiconductor devices. For this purpose, ferromagnetic semiconductors are proposed to act the basis materials. The naturally existing ferromagnetic semiconductors are a kind of compounds, in which either rare earth or transition metal ions are periodically arranged in the lattices as cation ions, as shown in Fig. 1.1(A). The example includes EuO, CrCd<sub>2</sub>S<sub>4</sub>, etc [1, 2]. When semiconductors, *e.g.* the IV group, III-V group, and oxide semiconductors, are substitutionally doped with 3*d* magnetic elements, and if the properties of ferromagnets and semiconductors are simultaneously achieved, the resulting new kind of materials is called dilute ferromagnetic semiconductors (DFS) (shown in Fig. 1.1(B)). In DFS, the doped local spins are very dilute (generally only several percents in the semiconductor) and randomly distributed. In this case, the coupling between “dilute” spins which are far from each other is achieved by long-range coupling between local spins and holes: The *p-d* coupling results in the ferromagnetism in DFSs. In order to distinguish the two kinds of ferromagnetic semiconductors shown in Fig. 1.1(A) and (B), the case of Fig. 1.1(A) is also referred as normal ferromagnetic semiconductor [2].

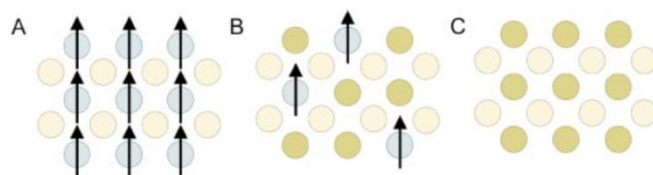


Fig. 1.1 Three types of semiconductors: (A) a ferromagnetic semiconductor, in which a periodic array of magnetic element is present; (B) a diluted ferromagnetic semiconductor, an alloy between nonmagnetic semiconductor and magnetic element; (C) a nonmagnetic semiconductor, which contains no magnetic ions. Taken from Ref. [3].

During the past two decades, DFSs have attracted sizable attention due to their application potential in spintronic devices. The persistence of spin-related phenomena, *e.g.* anomalous Hall effect (AHE) [4, 5], anisotropic magnetoresistance (AMR) [6-9],

as well as current induced spin-transfer torque (STT) [10, 11] and spin-orbit torque (SOT), allows for conceiving different prototype spintronic devices. In addition, the manipulation of ferromagnetism by electrical operation, *e.g.* electrical field induced magnetic anisotropy switching [12] and controlling magnetization by a gating voltage [13], lightens an avenue to new magneto-resistive random access memory (M-RAM).

## 1.2 Hole-mediated magnetism in DFS

Due to the large distance between substitutional transition metal atoms in DFS, free carriers are particularly needed to establish the “communication” between local spins. The *p-d* hybridization between the *d* orbital in doped *3d* element and the *p* orbital holes in semiconductors builds the effective magnetic coupling, thus, holes are always treated as a crucial element for long-range magnetic mediation in DFS [14, 15]. This has been proven in (Zn,Mn)Te that undoped (Zn,Mn)Te is antiferromagnetic and *p*-type (Zn,Mn)Te is ferromagnetic with a Curie temperature  $T_C \sim 2.4$  K [15]. Moreover, the *n*-type (In,Mn)As only exhibits paramagnetic features, proving that the *s-d* exchange interaction between Mn local spins and conduction electrons is far from sufficient to establish long-range ferromagnetic coupling. Although in recent years the *n*-type DFS (In,Fe)As has been claimed by Tanaka *et.al.* [16-20], the ferromagnetism from Fe-rich clusters in the layer cannot be excluded.

### 1.2.1 Zener model

On the basis of the mean-field approximation, the Zener model was firstly proposed by Zener in 1950s to note the role of band carriers in promoting ferromagnetic order between localized spins in magnetic metals: When a *sp* band is partly filled by carriers but the electrons in the open magnetic shells remain localized, the *sp-d* interaction causes the appearance of spin-polarized clouds around each localized spins, thus, ferromagnetic order emerges when all carrier spins assume the same direction [21] in order to lower the carrier energy. In 2000, this model was reformulated by Dietl *et al.* [14, 22] to interpret the ferromagnetism in DFSs. It turned out to be successful in understanding many properties of (Ga,Mn)As, *e.g.* the Curie temperature dependence on the Mn concentration, the magnetic anisotropy, and the interplay between hole localization and magnetization. The reformulated model describes how the Ginzburg-Landau free-energy function ( $F$ ) depends on the magnetization  $M$  of the localized spins [22]. The system total free energy  $F$  strongly depends on both carrier concentration and local spins. Thus, the  $F$  could divide into two contributed energies from carrier concentration  $F_C$  and local spins  $F_S$ . By minimizing  $F[M]=F_C[M]+F_S[M]$  with respect to  $M$  at a given temperature, magnetic field, and hole concentration, one obtains  $M(T, H)$  as a solution of the mean-field equation:

$$M = \mu_g \mu_B S N_0 x_{eff} B_S \left[ \frac{g \mu_B (-\frac{\partial F_C[M]}{\partial M} + H)}{k_B (T + T_{AF})} \right] \quad 1.1$$

and

$$T_C = \frac{x_{eff} N_0 S(S+1) \beta^2 A_F \rho_S(T_C)}{12 k_B} - T_{AF} \quad 1.2$$

where  $\mu_g$  is the Landé g-factor,  $\mu_B$  is the Bohr magneton,  $S$  is the local spins,  $x_{eff} N_0$  is the effective spin concentration,  $B_S(x)$  is the Brillouin function,  $F_C(M)$  is the carrier concentration contributed energy,  $k_B$  is the Boltzmann constant,  $H$  is the magnetic field,  $M$  is the magnetization,  $T_{AF}$  presents the antiferromagnetic interaction,  $T_C$  is the Curie temperature,  $\rho_S$  is the spin density-of-states,  $A_F$  is the Fermi-liquid parameter, and  $\beta$  is the exchange energy. The calculated results from the Zener model outstandingly match the experimental data of both (Ga,Mn)As and (Zn,Mn)Te as displayed in Fig.1.2, particularly for  $T_C$  and magnetization [14].

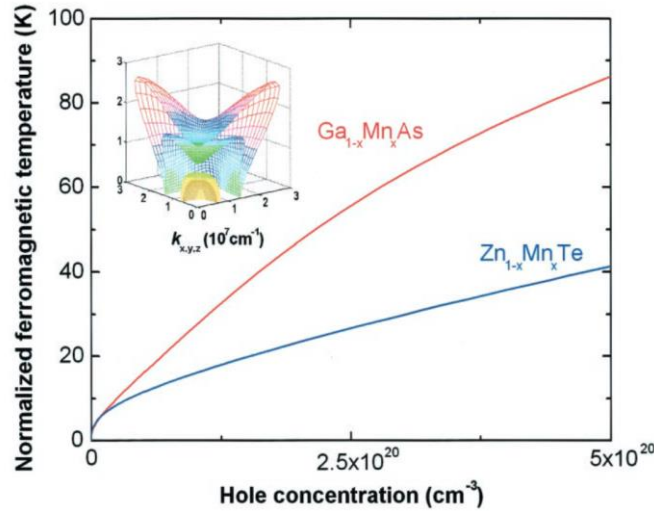


Fig. 1.2 The dependence of hole concentration vs. Curie temperature of (Ga,Mn)As and (Zn,Mn)Te, which was calculated by the Zener model. Taken from Ref. [14].

In addition, the Zener model quantitatively predicts the inner-strain induced uniaxial magnetic anisotropies in different DFSs: The confinement of strain induced anisotropy of the valence band leads to a great anisotropy of spin properties including magnetization and magneto-transport, which have been proven by many groups [23-27].

## 1.2.2 Super-exchange interaction

Although the Zener model successfully explains the ferromagnetism in metallic DFS, the appearance of the ferromagnetism in insulating DFS indicates that the

ferromagnetism is not always related to the presence of itinerant carriers, such as is the case in (Ga,Mn)N [28].

Due to the  $sp-d$  exchange interaction, the electrons in the valence band will get attracted or repulsed by adjacent magnetic ions, resulting in a spatial redistribution of spin-down or spin-up electrons in the valence band. In this case, the system energy arrives at a minimum value through antiferromagnetic coupling among neighbor localized spins, which is known as the short range super-exchange interaction. According to Anderson-Goodenough-Kanamori rules [29], ferromagnetic super-exchange appears in the case of certain charge states of transition-metal ions and bond arrangement. Taking (Zn,Cr)Se and (Zn,Cr)Te [30, 31] as examples, according to a tight-binding approximation, the ferromagnetic super-exchange dominates where  $\text{Cr}^{2+}$  ions are in a tetrahedral environment. Moreover, analogous to  $\text{Cr}^{2+}$ , the ferromagnetic coupling between Mn spins in insulating (Ga,Mn)N was also found dominated by the super-exchange interaction, according to a finding of Mn concentration dependent relation  $T_C(x) \sim x^{2.2 \pm 0.2}$  [32].

### 1.3 Mn doped III-V DFSs

When Mn atoms substitute trivalent III atoms in III-V semiconductors, they always present a +2 valence state, thus bring a hole into the system. By considering that the electron configuration of single Mn atom is  $[\text{Ar}]3d^54s^2$ , the doped Mn ion may present two configurations: (1)  $d^4$  or (2)  $d^5$  plus a weakly bound hole ( $d^5 + h$ ). These different configurations are related with different mechanisms of carrier-mediated ferromagnetism and are largely influenced by various III-V host physical parameters. As shown in Fig. 1.3, different physical properties in various III-V hosts, *e.g.*, the lattice constant, the band gap energy, as well as the Mn binding energy, result in distinct electronic configurations and magnetic behaviors in various III-Mn-V DFSs. For antimonides and arsenides, substitutional Mn atoms always act as effective mass acceptors ( $d^5 + h$ ). Differently, the strong  $p-d$  coupling between holes and Mn local spins in GaP and GaN results in a state of  $d^4$  rather than ( $d^5 + h$ ) [33]. Moreover, different inner strains resulting from the lattice mismatch between III-Mn-V DFS layer and the substrate used lead to the distinct magnetic anisotropies, *e.g.* the in-plane direction in (Ga,Mn)As and (Ga,Mn)P forms magnetic easy axis, however the same axis is the magnetic hard axis in (In,Mn)As. Therefore, it is useful to approach the DFS physics through comparing electrical and magnetic properties in various III-Mn-V DFSs.

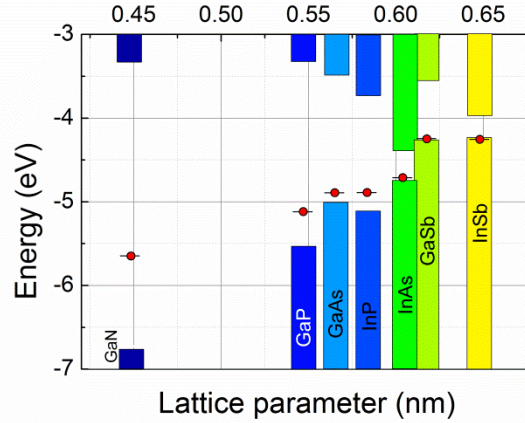


Fig. 1.3 Physical properties of various III-Mn-V DFSSs, including lattice parameter, Mn binding energy, and band gap energy. Bars are energy values of conduction and valence bands, and points are Mn impurity energy levels in different III-V semiconductors.

### 1.3.1 (Ga,Mn)As

As the mostly studied Mn doped III-V DFSSs in last two decades, (Ga,Mn)As is granted the most representative role in the III-Mn-V DFS family. The non-equilibrium growth by low-temperature molecular beam epitaxy (LT-MBE) allows that the doped Mn concentration is far beyond the Mn solubility in GaAs. The anomalous Hall effect curve outstandingly fits the result of field dependent magnetization, directly proving the ferromagnetism mediated by carriers. Interestingly, ferromagnetism is observed in both insulating and metallic samples, and two models have been proposed to explain the origin of hole mediated ferromagnetism in (Ga,Mn)As.

(1) The isolated Mn impurity model: Holes are believed to reside in a Mn-derived impurity band separated from the valence band even for samples with high Mn concentration, and thus impurity band holes are mainly in charge of the ferromagnetism-mediation through double exchange interaction [34-39]. In this case, the maximal Curie temperature is obtained when the Fermi level is located in the middle of the Mn impurity band.

(2) The valence band hole model, also referred as the Zener model: The Mn impurity band merges with the valence band of the GaAs host when the Mn concentration is higher than 1%, and ferromagnetism is mediated by valence band holes via long-range RKKY coupling [14, 40-43]. Different from the double exchange mechanism, the deeper the Fermi level is located in the valence band, the higher Curie temperature is achieved.

Accordingly, plenty of experiments were performed to verify one of the above-mentioned two models, of which a very fascinating work was done by Sawicki *et al.* [13]. In their work shown in Fig. 1.4, by electrical gating operation, the hole

injection and depletion in (Ga,Mn)As directly cause the a transition between global ferromagnetic and superparamagnetic phases, demonstrating the crucial role of itinerant holes for mediating ferromagnetism. This result definitively gives a strong proof to support the Zener model, particularly in the regime of the insulator-metal transition. However, Dobrowolska *et al.* [39] performed another work and they changed the effective Mn concentrations and systematically investigated the magnetic properties by magnetic circular dichroism (MCD). They found that the maximal  $T_C$  was not achieved in the sample which has the lowest compensation, *i.e.* when the hole concentration is equal to the Mn concentration. Instead, when the ratio between the hole concentration and effective Mn concentration approached 0.71, the highest  $T_C$  of 90 K was obtained as shown in Tab. 1.1, this suggests that the maximal  $T_C$  appears only when the Fermi level is located near the center of the isolated Mn impurity band. Dobrowolska *et al.* [39] draw a conclusion in contradiction with the  $p$ - $d$  exchange Zener mechanism: The location of the Fermi level within the impurity band plays a crucial role in determining  $T_C$  through the variation of the density of states at the Fermi level [39], although it was commented by Edmonds *et al.* [44]. Interestingly, it is worth mentioning that by using hard X-ray angle resolved photoemission spectroscopy (HARPES), an intuitive band structure is drawn for (Ga,Mn)As. The results suggested that the ferromagnetism in (Ga,Mn)As must be considered to arise from both  $p$ - $d$  exchange and double exchange, thus providing a more diplomatic picture for this controversial material [45].

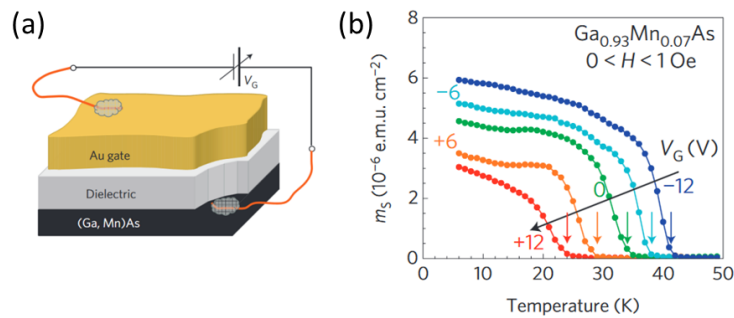


Fig. 1.4 Magnetic properties of (Ga,Mn)As are modified by an electric gating voltage in a (a) metal-insulator-semiconductor structure. (b) Both magnetization and Curie temperature are manipulated by the bias electric gating. The result provided a strong evidence for the crucial role of itinerant valence-band holes in mediating ferromagnetism in (Ga,Mn)As. Taken from Ref. [13].



Sample	$x_{\text{tot}}$ (%)	$x_{\text{random}}$ (%)	$x_{\text{sub}}$ (%)	$x_{\text{i}}$ (%)	$x_{\text{eff}}$ (%)	$T_{\text{C}}$ (K)	$p$ ( $10^{20}$ cm $^{-3}$ )	$p/N_{\text{Mn}}^{\text{eff}}$ or $f$
A (as grown)	3.0	0.1	2.4	0.5	1.9	45	3.1	0.74
B (as grown)	3.5	0.1	3.2	0.2	3.0	27	6.2	0.93
C (as grown)	4.8	0.3	4.0	0.5	3.5	34	6.6	0.86
C* (annealed)	5.0	0.4	4.3	0.3	4.0	54	8.2	0.93
D (as grown)	5.8	0.3	5.0	0.5	4.5	26	8.8	0.90
D* (annealed)	5.9	0.4	5.3	0.2	5.1	42	10.8	0.96
E (as grown)	6.0	0.3	5.0	0.7	4.3	30	8.0	0.84
E* (annealed)	6.1	0.5	5.2	0.4	4.8	43	9.7	0.92
F (as grown)	6.4	0.5	4.2	1.7	2.5	40	1.8	0.32
F* (annealed)	6.8	1.3	4.5	1.0	3.5	90	5.5	0.71

Tab. 1.1 The location of Mn sites in the lattice was determined by simultaneous  $c$ -PIXE and  $c$ -RBS. Here  $x_{\text{tot}}$  indicates the total Mn concentration;  $x_{\text{random}}$  the concentration of Mn atoms residing at random locations, for example, MnAs inclusions;  $x_{\text{sub}}$  the concentration of Mn ions located at Ga sites ( $\text{Mn}_{\text{Ga}}$ ); and  $x_{\text{i}}$  the concentration of Mn ions located at interstitial sites ( $\text{Mn}_{\text{i}}$ ). The quality  $x_{\text{eff}} = x_{\text{sub}} - x_{\text{i}}$  is the concentration of Mn ions which contributes to ferromagnetic order. The hole concentration  $p$  for a given sample was found as  $p = 4(x_{\text{sub}} - 2x_{\text{i}})/a^3$ , where  $a$  is the lattice constant of (Ga,Mn)As. The Curie temperature  $T_{\text{C}}$  is determined from magnetization measurements versus temperature. Finally,  $p/N_{\text{Mn}}^{\text{eff}}$  is the number of holes per effective Mn moment  $N_{\text{Mn}}^{\text{eff}} = 4(x_{\text{eff}})/a^3$  [39]. The experimental results suggests that the maximal  $T_{\text{C}}$  appears when  $p/N_{\text{Mn}}^{\text{eff}}$  is approaching 0.71, matching the prediction by double exchange mechanism. Taken from Ref. [39].

From the application point of view, the reason why (Ga,Mn)As is attractive is that it has the highest reported Curie temperature ( $T_{\text{C}}$ ) of Mn based III-V DFSs, thus it has a large potential for a spintronic device. A  $T_{\text{C}}$  above 100 K was predicted by the Zener model and was also proven by many experimental groups [14]. In the beginning, due to the existence of a large amount of Mn interstitials and Ga antisites which act as donors and compensate holes, the  $T_{\text{C}}$  was much lower than the predicated value [3]. Afterwards, the long-time low-temperature annealing has been found to effectively out-diffuse Mn interstitials in as-grown (Ga,Mn)As samples, largely enhancing the  $T_{\text{C}}$  even to a value as high as 188 K [46-48].

In addition, some spin-related effects render (Ga,Mn)As a favorable test-bed for spintronic devices. The manipulation of magnetic behavior by an electrical field, *e.g.* magnetic moment [13], magnetization vector [12], and damping constant [49], shows possible avenues for switching logical states. The current-induced spin-orbit torque [50] and spin-transfer torque [51, 52] in patterned (Ga,Mn)As are regarded as a key point to achieve current writing in spintronic devices.

### 1.3.2 (In,Mn)As

Although being the firstly realized Mn doped III-V DFS, (In,Mn)As has not attracted attentions as much as (Ga,Mn)As. However, the advantages of high carrier mobility and the possible out-of-plane direction uniaxial magnetic anisotropy still allow it as a candidate material for spintronic devices, particularly for a device with vertical multi-layer structure [53].

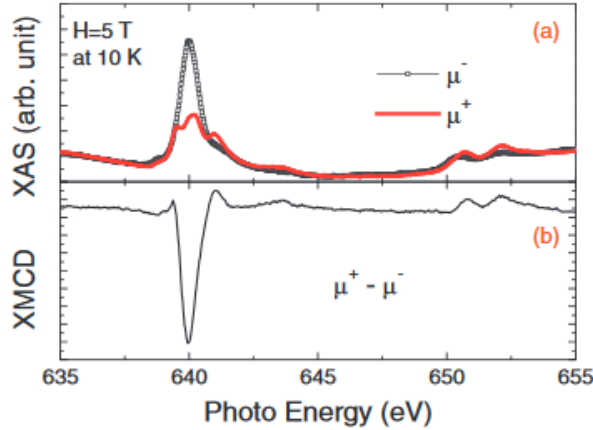


Fig. 1.5 XAS/XMCD spectra of Mn  $L_{3,2}$  in (In,Mn)As. (a) XAS for magnetization and helicity parallel ( $\mu^+$ ) and antiparallel ( $\mu^-$ ) and (b) XMCD ( $\mu^+ - \mu^-$ ) for (In,Mn)As measured at around 10 K under an external field of 5 T applied perpendicular to the surface. Taken from Ref. [54].

The initial approach to obtain (In,Mn)As DFS was low-temperature molecular beam epitaxy (LT-MBE). However, during the epitaxial growth by LT-MBE, the slight lattice mismatch between the grown (In,Mn)As layer and the GaSb substrate results in a large amount of  $n$ -type defects. These defects act as donors and compensate itinerant holes in the (In,Mn)As layer, strongly suppressing the magnetization and  $T_C$  [55]. By carefully selecting a buffer layer,  $n$ -type defects were effectively eliminated and a  $T_C$  as high as 90 K was achieved in (In,Mn)As [56]. Meanwhile, due to the relaxation of the inner strain between the (In,Mn)As layer and the substrate, the perpendicular magnetic anisotropy of (In,Mn)As was lost. To date, for LT-MBE prepared (In,Mn)As with perpendicular magnetic anisotropy, the record Curie temperature is 72 K when the Mn concentration reaches 10% by using an AlSb buffer layer [56]. It is worth mentioning that (In,Mn)As prepared by ion implantation and pulsed laser melting spontaneously exhibits a high  $T_C$  of 82 K and perpendicular magnetic anisotropy, demonstrating the minimized  $n$ -type defects in (In,Mn)As prepared by this method [54, 57]. Figure 1.5 shows an X-ray absorption spectrum (XAS) / X-ray magnetic circular dichroism (XMCD) signal of ferromagnetic (In,Mn)As prepared by implantation, indicating that the ferromagnetism originates from the Mn L edge. In addition, some other methods are possible to produce (In,Mn)As material, *e.g.* (In,Mn)As dots were obtained by metal-organic vapour phase epitaxy (MOVPE) on high-index surfaces [58].

### 1.3.3 (Ga,Mn)P

Compared with GaAs ( $E_g=1.42$  eV) and InAs ( $E_g=0.35$  eV), GaP exhibits a larger band gap of 2.26 eV and a much larger Mn binding energy of 400 meV above the valence band top, leading to a separated Mn impurity band existing in the band gap [59]. Thus, (Ga,Mn)P is quite different from (Ga,Mn)As whose ferromagnetism is mediated by valence band holes, which enables the new discussion about the hole-mediated ferromagnetism mechanism in DFSs. To date, Mn doped GaP DFS has only been prepared by ion implantation and subsequently pulsed laser melting. After the first preparation of (Ga,Mn)P, Scarpulla *et al.* [59] presented the detached Mn impurity band structure and observed that the hopping mechanism is mainly responsible for the electrical conduction as shown in Fig. 1.6. Due to the absence of itinerant valence band holes, impurity band holes effectively couple with magnetic moments through hopping conduction, resulting in ferromagnetism in insulating (Ga,Mn)P [60]. Interestingly, it seems that the localized-hole-mediated ferromagnetism in (Ga,Mn)P acts as a challenge to the  $p$ - $d$  Zener model. Actually, due to much stronger  $p$ - $d$  coupling in (Ga,Mn)P than in (Ga,Mn)As and (In,Mn)As, the super-exchange mechanism is taking the place of the Zener model to explain the ferromagnetism mechanism.

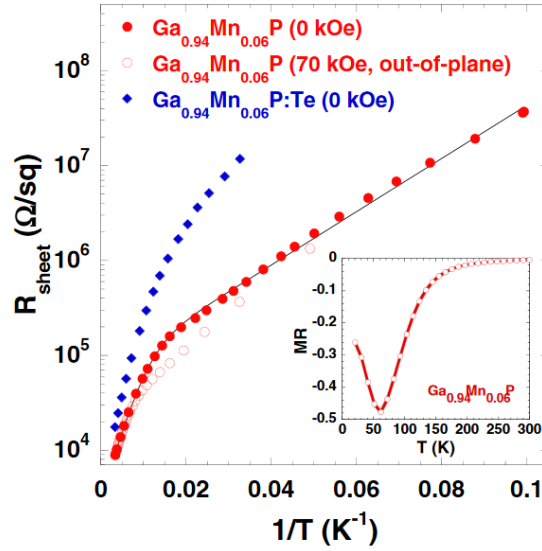


Fig. 1.6 Hopping conduction is responsible for the electric conducting in (Ga,Mn)P. Sheet resistivity ( $R_{\text{sheet}}$ ) versus inverse temperature in zero-field for  $\text{Ga}_{0.94}\text{Mn}_{0.06}\text{P}$  (solid circles) and Te co-compensated  $\text{Ga}_{0.94}\text{Mn}_{0.06}\text{P}$  (solid diamonds) as well as for  $\text{Ga}_{0.94}\text{Mn}_{0.06}\text{P}$  at 70 kOe (open circles). (Inset) Magnetoresistance between 70 and 0 kOe for  $\text{Ga}_{0.94}\text{Mn}_{0.06}\text{P}$  as a function of temperature. Taken from Ref. [59].

It is worth mentioning that like some other functional materials, the micro- and nano-structure strongly influences the physical properties of (Ga,Mn)P. By applying

different laser energies to Mn implanted GaP samples, the uniaxial magnetic anisotropy and Curie temperature are carefully tuned through manipulating the ratio between epitaxial single crystalline and polycrystalline phases [43], which will be discussed in Chapter 4.

### 1.3.4 Some other III-Mn-V DFSs

In addition to the above-mentioned three Mn doped III-V DFSs, some other DFS materials, *e.g.* (Ga,Mn)N [58, 61-63], (In,Mn)Sb [64-67], and (In,Mn)P [68], are also of great importance and are attractive to present various physics in DFSs.

According to the Zener model calculation, a  $T_C$  above room temperature is predicted in 5% Mn doped GaN providing a hole concentration of  $3.5 \times 10^{20} / \text{cm}^3$ , thus attracting great attention [14]. Extensive nano-characterization of (Ga,Mn)N which was prepared by MOVPE [69] and MBE [62, 63] shows that by carefully adjusting growth conditions, all Mn (below 10%) ions are randomly distributed at the substitutional sites. However, even for such good quality (Ga,Mn)N samples, the  $T_C$  obtained from subsequent experimental results strongly conflicts the theoretical predicted value. This distinction has raised a lot of questions about the *p-d* Zener model. Interestingly, according to the magnetic phase diagram displayed in Fig. 1.7, a dependence of  $T_C(x) \sim x^m$ , where  $m=2.2$  is observed. The same value of  $m$  was observed for spin-glass freezing in II-VI DFSs, suggesting that the super-exchange interaction instead of the *p-d* Zener mechanism dominates the spin-spin coupling mechanism in (Ga,Mn)N [28]. The route of the super-exchange interaction in (Ga,Mn)N is from a strong *p-d* coupling between the Mn open *d* orbital and a hole from the As *p* orbital.

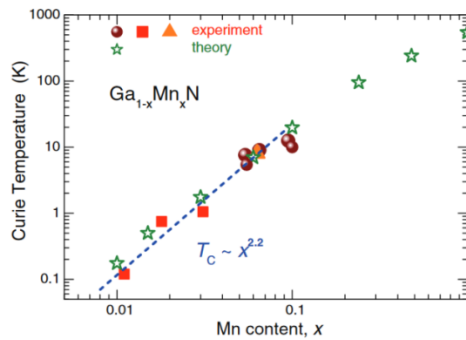


Fig. 1.7 The super-exchange interaction enables ferromagnetism in (Ga,Mn)N. Experimental  $T_C$  of (Ga,Mn)N as a function of Mn content  $x$  (circles), together with the experimental result of Refs. [62] and [32] (squares and triangle, respectively). The dotted line indicates the scaling dependence  $T_C \propto x^m$  with  $m=2.2$ . Results of Monte Carlo simulations with exchange integrals from the tight-binding model (stars) are also shown. Taken from Ref. [28].

Due to its band gap (1.34 eV) being close to that of GaAs (1.42 eV) and a Mn-acceptor level at an energy 220 meV above the valence band [70], InP is regarded

as another candidate for DFSs. Dietl *et al.* have predicted theoretically that Mn-doped InP is DFS with a Curie temperature of  $\sim 50$  K, in which 5% of indium atoms are randomly substituted by Mn [14]. Similar as for (Ga,Mn)P, the preparation of (In,Mn)P is a great challenge for LT-MBE, however, it is possible by ion implantation and subsequent pulsed laser melting [68, 71]. When the Mn concentration approaches 5% in (In,Mn)P, an isolated Mn impurity band is found still detached from the InP valence band, thus the electrical transport is resulting from hopping conduction. Therefore, (In,Mn)P exhibits both similar conduction behavior and mechanism for hole-mediated ferromagnetism as (Ga,Mn)P. The results from SQUID (shown in Fig. 1.8) and XMCD show that a  $T_C$  of 40 K is measured in 5% Mn doped (In,Mn)P. Interestingly, this detected  $T_C$  is quite close to the predicted value from the Zener model, even though (In,Mn)P has a different ferromagnetic coupling mechanism from the Zener model prediction. For the ferromagnetic properties, (In,Mn)P exhibits a perpendicular magnetic easy axis, similar for (In,Mn)As on InAs substrate. This is due to the fact that both materials experience a compressive strain resulting from the InP and the InAs substrate, respectively.

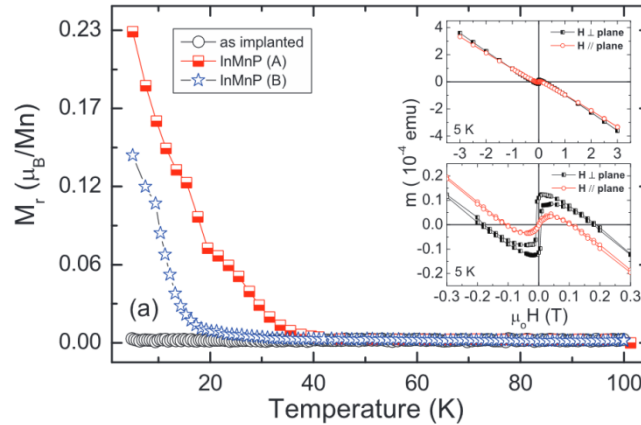


Fig. 1.8 Ferromagnetic (In,Mn)P prepared by ion implantation and subsequent pulsed laser annealing. Remnant magnetization vs temperature for an as-implanted sample and two laser annealed (In,Mn)P with Mn concentration  $x$  of 2.5 and 5%. The inset shows the magnetization of laser annealed  $x=5\%$  sample in magnetic field ranges  $\pm 3$  and  $\pm 0.3$  T applied parallel and perpendicular to the sample plane. Taken from Ref. [68].

In addition to the above-mentioned two DFSs, another attractive DFS is attractive is (In,Mn)Sb. The Fermi level residing in the valence band and the narrow band gap of the InSb host render (In,Mn)Sb an ideal candidate for spintronic devices. (In,Mn)Sb films are usually grown on InSb buffers by MBE. A Curie temperature of 8 K was observed when the Mn concentration is 2.8% [72]. Moreover, as shown in Fig. 1.9, the magnetic field dependence of magnetization and anomalous Hall effect reveal a convincing nature of spin-polarized hole mediated ferromagnetism in (In,Mn)Sb [73,

74]. Importantly, according to a result from Furdyna *et al.*, when more pressure is applied on the (In,Mn)Sb sample, the magnetization is strongly modified as shown in Fig. 1.9 [75]. This work shows that the pressure modified magnetization is also possible in DFSs.

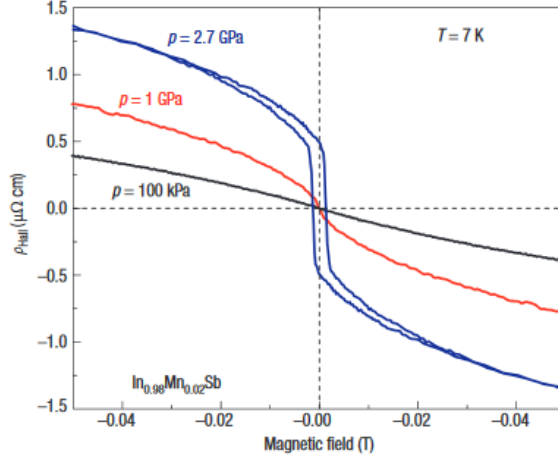


Fig. 1.9 Hall resistivity as a function of magnetic field taken at several hydrostatic pressures in  $\text{In}_{0.98}\text{Mn}_{0.02}\text{Sb}$ . Taken from Ref. [75].

## 1.4 Spin-related phenomena in DFSs

On the basis of the interaction between spin and electrical current, fruitful spin-related phenomena in III-Mn-V DFSs offer a broad platform to achieve various prototype spintronic devices, particularly compatible with current semiconductor devices. Therefore, it would be crucial to pay attention to these in-depth investigations on the spin-electric current interaction to understand and develop novel devices. In this section, a brief review will be given based on four different aspects, including anomalous Hall effect (AHE), tunneling magnetoresistance, as well as current-induced spin-transfer and spin-orbit torque.

### 1.4.1 Anomalous Hall effect (AHE)

The anomalous Hall effect (AHE) occurs in solids with broken time-reversal symmetry, typically in a ferromagnetic phase, as a consequence of spin-orbit coupling. In ferromagnets, the Hall resistivity  $\rho_{xy}$  initially increases steeply in weak  $H_z$  (the magnetic field along the out-of-plane direction), but saturates at a large value which is nearly  $H_z$ -independent. The experiments by Pugh and coworkers established that an empirical relation between  $\rho_{xy}$ ,  $H_z$ , and  $M_z$ ,

$$\rho_{xy} = R_0 H_z + R_s M_z$$

applies to many materials including III-Mn-V DFSs (see Fig. 1.10) over a broad range of external magnetic fields. The second term represents the Hall effect contribution

due to the spontaneous magnetization, referred as anomalous Hall effect. Unlike the ordinary Hall coefficient  $R_0$ , which has been already understood to depend mainly on the density of carriers, the anomalous Hall coefficient  $R_s$  was found to depend subtly on a variety of material specific parameters and, in particular, on the longitudinal resistivity  $\rho_{xx}$ .

III-Mn-V based DFSs, particularly (Ga,Mn)As, have become a favorable test-bed for the investigation of the AHE. Here the unique position of III-Mn-V DFSs stems from the strongly spin-orbit coupled and exchange-split carrier bands. Here, we mainly take (Ga,Mn)As as an example. The principles of the microscopic description of the AHE in the metallic (Ga,Mn)As materials, based on the scattering-independent intrinsic mechanism, have been successful to explain the effect in other itinerant ferromagnets. Experimentally, a line of research has been prompted by AHE in the heavily doped metallic (Ga,Mn)As [4, 76-78]. As shown in Fig.1.10, the positive slope of the Hall effect in the large field regime in (In,Mn)As indicates a hole-conduction nature. The square-like hysteresis loops below the Curie temperature result from the interaction between spin-polarized holes and ordered ferromagnetic moments. Expectedly, when the temperature increases above the Curie temperature, the hysteresis loop disappears, indicating that the highly ordered magnetic moments are disturbed by the thermal fluctuation.

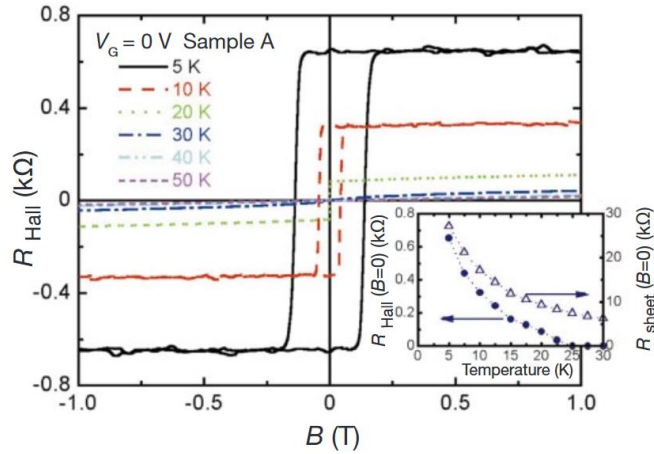


Fig.1.10 Magnetic-field dependence of the sheet Hall resistance  $R_{Hall}$  proportional to the magnetization of the magnetic semiconductor layer in (In,Mn)As. Clear hysteresis observed at  $T = 20$  K is evidence of ferromagnetism. Inset, the temperature dependence of the remanence of  $R_{Hall}$  (solid circles), showing that the ferromagnetic transition temperature  $T_C$  is above 20 K. Open circles indicate the channel sheet resistance  $R_{sheet}$  at zero field, which shows moderate negative T-dependence. Taken from Ref. [53].

## 1.4.2 Tunneling magnetoresistance (TMR)

The electrical response to changes in the magnetic state is strongly enhanced in layered structures consisting of alternating ferromagnetic and nonmagnetic materials. The giant magnetoresistance (GMR) and tunneling magnetoresistance (TMR) effects

which are widely exploited in metal spintronic technologies reflect the large difference between resistivity in configurations with parallel and antiparallel polarization of ferromagnetic layers in magnetic multilayers, or trilayers like spin valves and magnetic tunnel junctions [79, 80]. In DFSs, functional magnetic tunnel junction devices can be also fabricated, as proven by the measured large TMR effects [7, 11, 81-85]. Among various TMR devices, a device based on the combination of anisotropic magnetoresistance (AMR) and TMR is called tunneling anisotropic magnetoresistance (TAMR) device, opening a fresh avenue for spintronic device [9, 84, 86-88].

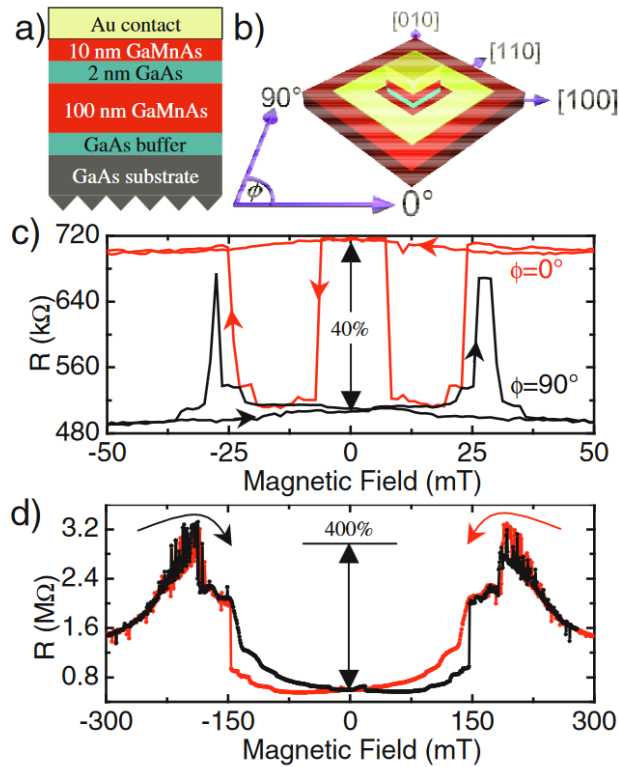


Fig. 1.11 (a) Layer stack and (b) sample layout of (Ga,Mn)As based TAMR spintronic device. (c) 4 K magnetoresistance near each in-plane easy axis showing both positive and negative 40% effects. (d) 4 K magnetoresistance in perpendicular field showing a 400% signal. Taken from Ref. [88].

As shown in Fig. 1.11, a TAMR spintronic device based on (Ga,Mn)As DFS was fabricated by LT-MBE [88]. A 2 nm GaAs tunneling layer was fabricated between two (Ga,Mn)As electrodes. When the magnetic field was scanned between positive and negative sides, a TMR of 40% was observed when the field was applied parallel with the in-plane direction. However, a much larger TMR, as high as 400%, was achieved when the field was put along the out-of-plane direction. Moreover, four key novel spintronic features of this device are achieved as follows: (i) both normal and inverted spin-valve-like signals; (ii) a large non-hysteretic magnetoresistance for magnetic fields perpendicular to the interfaces; (iii) magnetization orientations for extremal



resistance are, in general, not aligned with the magnetic easy and hard axis; (iv) the enormous amplification of the effect at low bias and temperatures. Therefore, similar as in ferromagnetic metals, the TMR effect provides an option for the DFS application in spintronic devices.

### 1.4.3 Current-induced spin-transfer and spin-orbit torque

When spin-polarized carriers are injected into a magnetic region whose moments are misaligned with the injected spin polarization of the carriers, a spin transfer torque (STT) can act on the magnetic moments and align them on purpose. The phenomenon belongs to an important area of spintronic research. It provides a mean for manipulating magnetization by electrical currents and is treated as the basis of the emerging technologies for scalable MRAMs. In III-Mn-V DFS, take (Ga,Mn)As as an example, together with the high degree of spin polarization of carriers it implies that the electrical currents required to excite magnetization by STT are also comparatively low. According to the theory prediction [89], STT induced switching could be obtained at a current density of the order  $10^4 \sim 10^5$  A cm<sup>-2</sup> in magnetic tunnel junctions with (Ga,Mn)As electrodes [82], which is 1-2 orders magnitude lower than in common dense-moment metal ferromagnets. Another example is experimentally provided by a tensile-strained (Ga,Mn)(As,P) sample with perpendicular magnetic easy axis [90].

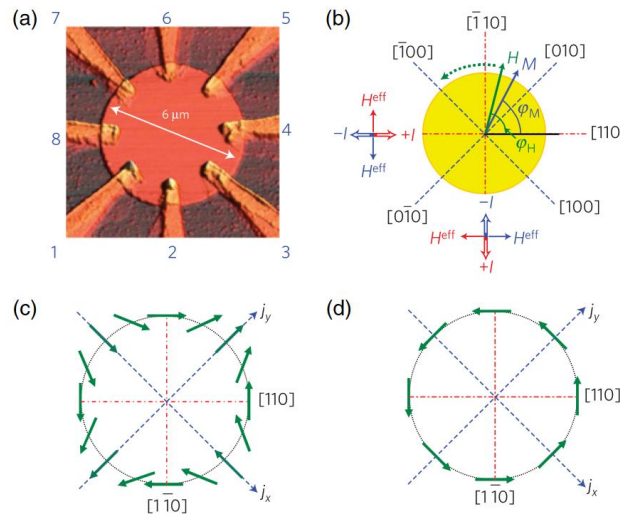


Fig. 1.12 Spin-orbit torque induced magnetization switching in (Ga,Mn)As. (a) Atomic force micrograph of the studied sample with eight nonmagnetic metal contacts. (b) Diagram of device orientation with respect to crystallographic axes, with easy and hard magnetization axes marked with dashed and dot-dashed lines, respectively. Measured directions of the  $H_{\text{eff}}$  field are shown for different current directions. Orientation of the effective SOT field with respect to the current direction for (c) Dresselhaus and (d) Rashba spin-orbit interactions. Taken from Ref. [91].

In addition to STT, the presence of current-induced spin-orbit torque (SOT) also provides a possibility to achieve the current switched magnetization. In a circular patterned (Ga,Mn)As device with eight nonmagnetic Ohmic contacts as shown in Fig. 1.12, in the presence of an external field, when the current is parallel with the [1-10] direction, the measured transverse AMR is positive if magnetization is parallel with the [100] direction and negative if magnetization is parallel with the [010] direction [91]. Such difference can be explained by the external current-induced magnetic field by spin-orbit torque. Interestingly, in the absence of external magnetic field, the SOT in (Ga,Mn)As can generate a 180° magnetization reversal [92].

The successful switching of magnetization by the STT and SOT in demonstrates the possibility of spin-current writing in DFS based spintronic devices.

## 1.5 Organization of this thesis

As discussed in this short literature review, different physical parameters of III-V lead to a diversity of magnetic and electrical properties in the III-Mn-V DFSs. Thus, the systematic investigation of different Mn doped III-V DFSs is essential to figure out a full picture to understand the physics behind. However, due to low solubility of Mn in III-V semiconductors (usually less than 0.1%), regular equilibrium ways of material preparation only produce either Mn-rich nanoclusters or DFS whose Mn concentration is too low to display ferromagnetic behavior. Despite the successful preparation of (Ga,Mn)As by LT-MBE, it is still a great challenge to prepare the complete family of highly epitaxial Mn doped III-V DFSs, particularly for the phosphides. The combination of ion implantation and pulsed laser melting (PLM) not only overcomes the solubility obstacle, incorporating more Mn (several percents) atoms into the substitutional sites, but also succeeds in bringing new DFS members such as (Ga,Mn)P and (In,Mn)P. In this thesis, three different epitaxial III-Mn-V DFSs, (Ga,Mn)As, (In,Mn)As and (Ga,Mn)P, are successfully produced by ion implantation and pulsed laser melting. Through the comparison between these three different DFSs, we aim at comprehending the different nature of hole-mediated ferromagnetism, *e.g.* ferromagnetism in metallic (Ga,Mn)As and in insulating (Ga,Mn)P.

This thesis is organized as below:

In chapter 2, I will introduce the experimental techniques used in the sample preparation, including ion implantation and pulsed laser melting. For the physical properties measurement, the magnetic properties are measured by superconducting quantum interference device (SQUID) and X-ray magnetic circular dichroism (XMCD, at the beamline UE46/PGM-I at BESSY II). Hall measurement system (HMS) is used to investigate the electrical properties.

In chapter 3, I will introduce the ferromagnetic (Ga,Mn)P with different Mn concentrations prepared by ion implantation and pulsed laser melting. A change of magnetic, transport, and structural properties is observed when the Mn concentration increases from 3 to 12%. The results from micro-Raman spectroscopy and high-resolution X-ray diffraction suggest that the Mn-implanted region is epitaxially recrystallized by pulsed laser treatment. The in-plane uniaxial magnetic anisotropy, negative magnetoresistance, and anomalous Hall effect indicate the DFS nature of (Ga,Mn)P.

In chapter 4, I present a systematic investigation on the evolution of microstructure and magnetic properties of (Ga,Mn)P depending on different pulsed laser annealing energies. The microstructure was analyzed by high resolution X-ray diffraction (HR-XRD), transmission electron microscopy (TEM), Rutherford backscattering spectrometry (RBS), ultraviolet Raman spectroscopy (UV-RS), and extended X-ray absorption fine structure (EXAFS) spectroscopy. In addition, a reduction of the  $T_C$  and of the uniaxial magnetic anisotropy gradually happens when more defects and the domains appear upon increasing the annealing energy density. This fact univocally points to the decisive role of the laser energies on the resulting magnetic characteristics in the processed layers.

In chapter 5, by using ion implantation and laser melting, (In,Mn)As on InAs substrate is successfully produced. Moreover, a record  $T_C$  of 82 K is obtained in the sample with an out-of-plane direction magnetic anisotropy when the Mn concentration is around 10.5%. The out-of-plane uniaxial magnetic anisotropy results from the tensile strain between the upper (In,Mn)As layer and the InAs substrate, which is proved by high-resolution X-ray diffraction (HR-XRD) and XMCD. The (In,Mn)As obtained presents a test-bed for spin-transfer-torque induced magnetization reversal in spintronic devices.

In chapter 6, highly epitaxial (Ga,Mn)As and (In,Mn)As samples with low Mn concentrations ( $0.30\% \leq x \leq 2.2\%$ ) are prepared. Through the systematic comparison of electric and magnetic properties between two different materials, we observed that in both materials upon increasing the Mn concentration, a conductivity change from insulating (hopping) to metallic-like is accompanied by a gradual build-up of a long-range magnetic coupling and an increase of the Curie temperature. Our findings strongly advocate for the heterogeneous model of electronic states at the localization boundary and point to the crucial role of weakly localized holes in mediating efficient spin-spin interactions even on the insulator side of the insulator-metal transition.

In chapter 7, all the results are summarized. An outlook of the future work on Mn doped III-V DFSs prepared by ion implantation and pulsed laser melting is presented.

## Chapter 2

# Experimental methods

### 2.1 Sample preparation

To date, LT-MBE is treated as the main way for the preparation of III-Mn-V DFSs. The non-equilibrium growth process successfully overcomes the limitation of Mn solubility, producing heavily Mn doped III-V DFSs. In our work, different from the film growth process of LT-MBE, Mn atoms are implanted into the III-V wafer by means of ion implantation to achieve Mn super-saturated doping. Eventually, a Mn doped III-V DFS epitaxial layer is realized by liquid phase epitaxial growth induced by subsequent pulsed laser melting.

#### 2.1.1 Ion implantation

As widely used for obtaining doped semiconductors and for fabricating *p-n* junctions, ion implantation has been regarded as a mature technology in semiconductor industry. In the production, the advantages of high efficiency and reproducibility render ion implantation an ideal approach for large scale production when compared with some other growth methods, i.e. MBE and pulsed laser deposition (PLD), *etc.* On the other hand, the kinetic nature of ion implantation overcomes the element solubility limitation, achieving super-saturation in doped semiconductor materials successfully.

When ions are implanted into the host matrix, the collision (including elastic and inelastic collision) between implanted ions and host atoms transfers the kinetic energy of implanted ions into the host matrix. Part of the kinetic energy is transferred through the elastic collisions to the lattice, leading to a result that the host atoms can be kicked away from the lattice sites, resulting in the crystal structural disorder and amorphization when the implantation fluence is large enough.

It is worth noting that due to the energy loss of the implanted ions during the collision process, the element distribution is strongly related to the implantation energy. The energy loss for the unit penetration depth  $dE/dx$ , is used to describe the stopping effect. The depth profile of the stopped implanted ions theoretically follows a Gaussian distribution which is described by the projected range  $R_p$  and the standard deviation  $\Delta R_p$ .

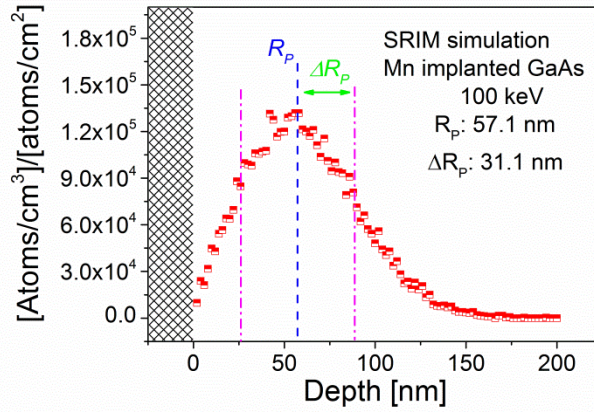


Fig. 2.1 Mn ions profile from a SRIM simulation for 100 keV Mn implantation in GaAs at an angle of 7°.

Using the software of Stopping and Range of Ions in Matter (SRIM) [93], the detailed distribution information of implanted ions can be obtained. Accordingly, the depth profile of the probability of the implanted ions along the normal axis can be described as:

$$P(x) = \frac{1}{\sqrt{2\pi}\Delta R_p} \exp\left(-\frac{(x-R_p)^2}{2(\Delta R_p)^2}\right) \quad 2.1$$

Where the  $\Delta R_p$  is the longitudinal straggling range, the  $R_p$  is the projected range, and the  $x$  is the depth in the layer. The peak position appears at the position of  $R_p$ , where the exponential term equals to 1. Thus, the probability at the peak position  $R_p$  can be shown as:

$$P(R_p) = \frac{1}{\sqrt{2\pi}\Delta R_p} \quad 2.2$$

When  $P(x)$  is multiplied with the implantation fluence  $\Phi$ , the atom density of the implanted ions at the depth of  $x$ ,  $N(x)$ , is obtained. As an example, Fig. 2.1 shows the depth profile of Mn in GaAs.  $R_p$  and  $\Delta R_p$  are labeled in the figure. As shown in Fig. 2.2, the increase of the implantation fluence directly causes an increase of the Mn atom density in the GaAs matrix. The precise and reproducible manipulation of both the implantation energy and the fluence ensure the quantitative determination of the Mn doping for all samples.

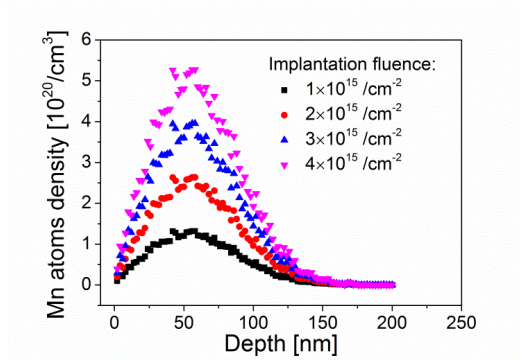


Fig. 2.2 Implantation fluence dependent Mn distribution in GaAs

In this thesis, all implantation is performed in the Ion Beam Center (IBC) of Helmholtz-Zentrum Dresden-Rossendorf (HZDR).

## 2.1.2 Pulsed laser melting (PLM)

In the past several decades, pulsed lasers have been successfully employed for rapid melting and recrystallization to achieve supersaturated semiconductors, particularly for IV-elementary and III-V compound semiconductors. When the amorphous as-implanted sample gets irradiated by a pulsed laser, the photons are absorbed in the near-surface regime of the layer. Then, the absorbed energy is transferred into local heat which melts the irradiation area and diffuses at a speed of m/s into the sample. When the molten regime extends into the undamaged substrate and the laser pulse is off, the large temperature gradient between the molten doped regime and the substrate at ambient temperature causes the liquid phase epitaxial re-growth at a speed of around m/s. Different from the traditional furnace annealing or rapid thermal annealing (RTA), the ultra-fast regrowth velocity by pulsed laser traps the dopant atoms into the substitutional sites of the lattice and effectively suppresses the generation of Mn-rich second-phases. However, during the epitaxial growth, part of implanted ions diffuse with the liquid-solid phase boundary and pile up at the surface. The dopant diffusion to the surface is the so-called “snow-plow” effect and generally leads to a thin oxide layer on the surface with amorphous nature.

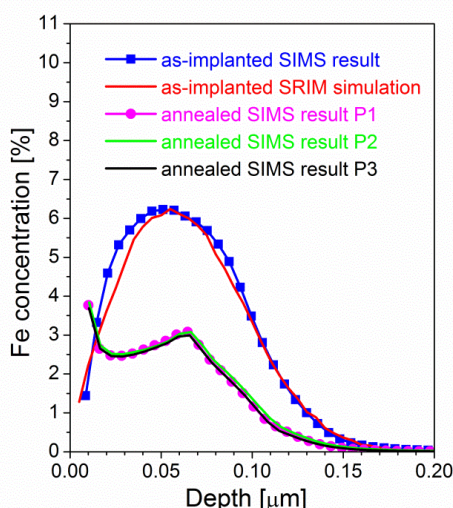


Fig. 2.3 The depth profile of implanted Fe ions before (as-implanted) and after (annealed) pulsed laser melting [94].

As illustrated in Fig. 2.3, the depth profile of the Fe distribution in Fe as-implanted InAs is detected by second ion mass spectrometry (SIMS) which is consistent with the SRIM simulation. Interestingly, the recrystallization by pulsed

laser melting largely redistributes the Fe atom depth profile. As expected, the Fe segregation is observed in the near-surface region, proving the out-diffusion of Fe atoms in the sample. In the deeper region, the epitaxial structure is observed between the doping regime and the substrate. The same epitaxial structural result is also observed in B, As, and P implanted Si after pulsed laser treatment [95].



Fig. 2.4 Excimer laser system applied for pulsed laser melting.

In this thesis, we used a Coherent XeCl excimer laser with 308 nm wavelength and 28 ns pulse duration. The laser spot is homogenized and focused by a fly-eye homogenizer as a  $5 \times 5 \text{ mm}^2$  square spot. The SIMS results (shown in Fig. 2.3) measured at different position (P1, P2, P3) overlap with each other, proving the good spatial homogeneity of the laser beam. The energy density of the spot was manipulated by a manual attenuator from 0.15 to  $1 \text{ J/cm}^2$ .

## 2.2 Physical property measurements

### 2.2.1 Magnetic property measurement: SQUID

The earliest magnetism detection equipment could be traced back to more than two thousand years ago: Compass, a ferromagnetic needle which was used to sense the earth magnetic field and to distinguish directions. To date, a deeper understanding has been reached about the essence of the magnetism. Thus, different types of equipment have been invented to measure the various magnetic properties from different aspects. For instance, when combined with the spectroscopy, a technique named X-ray magnetic circular dichroism (XMCD) takes the full advantage of the different absorption of the circularly polarized X-ray by the electrons with different spin states, enabling this technique detect the magnetism with an elemental sensitivity. Another example is given by the magnetic force microscopy (MFM) which borrows the idea from the atomic force microscopy. When scanning on the sample surface, the magnetic MFM tip will sense the magnetic force from the magnetic regime in the

sample, drawing an image of the magnetic domain.

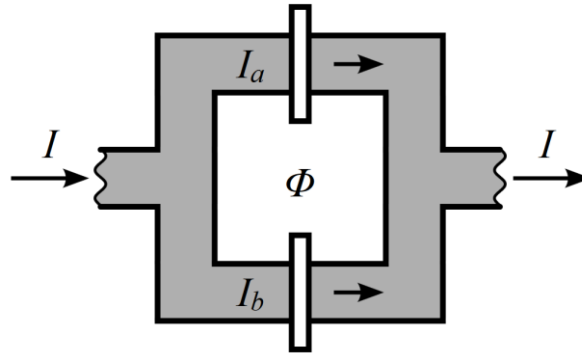


Fig. 2.5 A diagram of a SQUID. The current  $I$  enters and splits into the two paths, each with currents  $I_a$  and  $I_b$ . The thin barriers on each path are Josephson junctions, which together separate the two superconducting regions.  $\Phi$  represents the magnetic flux threading the SQUID loop.

In our work, the magnetic properties are investigated by a commercial superconducting quantum interference device (SQUID, by Quantum Design). SQUID is a very sensitive magnetometer to measure extremely small magnetic moments. As shown in Fig. 2.5 the SQUID sensor has two Josephson junctions in parallel in a superconducting loop. In the absence of any external magnetic field, the input current  $I$  splits into the two branches equally as  $I_a = I_b$ . If a small external magnetic field is applied to the superconducting loop, a screening current,  $I_s$ , begins circulating in the loop that generates a magnetic field canceling the applied external flux. The induced current is in the same direction as  $I$  in one of the branches of the superconducting loop, and is opposite to  $I$  in the other branch; the total current becomes  $I/2 + I_s$  in one branch and  $I/2 - I_s$  in the other. Once the current in either branch exceeds the critical current, a detectable voltage appears across the junction which is a measure of the magnetic moment.

In addition, the application of this technique is also exploited by the Vibrating Sample Magnetometer (VSM), which largely enhances the measurement speed while keeping the same sensitivity as that of SQUID-MPMS. During the measurement, the sample is vibrated at a known frequency and the phase-sensitive detection is employed for rapid data collection and spurious signal rejection, thus, enhancing the efficiency of the result collection.

For the sample mounting, a quartz sample holder is provided. The samples were attached in the quartz holder by low temperature glue, in which the magnetic field is along the out-of-plane and the in-plane directions. The diamagnetic background signal which is from the quartz substrate contributes to the final result and should be subtracted for data plotting. For our dilute magnetic semiconductor samples, the size should be smaller than  $2 \times 5 \times 5 \text{ mm}^3$  due to the limitation of sample chamber. In addition, the measurement sensitivity and the noise level are both around  $10^{-7} \text{ emu}$ .



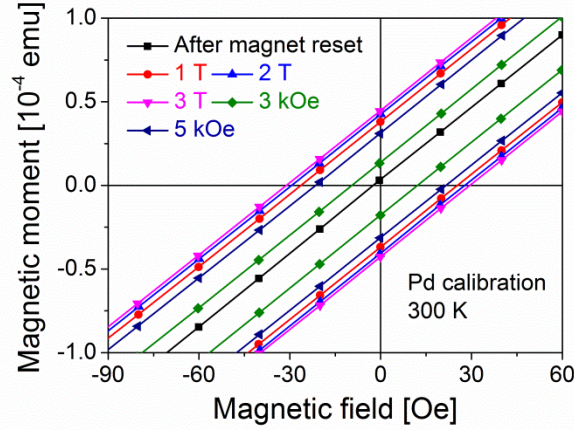


Fig. 2.6 Trapped field calibration is performed by measuring the standard sample (paramagnetic Pd) when the field goes down from different field values.

Some researchers are interested in measuring the magnetic behaviors in the regime of very tiny magnetic field (around several Oe). However, the magnet consisting of superconducting wires will trap remnant fields in its windings after being charged to high magnetic fields (several Tesla), as shown in Fig. 2.6. This tiny trapped field will largely influence on the measured results particularly under a zero nearby field. Through the calibration by measuring the magnetization of a paramagnetic Pd standard sample, the trapped fields in our SQUID-VSM system were detected as around  $\pm 10$ ,  $\pm 20$ ,  $\pm 25$ ,  $\pm 29$ ,  $\pm 30$ , and  $\pm 31$  Oe when the magnetic field is decreased to zero from  $\pm 3$ ,  $\pm 5$ ,  $\pm 10$ ,  $\pm 20$ , and  $\pm 30$  kOe, respectively. However, such remnant field can be eliminated by magnet reset operation which quenches the superconducting state in the magnet. As shown in Fig. 2.6, the proportional dependence of the MH measurement crossing the origin point after the magnet reset demonstrates that the trapped field has been totally removed from the superconducting magnet. It is worth mentioning that the trapped field elimination is crucial to the remnant magnetization measurement, particularly for the sample with small coercivities below 50 Oe.

### 2.2.2 Electrical properties measurement: HMS

The magnetic field- and temperature-dependent electrical behaviors in a semiconductor reflect crucial information of the electronic states. In our work, to study the interplay between magnetism and localization in DFSs, the electrical measurements are necessary.

Here, a fully integrated Hall measurement system (HMS) Model 9700A from Lake Shore (Fig. 2.7) is used to characterize electrical properties, i.e. magnetoresistance, Hall resistance, and temperature dependent sheet resistance. For all electrical measurements, the sample resistance ranging from 0.04 m $\Omega$  to 200 G $\Omega$  is

within the detectable limitation of our setup. When measuring the magnetoresistance and Hall effect, a superconducting magnet is employed to set magnetic field up to  $\pm 9$  T, and the temperature is varied from 1.8 to 400 K by liquid helium cooling. Directly after pulsed laser melting, DFS layer contains a top layer which is magnetically inert, but very conductive, preventing the electrical measurement of the active DFS, particularly for the (Ga,Mn)P layer. After the laser melting, the samples were dipped in dilute HCl (10%) to etch the top layer with bad crystalline quality and to remove the native oxide. For most of the electrical measurements, the Van-der-Pauw geometry is used and a thin Au layer is sputtered to get better Ohmic contact. The measured sample size is  $5 \times 5$  mm<sup>2</sup>. The difference of the (Ga,Mn)P electrical conductivity between and after the HCl etching is shown in Fig. 2.8. Thus, removing such conductive cap layer is quite necessary to obtain the proper electrical signal from the (Ga,Mn)P layer.



Fig. 2.7 Lake Shore Hall measurement system Model 9700A (HMS)

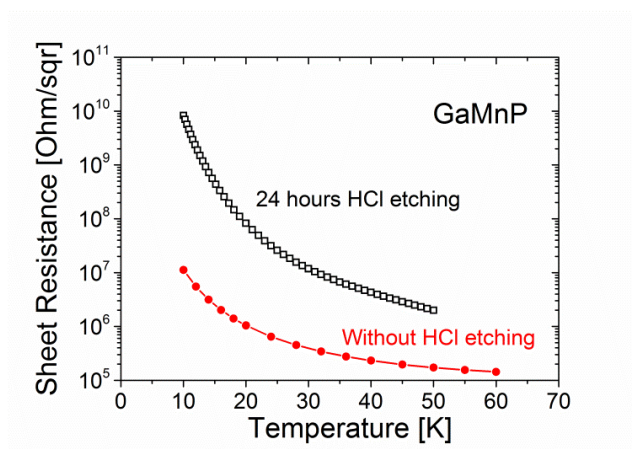


Fig. 2.8 The difference of the (Ga,Mn)P electrical conductivity between and after the HCl etching.

### **2.2.3 Micro-Raman spectroscopy**

In this work, micro-Raman spectroscopy is used to determine the recrystallized quality of (Ga,Mn)P samples. Raman measurements were performed in the backscattering geometry using the 325 nm line of a He-Cd laser, in the  $\bar{z}$  ( $y'$ ,  $y'$ )  $z$  back-scattering configuration using a LabRam HR800 (HORIBA Jobin Yvon GmbH, Bensheim, Germany) spectrometer aided with an optical microscope Olympus BX40 (Olympus Corporation, Hamburg, Germany). A 40  $\times$  objective lens was used to focus the laser beam and to collect the Raman signal.

## Chapter 3

### **Ferromagnetic (Ga,Mn)P prepared by ion implantation and pulsed laser annealing**

This chapter has been published as:

Y. Yuan *et al.*, IEEE Trans. Magn., **50**, 2401304 (2014)

We present the magnetic, transport and structural properties of (Ga,Mn)P with different Mn concentrations prepared by ion implantation and pulsed laser annealing. The Curie temperature increases with Mn concentration and the samples show in-plane magnetic anisotropy due to the in-plane compressive strain in the (Ga,Mn)P layer. Anomalous Hall effect and negative magnetoresistance are observed, indicating the carrier mediated nature of the ferromagnetism in (Ga,Mn)P. According to the micro-Raman spectroscopy data after pulsed laser annealing the implanted layer has been fully recrystallized and the carrier concentration (hole) increases with Mn concentration.

### 3.1 Introduction

During the past several decades, how to tune the charge and spin functionalities in one material has been the core subject for achieving spintronic devices. The discovery of Mn doped III-V dilute ferromagnetic semiconductors (DFS) has proven to be of special interest due to the possibility of realizing ferromagnetism through the  $p$ - $d$  exchange interaction between Mn ions and holes [96-99]. When compared to (Ga,Mn)As which is the prototype III-V DFS that has drawn the most attention in research, GaP has a larger and indirect band gap with a Mn energy level of around 400 meV above the valence band. Particularly, it is expected to obtain strong  $p$ - $d$  hybridization in (Ga,Mn)P due to the short bond length. However, to our knowledge, fewer investigations have been carried out to obtain (Ga,Mn)P through traditional methods as for other DFS [100, 101], such as low temperature molecule beam epitaxy (LT-MBE), probably due to technical difficulties. Therefore, an alternative method is necessary for the preparation of (Ga,Mn)P DFS. Scarpulla *et al.*, have been successful in preparing (Ga,Mn)As and (Ga,Mn)P through ion-implantation and pulsed laser annealing [59, 102]. By controlling the implantation fluence, different Mn concentrations much higher ( $\sim 10^{20-21}$  cm<sup>-3</sup>) than the solid solubility in GaP are obtained, which is a pre-requisite to obtain (Ga,Mn)P DFS. Meanwhile, the large crystal regrowth velocity after pulsed laser annealing traps the implanted Mn ions into the substitutional sites and avoid their precipitation [103]. Moreover, due to the high temperature processing, interstitial Mn (Mn<sub>int</sub>), acting as double donors which compensate holes, can be largely reduced compared to samples prepared by LT-MBE [102]. The obtained ferromagnetic (Ga,Mn)P by ion implantation and pulsed laser annealing also shows X-ray magnetic circular dichroism (XMCD) at the Mn L<sub>3,2</sub> edges [104] and the same hydrogenation effect as for (Ga,Mn)As [105]. All evidence supports the carrier-mediated nature of ferromagnetism in (Ga,Mn)P.

In this work, we prepared ferromagnetic (Ga,Mn)P with different Mn concentrations by ion implantation and pulsed laser annealing. We present a systematic investigation about its magnetic, magneto-transport and structural properties. The prepared (Ga,Mn)P films show a clearly in-plane magnetic easy axis due to the compressive strain from the substrate. The Curie temperature increases with increasing Mn concentration, so as the hole concentrations as indicated by Raman scattering. The measured anomalous Hall effect and negative magnetoresistance confirm the hole-mediated nature of the ferromagnetism in (Ga,Mn)P. The sample with the largest Mn concentration does not show metallic behavior, which indicates a non-merged impurity band in (Ga,Mn)P.

## 3.2 Experiment section

Intrinsic GaP (001) wafers were implanted with 50 keV Mn ions at room temperature. The Mn fluences were  $5 \times 10^{15} \text{ cm}^{-2}$ ,  $1 \times 10^{16} \text{ cm}^{-2}$ , and  $2 \times 10^{16} \text{ cm}^{-2}$ , corresponding to  $x \sim 0.03$ , 0.06, and 0.12 in  $\text{Ga}_{1-x}\text{Mn}_x\text{P}$  over a depth of around 60 nm, respectively. A XeCl excimer laser (Coherent COMPexPRO201,  $\lambda=308 \text{ nm}$ , pulse duration of 30 ns) is used for annealing with a single pulse with the energy density varying from 0.35 to 0.60  $\text{J/cm}^2$ . According to the magnetic and structural properties, it was determined that the 0.45  $\text{J/cm}^2$  is the optimal annealing condition for each sample of different fluence. After annealing, all samples were etched in 10% HCl to remove the oxide layer. It is expected that significant amount of Mn ions which are not in the crystalline (Ga,Mn)P phase were removed after etching, resulting in the reduction of the Mn concentration to around half of its designed values [106]. Magnetic properties were analyzed using a superconducting quantum interference device magnetometer (Quantum Design, SQUID-VSM). Raman measurements were performed in the backscattering geometry using the 325 nm line of a He-Cd laser, and in the  $\bar{z}(y', y')$  z back-scattering configuration. The Raman spectrometer is a LabRam HR800 (HORIBA Jobin Yvon GmbH, Bensheim, Germany) with an optical microscope Olympus BX40 (Olympus Corporation, Hamburg, Germany). A 40 $\times$  objective was used to focus the laser beam and to collect the Raman signal.

## 3.3 Results and discussion

### 3.3.1 Magnetism

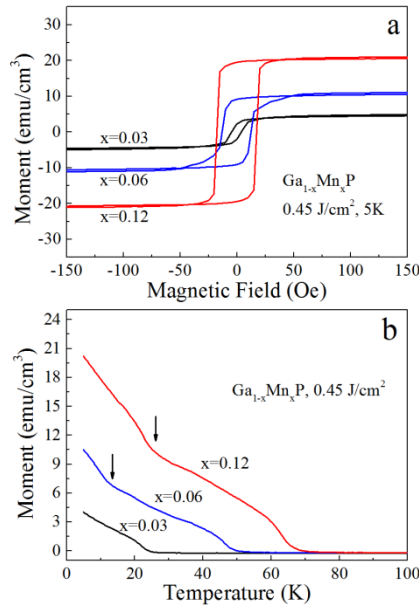


Fig. 3.1 (a) Hysteresis and (b) magnetization versus temperature for  $\text{Ga}_{1-x}\text{Mn}_x\text{P}$  with  $x \sim 0.03$ , 0.06, and 0.12.

Figure 3.1(a) shows the magnetic field dependent magnetization measured at 5 K for (Ga,Mn)P with different Mn concentrations annealed with the laser energy density of  $0.45 \text{ J/cm}^2$ . The magnetic field was applied parallel to the in-plane GaP [1-10] direction. The clear square-like hysteresis indicates that all samples are ferromagnetic with in-plane magnetic easy axis direction. The saturation magnetization is  $\sim 2.6 \mu_B/\text{Mn}$  by considering the fact that half of Mn atoms have been removed during etching [106], probably the small extent of the  $p$ -wave functions due to large Mn binding energy leads to this value smaller than the expected value of  $5 \mu_B/\text{Mn}$  [33]. The coercive field decreases with Mn concentrations from around 17 Oe for the sample with 12% Mn to 12 Oe and 4 Oe for the 6% and 3%, respectively. Magnetization versus temperature was measured in a 30 Oe field (after applying a field of 1000 Oe to saturate the magnetization), along the in-plane direction for all samples, as shown in Fig. 3.1(b). We can roughly estimate the Curie temperature ( $T_C$ ) to be around 25, 50, and 70 K for  $x = 3\%$ , 6%, and 12% respectively. It is worth noting that there is a kink in the temperature dependent magnetization curves as indicated by arrows in Fig. 3.1(b). A similar kink was observed in (Ga,Mn)As with homogeneous Mn distribution, which is due to a spin reorientation transition [75]. However, in our (Ga,Mn)P samples we have not measured the change of magnetic anisotropy with temperature. Such a kink is probably from the tail of Mn Gaussian distribution in the layer with a lower  $T_C$ .

### 3.3.2 Magnetic anisotropy

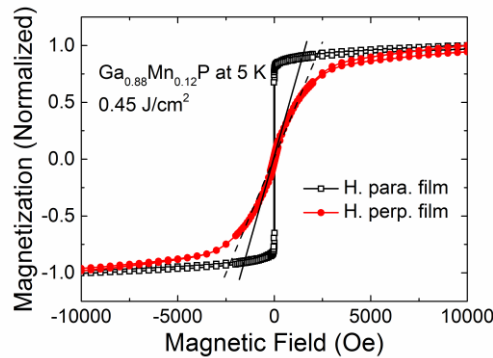


Fig. 3.2 Hysteresis loops (Normalized) at 5 K. The field is applied either parallel (solid circle) or perpendicular (open square) to the film. The solid and dash lines are used to estimate the lower and upper limit of anisotropy field, respectively.

For magnetic semiconductors encountering a compressive strain, one expects a large magnetic anisotropy, as for the case of (Ga,Mn)As grown on GaAs substrates [107]. We also measured the (Ga,Mn)P sample under the magnetic field perpendicular and parallel to the sample surface as shown in Fig. 3.2. Obviously, the more

square-like hysteresis loop when the field is parallel to the film surface indicates that the in-plane GaP [1-10] direction is the easy axis, and the out-of-plane direction along GaP [001] is the hard axis. This uniaxial magnetic anisotropy is due to the in-plane compressive lattice in the (Ga,Mn)P layer. Note that the substitution of Ga ions by Mn results in a larger lattice parameter [107]. The top (Ga,Mn)P layer therefore undergoes compressive strain. Due to the fact it is very hard to measure the real hard axis loop without a precise control of the sample alignment, we deduced the lower and upper limit of the magnetic anisotropy field according to the shape of the hard axis loop to be  $\sim 1399$  Oe and  $\sim 2499$  Oe, respectively. The anisotropy field at 5 K is in the range (1000~2000 Oe) for (Ga,Mn)As and (Ga,Mn)P reported by other groups [108, 109].

### 3.3.3 Electrical behavior

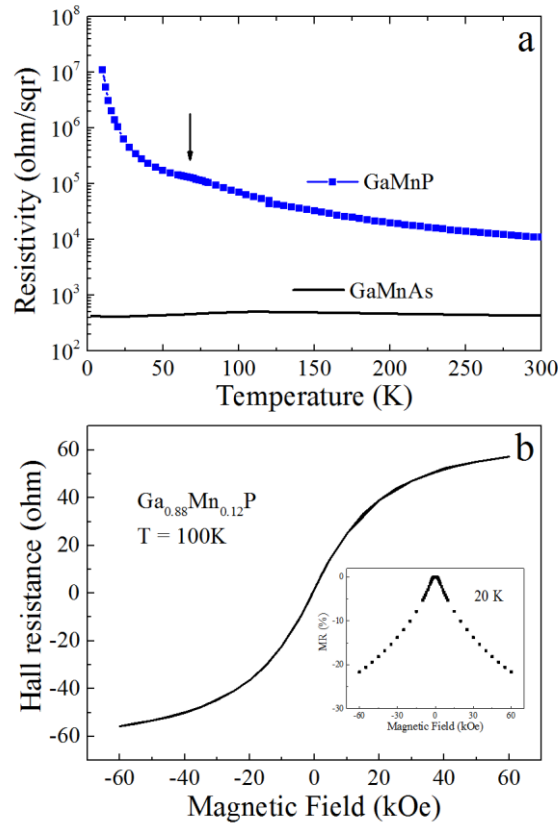


Fig. 3.3 (a) Sheet resistance of  $\text{Ga}_{0.88}\text{Mn}_{0.12}\text{P}$ , and a sample GaMnAs prepared by the same method is given for comparison. (b) Hall resistance versus magnetic field at 100 K. (the inset shows the field dependent sheet resistance at 20 K).

Figure 3.3(a) shows the temperature dependent sheet resistance for  $\text{Ga}_{0.88}\text{Mn}_{0.12}\text{P}$ . The ferromagnetic (Ga,Mn)P layer shows an insulating conducting behavior: The resistance is increased with decreasing temperature from 300 to 5 K. At around  $T_C$ , we observe a hump-like feature indicated by the arrow, but much less pronounced than that in (Ga,Mn)As. The temperature dependent resistance indicates that the holes in



(Ga,Mn)P are residing in an impurity band [59]. However, even for (Ga,Mn)As, it is still under debate if the Fermi level resides in the merged valance band or in the separated impurity band [39, 45, 110]. The sheet resistance is in the range of  $10^9$  ohm at low temperature (Note that for the sample  $\text{Ga}_{0.88}\text{Mn}_{0.12}\text{P}$ , the sheet resistance is already  $10^7$  ohm at low temperature) and makes the measurement of samples with Mn lower concentration difficult. For this (Ga,Mn)P sample, the hole concentration is calculated to be around  $1.03 \times 10^{18} / \text{cm}^3$  by assuming a thickness of 60 nm from the slope of Hall resistance at 300 K. This value can be underestimated due to the appearance of anomalous Hall effect [111]. Figure 3.3 (b) shows the field dependent Hall resistance measured at 100 K. A clear anomalous Hall effect has been observed from the non-linear dependence, which is due to the paramagnetic nature of the film at 100 K. At temperature below  $T_C$ , we should observe a hysteresis loop with the same shape as the magnetization. However, the Hall effect measurement is prevented due to the large magnetoresistance and the low hole mobility. The inset in Figure 3.3(b) shows the field dependent sheet resistance at 20 K. The same as for (Ga,Mn)As layers, the sample shows a negative magnetoresistance [112]. The negative magnetoresistance and the anomalous Hall effect reflect the intimate relationship between transport and ferromagnetism [112].

### 3.3.4 Raman spectra

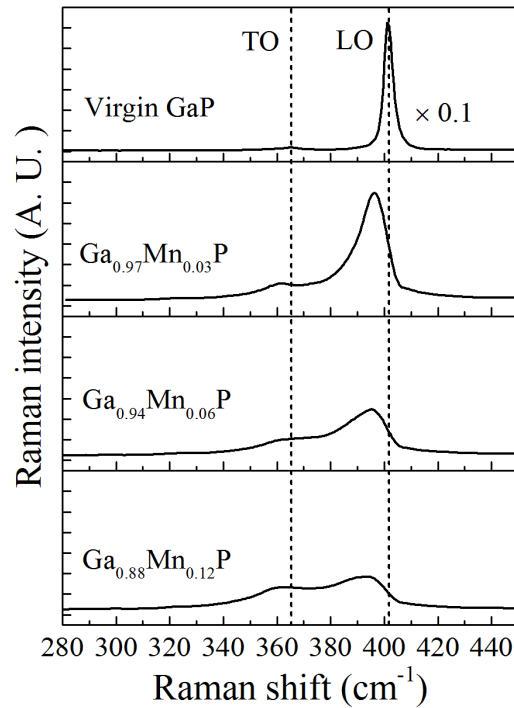


Fig. 3.4 Raman spectra of (Ga,Mn)P layers with different Mn concentrations.

Raman spectra taken under a 325 nm excitation of the three (Ga,Mn)P samples with Mn concentration 3%, 6%, and 12% are shown in Fig. 3.4, and a virgin GaP is also presented for comparison. The peak at  $401\text{ cm}^{-1}$  is the GaP longitudinal-optical (LO) phonon mode, while the transverse-optical (TO) phonons for (100) GaP is forbidden according to the Raman selection rules which are determined by the deformation-potential and the Frohlich electron-phonon interaction. However, due to the disorder from the recrystallization after PLA and Mn doping, the TO mode could be observed. The appearance of the Raman scattering modes in (Ga,Mn)P indicates the recrystallization from pulsed laser annealing. We observed that the LO mode shifts to lower frequencies with increasing Mn concentration ( $401\text{ cm}^{-1}$  to  $394\text{ cm}^{-1}$  for  $x$  from 0 to 0.12). This behavior has been observed for (Ga,Mn)As and is typical for heavily doped semiconductors with low mobility [113]. The broadening in the Raman spectra indicates the appearance of the coupled plasmon-LO-phonon mode (CPLOM). The Raman results give evidence that the hole concentration in (Ga,Mn)P increases with Mn concentration.

### 3.4 Conclusion

Ferromagnetic (Ga,Mn)P layers with different Mn concentrations are prepared by ion implantation and pulsed laser annealing. As more Mn ions are introduced, the layers show higher Curie temperatures, meaning that more Mn ions substitute the  $\text{Ga}^{3+}$  sites. Magneto-transport measurements support that the ferromagnetism in (Ga,Mn)P is hole mediated. However, the ferromagnetic (Ga,Mn)P sample with a  $T_C$  of 70 K shows insulating behavior. A detailed investigation of ferromagnetic (Ga,Mn)P or (In,Mn)P [68], in which the binding energy of Mn is much larger than that of (Ga,Mn)As, could give a better understanding about the III-V: Mn DFS family.



## Chapter 4

# Ferromagnetic Mn-implanted GaP: Microstructures vs. magnetic properties

This chapter has been published as:

Ye Yuan *et al.*, ACS Appl. Mater. Interfaces, **8**, 3912-3918 (2016)

Ferromagnetic (Ga,Mn)P layers were prepared by ion implantation and pulsed laser annealing (PLA). We present a systematic investigation on the evolution of microstructure and magnetic properties depending on the pulsed laser annealing energy. The sample microstructure was analyzed by high-resolution X-ray diffraction (HR-XRD), transmission electron microscopy (TEM), Rutherford backscattering spectrometry (RBS), ultraviolet Raman spectroscopy (UV-RS), and extended X-ray absorption fine structure (EXAFS) spectroscopy. The presence of X-ray Pendellösung fringes around GaP (004) and RBS channeling prove the epitaxial structure of the (Ga,Mn)P layer annealed at the optimized laser energy density ( $0.40 \text{ J/cm}^2$ ). However, a forbidden TO vibrational mode of GaP appears and increases with annealing energy, suggesting the formation of defective domains inside the layer. These domains mainly appear in the sample surface region and extend to almost the whole layer with increasing annealing energy. The reduction of the Curie temperature ( $T_C$ ) and of the uniaxial magnetic anisotropy gradually happens when more defects and the domains appear as increasing the annealing energy density. This fact univocally points to the decisive role of the PLA parameters on the resulting magnetic characteristics in the processed layers, which eventually determine the magnetic (or spintronics) figure of merit.

## 4.1 Introduction

During the past decade, ion implantation has become an alternative non-equilibrium method to introduce Mn atoms into III-V compounds to obtain dilute ferromagnetic semiconductors (DFS) [54, 59, 102, 114, 115]. Although thermal annealing has been an effective and general way for crystallizing the implanted (amorphous) layer and for activating the implanted dopant atoms, the easy generation of Mn-V second phases prohibit most traditional methods to fabricate III-Mn-V DFS, *e.g.*, furnace annealing (FA), and rapid thermal annealing (RTA) [116, 117]. Being different from these annealing approaches, flash lamp annealing (FLA) within only milli-seconds can effectively prevent the Mn ion out-diffusion which has been seen during RTA process [118]. Nonetheless, the recrystallization efficiency of FLA is still far from satisfactory, so that the (Ga,Mn)As samples only reveal weak ferromagnetism [118]. Therefore, much faster annealing especially within nano-seconds is mandatory to achieve high-quality DFS. A pulsed laser with a duration of several tens of nanoseconds (ns) is exactly qualified for this demand, and various DFSs have been successfully obtained through ion implantation combined with pulsed laser annealing (PLA) [54, 59, 102, 108, 117]. Especially in (Ga,Mn)P, which is hardly to obtain by low-temperature molecule beam epitaxy (LT-MBE, the most applicable way for (Ga,Mn)As), the large band gap and Mn-impurity binding energy essentially offer more angles to understand the ferromagnetism origin in DFSs [59, 119-121]. During the annealing process, the nanosecond laser pulse causes a huge temperature gradient between the substrate and the implanted layer, and a large regrowth velocity could trap the Mn atoms in Ga sites in the regrown region. Thus, the interaction between the laser light and solid materials can affect the quality of epitaxial regrowth, for instance, the recrystallization and dopant activation [54, 122]. Both effects strongly influence the crystalline microstructures and the ferromagnetic properties, including magnetization, Curie temperature, as well as magnetic anisotropy [13]. Therefore, it is expected that by optimizing the PLA conditions epitaxial (Ga,Mn)P with a high Curie temperature and favorable micromagnetic properties could be achieved.

In this paper, we present a systematic research on the relation between PLA parameters, microstructures, and ferromagnetic properties of (Ga,Mn)P DFS. High-resolution X-ray diffraction (HR-XRD), transmission electron microscopy (TEM), Rutherford backscattering spectrometry (RBS), ultraviolet Raman spectroscopy, and extended X-ray absorption fine structure (EXAFS) were applied to analyze the microstructures of the samples annealed at various conditions. The declining of uniaxial magnetic anisotropy and ferromagnetic moment is due to defective epitaxial recrystallization of the Mn-implanted GaP, during PLA at higher

energy fluences.

## 4.2 Experiment section

### 4.2.1 Sample preparation

(Ga,Mn)P samples were prepared by Mn ion implantation into virgin GaP (001) substrates in the Ion Beam Center at Helmholtz-Zentrum Dresden-Rossendorf. The implanting energy was 50 keV. The process was carried out at room temperature, and the implanting angle was set to 7 deg. to avoid the sputtering effect. According to stopping and range of ions in matter (SRIM) simulation, the projected range ( $R_p$ ) and the longitudinal straggling ( $\Delta R_p$ ) for Mn distribution are around 65 and 30 nm, respectively. From the latter quantity one obtains Mn concentration  $x = \Phi/\sqrt{2\pi}\Delta R_p = 0.12$ , where  $\Phi$  is the implanting fluence,  $2 \times 10^{16} \text{ cm}^{-2}$  in this case. An XeCl excimer laser (Coherent ComPexPRO201, wavelength of 308 nm and pulse length of 30 ns) with an energy density of 0.30, 0.40, 0.45, 0.50, and 0.60 J/cm<sup>2</sup> was used in this study. The laser annealing took place at the room temperature and in the air atmosphere. During this high intensity laser process, the near-surface layer including the whole implanted region gets molten whereas the bulk substrate remains at ambient temperature. After the laser pulsed, the molten superficial layer cools down and recrystallizes in a nanosecond time frame forcing the Mn atoms to remain at their actual position at the newly rebuilding host lattice. This effectively prevents Mn aggregation or separation into other crystallographic phases, what allows for Mn doping beyond the solid solubility limit. The whole process starts from the interface between the molten and solid regions, what results in the bottom-up liquid phase epitaxial growth of the (Ga,Mn)P layer.

### 4.2.2 Sample characterization

For Rutherford backscattering spectrometry (RBS), a collimated 1.7 MeV He<sup>+</sup> beam with a 10-20 nA beam current was used, and the scattered ions were collected at a backscattering angle of 170°. The channeling spectra were recorded by aligning the sample to make the impinging He<sup>+</sup> beam parallel to the GaP [001] axis. HR-XRD was performed using a wavelength of  $\lambda=1.0781 \text{ \AA}$  at the BM20 (ROBL) beamline at the European Synchrotron Radiation Facility (ESRF). Raman measurements were performed in the backscattering geometry using the 325 nm line of a He-Cd laser, in the  $\bar{z}$  ( $y'$ ,  $y'$ )  $z$  back-scattering configuration using a LabRam HR800 (HORIBA Jobin Yvon GmbH, Bensheim, Germany) spectrometer aided with an optical microscope Olympus BX40 (Olympus Corporation, Hamburg, Germany). A 40 × objective lens was used to focus the laser beam and to collect the Raman signal. Fluorescence EXAFS experiments were performed at the Dutch-Belgian Beamline

(DUBBLE, BM26) at the ESRF. Finally, the local microstructure of the synthesized films was assessed by an image-corrected FEI Titan 80-300 transmission electron microscope operated at an accelerating voltage of 300 kV.

### **4.2.3 Magnetic properties measurement**

Magnetic properties were measured by a superconducting quantum interference device (SQUID) magnetometer (Quantum Design, SQUID-VSM). The investigated samples were attached to a quartz sample holder by dilute glue. The temperature dependence of the magnetization, M-T curve, was measured between 5 and 100 K, whereas magnetic hysteresis loops, M-H curves, were collected at 5 K. The M-T measurement served to obtain an overview of the magnetic anisotropy and to determine the Curie temperature of the DFS layer, while the M-H studies provided the more detailed information on the magnetic anisotropy. All the data presented in this study have the diamagnetic contribution of the GaP substrate subtracted adequately and the guidance of the sensitive SQUID magnetometry of minute magnetic layers on a substrate [123].

## 4.3 Results and discussion

### 4.3.1 Structures

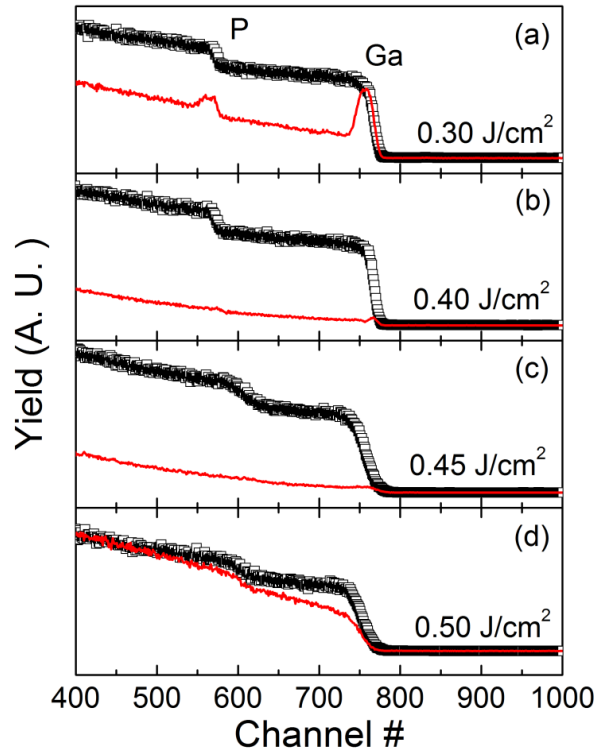


Fig. 4.1 (Color online) RBS random (open squares) and channeling (solid line) spectra of the (Ga,Mn)P samples annealed at energy densities of (a) 0.30, (b) 0.40, (c) 0.45, and (d) 0.50 J/cm<sup>2</sup>, respectively.

The recrystallization process of the annealed (Ga,Mn)P layers is investigated by RBS/channeling spectrometry. Channeling is observed when the implanting incident ion beam is aligned with a major symmetry axis of the crystal. In this case, the incident ions can penetrate the matrix distance without being backscattered, resulting in a drastic reduction of the observed backscattered signal. Herein, the RBS experiment was performed by implanting helium ions into the recrystallized layer along the [100] direction. The selected RBS spectra are plotted in Fig. 4.1 allowing a comparison of the degree of the recrystallization under different annealing conditions. The “Channel” of the x axis is proportional to the energy of the backscattered He ions. From the random spectra, Ga and P signals are both prominent, meanwhile, the Mn signal is much weaker due to its concentration of only several percents and overlapping with the Ga signal. The channeling spectra from layers annealed at 0.40 and 0.45 J/cm<sup>2</sup> confirm the complete recrystallization of the implanted layer and the incorporation of Mn into the Ga lattice sites [106, 124, 125]. The figure of merit of the crystalline quality is the ratio of backscattering yields obtained under the channeling conditions and the random beam incidence,  $\chi_{\min}$ , and it stays below 7% for these two samples. On the contrary, the  $\chi_{\min}$  for 0.50 J/cm<sup>2</sup> annealed sample increases sharply to 36%, suggesting a sizable crystalline disorder induced by the higher energy



annealing. However, too low annealing energy density is also prohibitive to produce a high quality material. As displayed in Fig. 4.1(a), the sample annealed at  $0.30 \text{ J/cm}^2$  shows a similar signal as the as-implanted layer [106], which indicates it fails to trigger an effective epitaxial recrystallization.

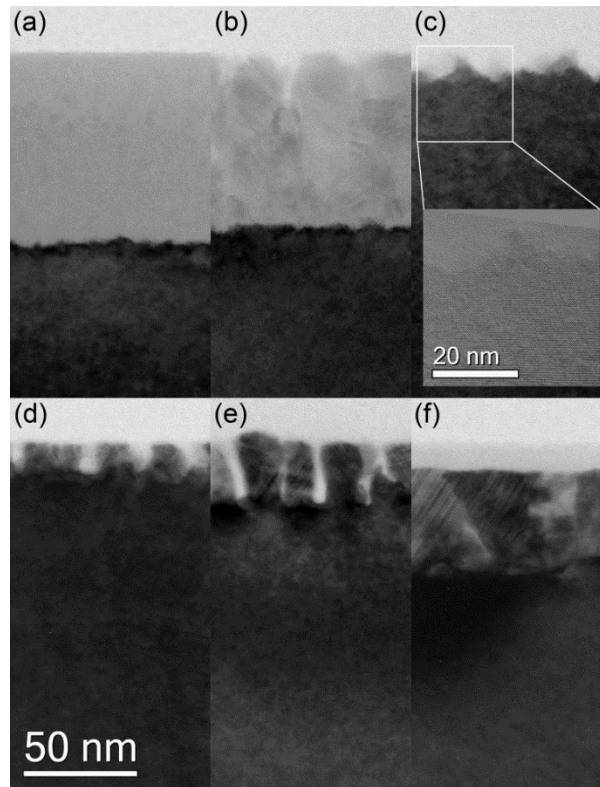


Fig. 4.2 Cross-sectional bright-field TEM micrographs of the (Ga,Mn)P samples (a) after Mn implantation and subsequent annealing for 30 ns with energy density of (b) 0.30, (c) 0.40, (d) 0.45, (e) 0.50, and (f)  $0.60 \text{ J/cm}^2$ . The inset shows a high-resolution TEM image of the surface region of the (Ga,Mn)P sample annealed at  $0.40 \text{ J/cm}^2$ .

The evolution of the microstructure of the Mn-implanted layers on the PLA power density is presented in Fig. 4.2, which collects cross-sectional TEM images of the superficial regions of the Mn-implanted samples before and after the PLA. As indicated by the light-grey color of the 85 nm thick top layer of the as-implanted sample, Mn implantation leads to a complete amorphization of the upper GaP substrate region (Fig. 4.2(a)). The beginning of the crystallization process is seen already after PLA performed at the lowest energy  $0.30 \text{ J/cm}^2$  (Fig. 4.2(b)). The varying diffraction contrast in the Mn implanted part indicates polycrystalline composure of the layer. Only the closest part of the implanted layer to the single-crystalline GaP wafer recrystallizes (Fig. 4.2(b)). In contrast, PLA at  $0.40 \text{ J/cm}^2$  leads to the complete epitaxial recrystallization of the Mn-implanted region, which can be deduced from the uniform dark intensity within the whole zone-axis-oriented

cross-sectional TEM specimen (Fig. 4.2(c)) as well as from the perfect lattice-fringe image in the high-resolution micrograph (inset to Fig. 4.2(c)). Importantly, neither lattice defects, remaining amorphous fractions, nor MnP second phase formation are observed. However, the sample surface shows an enhanced roughness (Fig. 4.2(c)). A further development of the samples microstructure takes place for larger laser energy. Although epitaxial recrystallization is also observed at 0.45 J/cm<sup>2</sup>, the (Ga,Mn)P surface region of this sample gets substantially, defective. In particular, single pillars with heights of about 15 nm containing stacking faults start to grow (Fig. 4.2(d)). As a consequence, the sample surface gets rougher. During annealing at 0.50 J/cm<sup>2</sup>, the pillars, now also showing twin formation, grow even larger with heights up to 30 nm (Fig. 4.2(e)). At an energy density of 0.60 J/cm<sup>2</sup> the defective zone is even thicker, but covered with a 10 nm of a smooth amorphous layer (Fig. 4.2(f)).

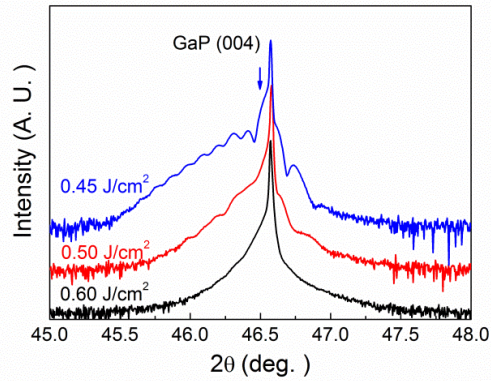


Fig. 4.3 (Color online)  $\theta$ - $2\theta$  scans of the 004 reflection for the (Ga,Mn)P samples treated at different pulsed laser annealing energy densities.

Figure 4.3 illustrates changes of the diffraction pattern observed at high laser energy density,  $\geq 0.45$  J/cm<sup>2</sup>. A presence of Pendellösung fringes seen around the GaP (004) main peak (most pronounced for the layer annealed at 0.45 J/cm<sup>2</sup>) confirms its superior crystallographic structure over the layers obtained at 0.5 and 0.6 J/cm<sup>2</sup>. This confirms the results of the spatially limited TEM studies indicating that also on a large scale the crystallographic structure of (Ga,Mn)P deteriorates substantially when laser energy exceeds 0.5 J/cm<sup>2</sup>. The observation of the Pendellösung fringes allows us to calculate the thickness of the 0.45 J/cm<sup>2</sup> annealed (Ga,Mn)P layer,  $t = \lambda / (2\Delta\theta_P \cdot \cos\theta_B)$ . For  $\theta_B = 23.28^\circ$ , the Bragg angular position of the GaP (004) reflex, and  $\Delta\theta_P = 0.055^\circ$ , the angular separation of two adjacent satellite peaks,  $t = 64$  nm is obtained in an excellent agreement with  $\sqrt{2\pi}\Delta R_P$  value obtained from SRIM simulation.

Another important feature of the diffraction pattern of the layer annealed at 0.45 J/cm<sup>2</sup> is an additional peak emerging on the left shoulder of the GaP (004) main peak,

which stands for the zero order peak of the (Ga,Mn)P epitaxial layer. According to the Bragg equation, a left-shifted peak indicates a lattice expansion, in agreement with the fact that larger Mn atoms substitute smaller Ga sites in GaP host lattice, oppositely to *e.g.* (In,Mn)As, where the InAs lattice contracts when Mn substitute Indium [57]. A smaller lattice parameter of the regrown layer than that of the substrate and their epitaxial relationship indicate that the (Ga,Mn)P layer is under a compressive strain along the in-plane direction on the GaP substrate. This implies that an in-plane magnetic anisotropy (IMA) is expected, the same as in ferromagnetic (Ga,Mn)As [107] with low compensation, assuming a sufficiently large hole density [23].

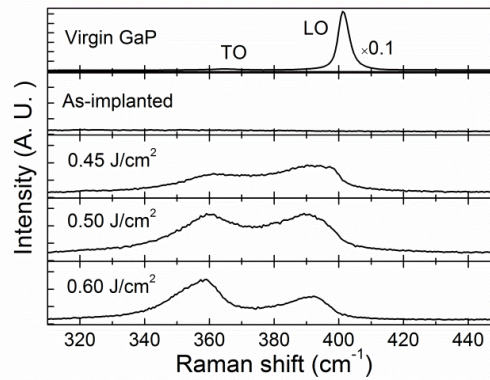


Fig. 4.4 Room-temperature UV-Raman spectra of the virgin GaP, the as-implanted (Ga,Mn)P, and the (Ga,Mn)P layers annealed at various energy densities.

Figure 4.4 shows the non-polarized Raman spectra of different (Ga,Mn)P samples, which are compared with the virgin GaP sample. According to the selection rule of the zinc-blende structure, only the longitudinal optical (LO) phonon mode is allowed in the backscattering configuration in virgin GaP, while, the transverse optical (TO) phonon mode is forbidden. Accordingly in Mn implanted GaP both the LO and TO peaks are not present. However, the PLA process restores the crystallinity of the irradiated layer. Indeed, the spectrum of the 0.45 J/cm<sup>2</sup> annealed (Ga,Mn)P shows the same behavior as (Ga,Mn)As [113, 126, 127]: the LO peak broadens and shifts to the TO position, a typical behavior for heavily doped p-type semiconductors with low carrier mobility [128]. When the carrier plasma couples with the LO phonon through macroscopic electric fields, we can see a phonon-like coupled plasmon-LO-phonon mode (CPLOM). This phenomenon arises from the strongly damped longitudinal vibration of the carrier plasma, and is only obvious in the high holes concentration region [60]. It is worth noting that in all annealed samples a TO peak is seen at 360 cm<sup>-1</sup>, which should be forbidden in this scattering geometry. The important fact is that its intensity increases with annealing energy. This is a similar behavior as for InP layers after PLA [129, 130], and indicates the formation of polycrystalline (Ga,Mn)P

film with misoriented domains. The LO peaks of 0.50 J/cm<sup>2</sup> and 0.60 J/cm<sup>2</sup> annealed (Ga,Mn)P exhibit a downward shift to the left side when compared with 0.45 J/cm<sup>2</sup> annealed sample, arising from two effects: (1) the CPLOM appears and shifts the LO peak to lower frequency and (2) the presence of strain introduced by crystalline domain boundaries and defects. Noted that the LO peak shifts from 389 (0.5 J/cm<sup>2</sup>) back to 392 cm<sup>-1</sup> (0.6 J/cm<sup>2</sup>), this is mainly due to the strain release in the fully polycrystalline (Ga,Mn)P (0.6 J/cm<sup>2</sup>).

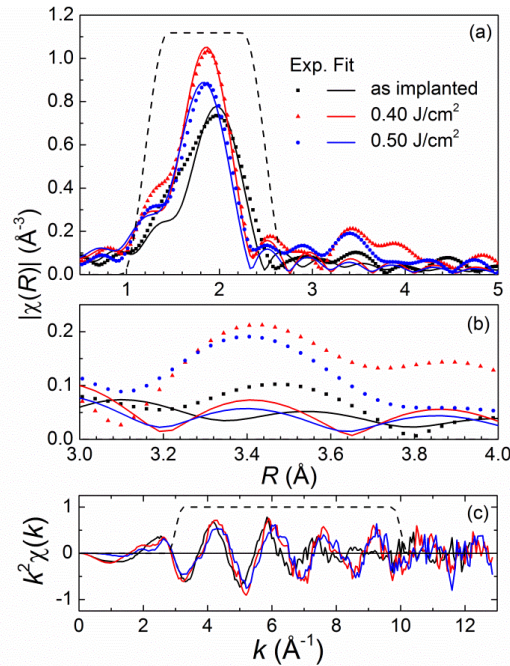


Fig. 4.5 (a) Magnitude of the Fourier transform (FT) of the  $k^2$ -weighted EXAFS (symbols) as a function of non-phase corrected radial distance  $R$ . The solid lines represent the best fit to the experimental data in an  $R$  window corresponding to the Phosphorus first-neighbor shell. The dashed line represents the Hanning window from 1.2 to 2.5 Å with a width of 0.5 Å used for the backward FT in the fitting procedure. (b) The zoom ranging from 2.5 to 5.0 Å of (a). (c)  $k^2$ -weighted EXAFS as a function of photoelectron momentum. The dashed line represents the Hanning window from 3 to 10 Å<sup>-1</sup> with a width of 0.5 Å<sup>-1</sup> used for the backward FT in the fitting procedure.

The EXAFS measurements were performed at the Mn K-edge (6539 eV) at room temperature and their analysis is presented in Fig. 4.5(a). The 9-element monolithic Ge detector was positioned at  $\sim 90^\circ$  and the sample surface at  $\sim 45^\circ$  with respect to the incoming X-ray beam. Background subtraction, data processing, and fitting were performed with ATHENA and ARTEMIS from the IFEFFIT 1.2.11 c package [131, 132]. Data were recorded up to a photoelectron wavenumber  $k$  of 13 Å<sup>-1</sup>, while the Fourier transform (FT) of the normalized EXAFS oscillations was performed over a  $k$ -range of 3 to 10 Å<sup>-1</sup> (maximum  $k$  imposed by statistics), using a Hanning window with a width of 0.5 Å<sup>-1</sup>. The  $k^2$ -weighted EXAFS as a function of photoelectron momentum is shown in Fig. 4.5(c), for three different samples (as implanted, 0.40,

and 0.5 J/cm<sup>2</sup> annealed samples). To fit the data, a backward FT was performed for a non-phase corrected radial distance range of 1.2 to 2.5 Å, using a Hanning window with a width of 0.5 Å, as shown by the dashed line in Fig. 4.5(a). Ab initio calculations (feff832) were used to determine the backscattering amplitude and the phase shift of the single scattering path corresponding to the P first-neighbor shell of a Mn absorber in a Ga site in GaP. The path lengths and Debye-Waller factors (DWFs)  $\sigma^2$  were taken as independent variables (compiled in Table 4.1). The coordination number was set to 4 defined by the zinc-blende structure. A passive electron reduction factor  $S_0^2=0.76(7)$  was determined from the simultaneous fit to the three data sets.

	As implanted	0.40 J/cm <sup>2</sup>	0.50 J/cm <sup>2</sup>
$R$ (Å)	2.46 (4)	2.35 (3)	2.33 (3)
$\sigma^2$ (Å <sup>2</sup> )	0.012 (3)	0.007 (2)	0.010 (2)

Table 4.1 The fitting structures parameters (radial  $R$  and Debye-Waller factors “ $\sigma^2$ ”) of the as implanted, 0.40, and 0.50 J/cm<sup>2</sup> annealed (Ga,Mn)P samples, when only considering the first-neighbor shell of phosphorus.

The higher  $\sigma^2$  and  $R$  values of the as-implanted sample compared to the annealed ones are consistent with the observation that the former is amorphous and the latter are crystalline. This is also supported by the fact that the higher order shells (3-4 Å) are visible above noise level for the annealed samples and they are absent in the as-implanted sample (Fig. 4.5(b)). The higher  $\sigma^2$  for 0.50 J/cm<sup>2</sup> than for 0.40 J/cm<sup>2</sup>, although within an error, is consistent with the observation that 0.40-0.45 J/cm<sup>2</sup> produces optimal crystallinity, and that 0.50 J/cm<sup>2</sup> and higher result in increasing structural disorder.

### 4.3.2 Magnetic properties

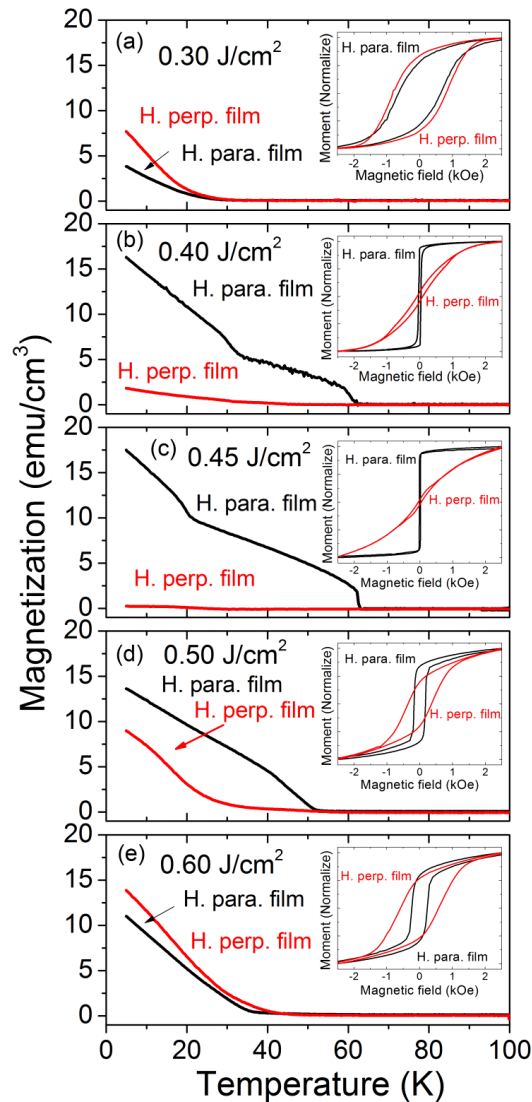


Fig. 4.6 The temperature dependence of the remnant magnetization and hysteresis loops (the insets) taken at 5 K for two sample orientations: with the magnetic field  $H$  parallel (black) and perpendicular (red) to the film at different pulsed laser annealing energy density of (a) 0.30, (b) 0.40, (c) 0.45, (d) 0.50, and (e) 0.60 J/cm<sup>2</sup>.

The temperature dependence of thermos-remnant magnetization (TRM) and M-H loops measured for two: in-plane and perpendicular orientations for all the samples annealed at various laser energy densities are shown in Fig. 4.6, and the presented there behavior gives direct evidence of a strong correlation between the microstructure (hence the PLA conditions) and the magnetic properties. The TRM measurements were carried out at near zero field condition on increasing temperature after the samples were cooled down to base temperature (5 K) at saturating magnetic field of 1 kOe. At such experimental conditions the temperature at which a non-zero TRM signal drops to zero defines the Curie temperature ( $T_C$ ) for the system and the relative strength of the TRM signals obtained at both experimental orientations below

this point hint about the strength of the out-of-plane uniaxial magnetic anisotropy.

The data collected in Fig. 4.6 clearly indicate that both the Curie temperature and the uniaxial magnetic anisotropy strongly vary in identically implanted samples but subjected later to PLA performed at different annealing energy densities. This fact univocally points to the decisive role of the PLA parameters on the resulting magnetic characteristics in the processed layers, which eventually determine the magnetic (or spintronics) figure of merit. Undoubtedly, the best characteristics are seen for samples,  $T_C \sim 62$  K. Also their highly square-like and sharp hysteresis loops along the in-plane direction indicate a strong IMA. The existence of the IMA in III-Mn-V compressively epitaxially strained DFS layers with  $T_C$  in excess of 20 K goes in hand with the theoretical predications for these systems [133], as well as experimental findings [23, 107], and confirms their high epitaxial quality. All the other samples exhibit inferior magnetic characteristics, their M-H loops are much more S-like and anisotropic properties deteriorate more the more energy density deviates from the 0.40-0.45 J/cm<sup>2</sup> level. It should be underlined here that, as shown in the previous sections, the same 0.40-0.45 J/cm<sup>2</sup> level of energy density results also in the best crystallographic composure of the layers, indicating that the magnetic fidelity of the ion implanted layers is in reality determined by the degree of their crystallinity, the PLA conditions set the latter which ultimately determines the former. Finally, we note a pronounced kink at the TRM seen at 20 or 30 K for energy density, 0.40 and 0.45 J/cm<sup>2</sup> samples. As described in Chapter 3, a similar kink has been observed in (Ga,Mn)As samples with homogenous Mn distribution, and it is due to the spin reorientation in a single domain [185]. Such a reorientation occurs in the compensated (Ga,Mn)As, resulting from a switching of the magnetic anisotropy. However, in our samples, we did not observe the changing of magnetic anisotropy upon increasing temperature. In our (Ga,Mn)P samples, it is probably due to the tail part of the Gaussian Mn distribution who has a lower  $T_C$ . As explained below, its presence strongly signalizes a more complex magnetic structure of these layers.

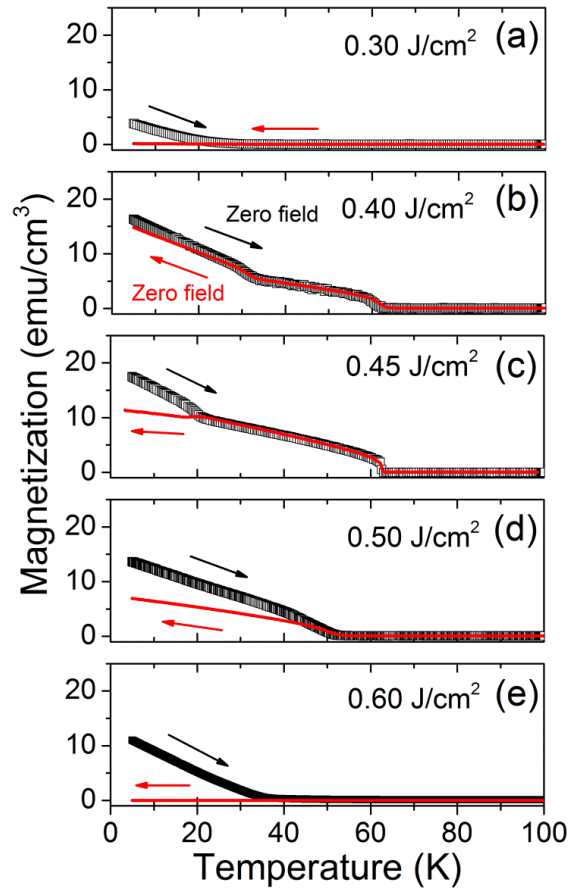


Fig. 4.7 M-T curves collected in absence of the external field: black squares are obtained on increasing temperature (the thermos-remnant magnetization, obtained after initial cooling at  $H = 1$  kOe), and the red solid lines were collected on decreasing temperature for the same set of samples as in Fig. 4.6, as indicated in the labels.

A certain non-random distribution of Mn atoms and sizable fluctuation of the local carrier density of states are the immanent features of DFS. Whereas the former may lead to complete structural and hence magnetic phase separation in certain systems [134]. The latter is an inherent property of all DFS due to their proximity to the metal insulator transition and a presence of a surface depleted layer [13]. These lead to the co-existence of the ferromagnetic (FM) and superparamagnetic-like (SP) components, which usually shows strong blocking behavior at low temperature, says below 20-30 K in most cases. The fact, that this SP property is hole density related was shown in thin (Ga,Mn)As film, where an electrical-gate-introduced carriers successfully mediated this SP part to the ferromagnetic one [13]. In general it remains hard to decisively tell one component from another, however as shown in Ref. [13], a real strength of both components in a specimen can be assessed by zero-field temperature cycling of the sample to its characteristic temperature, usually above and below a temperature at which an appreciable magnetic signal is still observed. The method relies on a temperature agitated nonreversible removal of the blocked SP moment,



and a full reversibility of the ferromagnetic material characterized with a strong uniaxial magnetic anisotropy.

The results of such an experiment are collected in Fig. 4.7 for all the samples in this study. The samples were initially cooled at a saturated field of 1 kOe down to 5 K where the field was set to zero and the warming up to 100 K commenced. This part of the test marked by black squares is in fact the TRM measurement already presented in Fig. 4.7. Then, the samples were re-cooled to 5 K at the same zero field condition (the red solid lines in Fig. 4.7). According to the argument given above, there should be no SP component in the recorded data, only a ferromagnetic spontaneous moment can contribute to the observed magnetic response. As a most general result of this test we note that magnetic signal recorded during re-cooling is weaker than in the remnant state. In fact there is no signal at the whole temperature range for the two outermost samples obtained for 0.30 and 0.60 J/cm<sup>2</sup>. This indicates that nearly the whole magnetism observed in these two layers has only a SP origin – no long range FM order is present there. We immediately invoke the fact that there are the two layers with the most inferior structural quality. On the other hand, for the two samples of the superior structural quality (0.40 and 0.45 J/cm<sup>2</sup> annealed samples) the moment recorder during re-cooling nearly completely reproduces the TRM one. This fact indicates that the magnetism of these two layers has predominantly long range FM origin, and combined with their high  $T_C$  values, which stay in a direct proportionality to the hole concentration further implies that the electrical disorder is the smallest in these two layers [2]. However, as indicated in panel (c) not the whole moment got restored upon recooling of the sample. This may result from the existence of a polycrystalline surface region (see Fig. 4.2(d)). It is quite feasible to assume that the nm-sized isolated volumes of the material, while undergoing the same long range coupling mechanism, behave SP since the coupling is spatially limited there by the polycrystalline morphology. Accordingly, cf. Figs 4.2(e) and 4.2(d), when these crystallites grow bigger the larger part of the layers acquires SP properties and the difference between the TRM and recooling M-T gets bigger. For the 0.60 J/cm<sup>2</sup> case, the fully polycrystalline form of this (Ga,Mn)P layer results in a complete domination of SP in the magnetic response in this sample. It is worth noting that the results could also be explained by the domain size changing upon changing laser energy: For the 0.4 J/cm<sup>2</sup> laser treated sample, the overlapping of the TRM and recooling M-T curves indicates a single domain structure in the layer. However, for the 0.45 and 0.5 J/cm<sup>2</sup> annealed samples, the partially increased cooling M-T curves present the development of the multi-domain structure. Interestingly, the SP behaviors in 0.3 and 0.6 J/cm<sup>2</sup> annealed samples indicate the fact that the domain size decreases to nano-meter range.

It is worth noting that the variation of other laser conditions (including pulsed

duration, laser wavelength, and annealing times) could also influence the structure, magnetic and electrical properties of prepared materials, *e.g.*, for (Ga,Mn)As, the annealing by 10 laser pulses is detrimental to the magnetic properties (both magnetic moment and the Curie temperature) when compared with the single pulse annealed sample [103]. On the other hand, the Mn concentration is of importance in the magnetic properties [60]. However, in this work, the other parameters are all fixed, and only laser energy was treated variable.

#### **4.4 Conclusion**

In summary, by various technologies, we prove the epitaxial regrowth of a (Ga,Mn)P layer on GaP substrate after optimal pulsed laser annealing at  $0.40 \text{ J/cm}^2$ . Moreover, annealing at higher energy densities induces the formation of defects, which is mainly responsible for decreasing of the Curie temperature and the weakening of the uniaxial magnetic anisotropy. Thus, we show a strong correlation between the microstructures and the magnetic properties in (Ga,Mn)P prepared by Mn ion implantation and subsequent pulsed laser annealing. Meanwhile, this fact univocally points to the decisive role of the PLA parameters on the resulting magnetic characteristics in the processed layers, which eventually determine the magnetic (or spintronics) figure of merit.



## Chapter 5

### High $T_C$ and PMA in homo-epitaxial (In,Mn)As films

This chapter has been published as:

Y. Yuan *et al.*, J. Phys. D: Appl. Phys., **48**, 235002 (2014)

We have prepared the dilute magnetic semiconductor (DMS) (In,Mn)As with different Mn concentrations by ion implantation and pulsed laser melting. The Curie temperature of the  $\text{In}_{1-x}\text{Mn}_x\text{As}$  epilayer depends on the Mn concentration  $x$ , reaching 82 K for  $x=0.105$ . The substitution of Mn ions at the indium sites induces a compressive strain perpendicular to the (In,Mn)As layer and a tensile strain along the in-plane direction. This gives rise to a large perpendicular magnetic anisotropy, which is often needed for the demonstration of electrical control of magnetization and for spin-transfer-torque induced magnetization reversal.

#### 5.1 Introduction

Studies focusing on the preparation of III-V dilute ferromagnetic semiconductors (DFS) exhibiting a high Curie temperature ( $T_C$ ) have been greatly inspired due to potential applications in spintronic devices [2, 99, 135-137]. The carrier mediated nature of the ferromagnetism in DFS allows for controlling the magnetic properties (Curie temperature, anisotropy and etc.) by an electric field [12, 53]. Current induced domain wall switching and motion have been demonstrated in (Ga,Mn)As [52, 99, 137] and (Ga,Mn)(As,P) quaternary alloy [138-140]. In those investigations, a perpendicular magnetic anisotropy (PMA) is required for the ferromagnetic semiconductors [52, 138-140]. Homoepitaxial (Ga,Mn)As on GaAs substrate normally exhibits in-plane magnetic anisotropy due to the compressive strain along its in-plane direction. The PMA in (Ga,Mn)As has been realized by two approaches: The mostly used one is to tune the strain from compressive to tensile state in (Ga,Mn)As either by applying (In,Ga)As as buffer [52, 138] or by co-alloying (Ga,Mn)As with phosphorus [139-142]. The other one is to change the localization of holes in the (Ga,Mn)As layer, by co-alloying Al [143-146]. Different from (Ga,Mn)As, homoepitaxial (In,Mn)As on InAs is subject to tensile strain along its in-plane direction, therefore, should exhibit PMA. Moreover, ferromagnetic (In,Mn)As films

in principle provide a more suitable test-bed for current induced magnetic switching in magnetic semiconductors due to its larger spin-orbit coupling [147].

The preparation of (In,Mn)As by low-temperature molecular beam epitaxy (LT-MBE) was not satisfactory in the early stage: the large lattice mismatch between the layer and the substrate results in a large amount of  $n$ -type defects, which are detrimental to magnetization and suppress  $T_C$  [55, 148]. Schallenberg and MuneKata prepared recently (In,Mn)As with the highest  $T_C$  of 90 K through LT-MBE by carefully selecting a buffer layer [56]. However, once the strain is completely relaxed, the PMA is lost in the (In,Mn)As layer. So far, the highest  $T_C$  of (In,Mn)As films with PMA is around 72 K when the Mn concentration reaches to 10% grown on an AlSb buffer by LT-MBE [56], i. e. still below the liquid nitrogen temperature. Thus, the preparation of (In,Mn)As with PMA and a higher  $T_C$  (above the liquid nitrogen temperature in the view of technical practice) is still challenging and interesting especially when it is prepared through a simple and versatile method.

In this letter, we present the preparation of homoepitaxial (In,Mn)As on InAs by ion implantation and pulsed laser melting. We show that a highest  $T_C$  of 82 K is achieved in  $\text{In}_{1-x}\text{Mn}_x\text{As}$  with PMA at a Mn concentration of  $x=0.105$ . The magnetic anisotropy in (In,Mn)As is confirmed by magnetization and X-ray magnetic circular dichroism (XMCD) measurements. The pronounced PMA in this system is attributed to the tensile strain in the in-plane direction of (In,Mn)As arising from the Mn ion incorporation.

## 5.2 Experiment methods

(In,Mn)As epilayers with different Mn concentrations were prepared by Mn ion implantation and pulsed laser melting on InAs (001) substrates. First, Mn ions were implanted into intrinsic InAs substrates with an energy of 100 keV. According to SRIM simulation, the projected range ( $R_p$ ) and the longitudinal straggling ( $\Delta R_p$ ) for Mn distribution are around 60 and 38 nm, respectively. The Mn fluences ( $\Phi$ ) were  $4 \times 10^{15}$ ,  $8 \times 10^{15}$ ,  $1.6 \times 10^{16}$ ,  $2.4 \times 10^{16}$ , and  $2.8 \times 10^{16}$   $\text{cm}^{-2}$ . A XeCl excimer laser (Coherent ComPexPRO201, wavelength of 308 nm and pulse length of 30 ns) with an energy density of  $0.30 \text{ J/cm}^2$  was used for annealing the (In,Mn)As samples. After the pulsed laser annealing and HCl etching, the remaining Mn fluences determined by particle induced X-ray emission (PIXE) using 3 MeV protons are  $3.25 \times 10^{15}$ ,  $7.26 \times 10^{15}$ ,  $1.18 \times 10^{16}$ ,  $1.48 \times 10^{16}$ , and  $1.78 \times 10^{16}$   $\text{cm}^{-2}$ , respectively. The virtual Mn concentration can be calculated by  $\Phi/\sqrt{2\pi}\Delta R_p$ . According to the remaining fluence, the Mn concentration  $x$  ( $\text{In}_{1-x}\text{Mn}_x\text{As}$ ) is determined to be 0.019, 0.042, 0.069, 0.087, and 0.105, respectively. Magnetic properties were measured by a Superconducting Quantum Interference Device (SQUID) magnetometer (Quantum Design,

SQUID-VSM). Synchrotron radiation X-ray diffraction (SRXRD) was performed on the InMnAs samples at the BM20 (ROBL) beamline at the European Synchrotron Radiation Facility (ESRF). It was using a wavelength of  $\lambda=1.0781 \text{ \AA}$ . X-ray absorption spectroscopy (XAS) measurements were performed at the beamline UE46/PGM-1 at BESSY II (Helmholtz-Zentrum Berlin). A magnetic field up to 1 T was applied parallel or anti-parallel to the photon helicity and the samples were rotated from perpendicular to the field to different angles. Before XAS measurements, all the samples were dipped in HCl solution to remove the native oxide layer from the surface.

## 5.3 Results and discussion

### 5.3.1 Magnetism

Figure 5.1(a) represents the results of magnetic field dependent magnetization measured at 5 K for (In,Mn)As with different Mn concentrations. Note that the diamagnetic background is subtracted from the data shown in Fig. 5.1(a). All samples were annealed with an energy density of  $0.30 \text{ J/cm}^2$ . The magnetic field is applied perpendicular to the layer (i.e. the field is parallel to the (In,Mn)As [001] axis). At a magnetic field of 300 Oe, all the samples attain their saturation magnetization, and exhibit square-like hysteresis loops which indicate that the out-of-plane direction is the magnetic easy axis for all samples. The magnetic remanence as a function of temperature is plotted in Fig. 5.1(b) for three samples. The samples were cooled down from room temperature under a magnetic field of 1000 Oe. Then the field was decreased to 20 Oe, which should compensate the possible residual field of the superconducting magnet. The magnetic remanence ( $M_r$ ) was measured during warming up. From the remanence measurements,  $T_C$  around 14, 40, and 77 K for  $x=0.019$ , 0.042, and 0.069 for  $\text{In}_{1-x}\text{Mn}_x\text{As}$  samples, respectively, are obtained. The inset to Fig. 5.1(b) shows the behavior of  $M_r(T)/M_r(5\text{K})$  as a function of  $T/T_C$ , and the curves follow the mean-field-like approximation [103]. This also indicates that a lot of Mn ions replace Indium ions resulting in a large hole concentration which eventually induces carrier mediated ferromagnetism in (In,Mn)As.

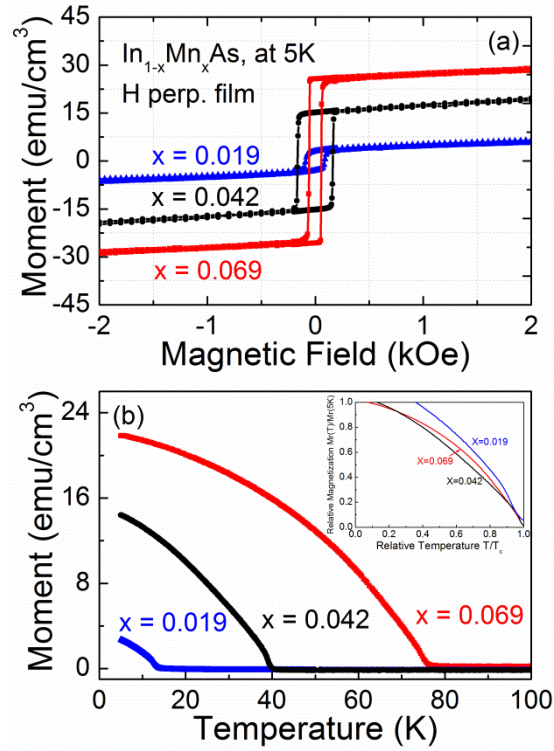


Fig. 5.1 (a) Magnetization of  $\text{In}_{1-x}\text{Mn}_x\text{As}$  samples measured at 5 K in the out-of-plane geometry: The Mn concentrations are:  $x=0.019$  (triangle), 0.042 (circle), and 0.069 (square); (b) Remanent magnetization as a function of temperature measured under a magnetic field of 20 Oe after the samples were saturated by applying 1000 Oe along the perpendicular direction for the three samples. The inset shows the plots of  $M_r(T)/M_r(5\text{K})$  as a function of  $T/T_C$ .

We increased the Mn implantation fluence to check if we can obtain higher Curie temperature. Figure 5.2(a) shows the relationship between the remaining Mn fluence determined by PIXE and the nominal implantation fluence. At the low fluence regime, most of implanted Mn ions are remaining in the InAs matrix, however, the remaining fraction is drastically decreased with increasing implantation fluence. This large reduction is mainly due to the partitioning at the solid/liquid interface during pulsed laser annealing. In the case of Mn implanted GaAs and GaP, it was found that around 50% Mn can be rejected. Moreover, at large ion fluence the sputtering effect arises and sets the upper limit for the Mn concentration to be implanted [149]. The Curie temperature and magnetization of  $\text{In}_{1-x}\text{Mn}_x\text{As}$  samples as a function of Mn concentration  $x$  are displayed in Fig. 5.2(b). The Curie temperature monotonically increases from 14 to 77 K when  $x$  is from 0.019 to 0.069. However, the Curie temperature seems to saturate at around 82 K with further increasing Mn concentration up to 0.105. So far, the highest  $T_C$  in (In,Mn)As with PMA is achieved in our sample, i.e., 82 K, which is accessible by liquid nitrogen cooling. Meanwhile, the same saturation tendency is seen for the magnetization at 5 K shown in Fig.

5.2(b).

We also calculate the saturation magnetization per Mn by assuming that all remaining Mn ions substitute on the Indium sites. Except for the sample with  $x$  of 0.019, the saturation magnetization is calculated to be between 2.3 and 2.5  $\mu_B/\text{Mn}$ . It is smaller than the theoretical value for (Ga,Mn)As ( $\sim 4 \mu_B/\text{Mn}$ ) [150], however comparable with the experimental values ( $\sim 2 \mu_B/\text{Mn}$  in Ref. [150] and  $\sim 3 \mu_B/\text{Mn}$  in Ref. [101]) for the state-of-art (Ga,Mn)As films. In reality, the substitutional concentration of Mn should be smaller than what we determined by PIXE and there are always defects (for instance As antisites [150]) compensating the holes. Both facts lead the underestimation for the magnetization in term of  $\mu_B/\text{Mn}$ . Indeed, the saturation magnetization is comparable to those obtained for (Ga,Mn)P (2.8  $\mu_B/\text{Mn}$ ) and (Ga,Mn)As (3.4  $\mu_B/\text{Mn}$ ) epilayers prepared by ion implantation [59, 106, 115].

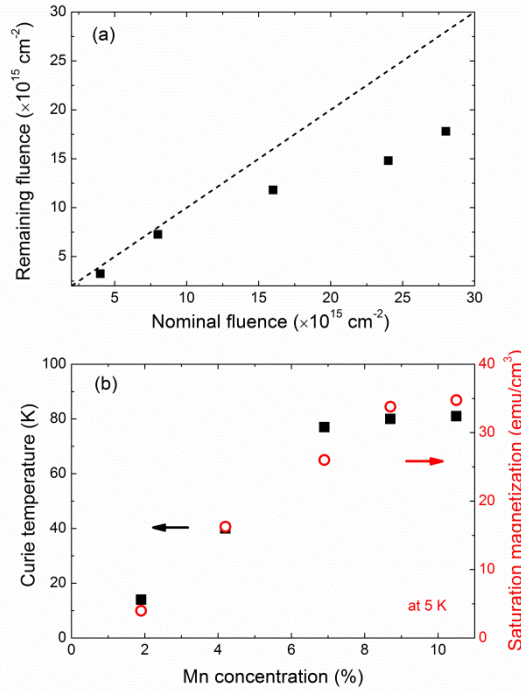


Fig. 5.2 (a) The remaining Mn fluence determined by PIXE vs. the nominal Mn implantation fluence. The dashed line shows the 1:1 relation. (b) Curie temperature and magnetization of  $\text{In}_{1-x}\text{Mn}_x\text{As}$  samples measured as a function of Mn concentration  $x$ . The five samples in (b) are the same as shown in (a).

### 5.3.2 Magnetic anisotropy

Figure 5.3 shows the magnetic hysteresis loops (normalized) of  $\text{In}_{0.931}\text{Mn}_{0.069}\text{As}$  measured at 5 K in two configurations *e.g.*, when the field is applied parallel to the [001] direction (out-of-plane) or [1-10] direction (in-plane). A clear square-like hysteresis loop is observed when the magnetic field is applied along (In,Mn)As [001] direction. It saturates at a low magnetic field compared to another field configuration



(parallel to the sample plane). This again proves that the  $\text{In}_{0.931}\text{Mn}_{0.069}\text{As}$  sample has an out-of-plane magnetic easy axis. By using the equation  $H_d = 4\pi M_S$ , where  $M_S$  is the saturation magnetization ( $26 \text{ emu/cm}^3$  for  $\text{In}_{0.931}\text{Mn}_{0.069}\text{As}$ ), we can calculate the demagnetizing field induced by the shape anisotropy to be 0.32 kOe. The lowest-order uniaxial magnetic anisotropy field induced by strain is 2.16 kOe obtained by the equation  $H_{u\perp} = [M_S/(dM/dH)_{H=0}] + H_d$  [146]. Different from the homoepitaxial (Ga,Mn)As on GaAs synthesized by LT-MBE, our samples do not show any temperature dependent magnetic anisotropy [151]. Note that the substitution of Indium by Mn results in a smaller lattice constant and compressive strain along the (In,Mn)As [001] axis, and this strain is mainly responsible for the uniaxial perpendicular magnetic anisotropy [23]. Due to the biaxial compressive strain, the valence band splits and the lowest valence band assumes a heavy-hole character. The hole spins are oriented along the growth direction when only the lowest valence band is occupied, since in this case it can lower their energy by coupling to the Mn spins and PMA is expected [151].

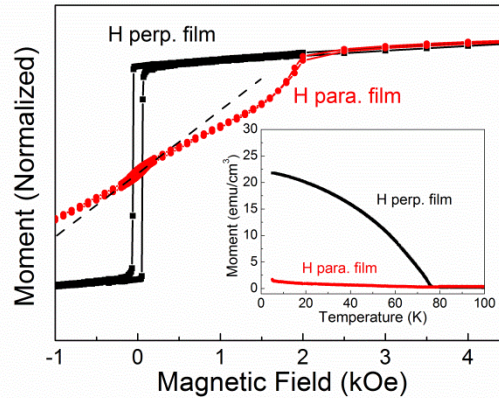


Fig. 5.3 Magnetic field dependence of magnetization of  $\text{In}_{0.931}\text{Mn}_{0.069}\text{As}$  with the field perpendicular to the surface (along (In,Mn)As [001]): square and parallel to the surface: circle, at 5 K. The inset shows the remanent magnetization vs. temperature for the different orientations.

The most probable secondary phase is MnAs, like in the case of Mn implanted GaAs upon rapid thermal annealing [152, 153]. For bulk MnAs or nanocrystalline MnAs in GaAs, the Curie temperature is above 300 K [152, 153]. As shown in Fig. 5.1(b) and Fig. 5.3, there is no indication of secondary magnetic phase with a higher  $T_C$ . Moreover, nanocrystalline MnAs embedded in GaAs reveals an easy axis along the in-plane of the film [152, 153]. Therefore, the ferromagnetism in the (In,Mn)As film is intrinsic and the perpendicular magnetic anisotropy is due to the strain. The existence of strain is proved by XRD (see Fig. 5.4) and is also in agreement with the mean-field theory for dilute ferromagnetic semiconductors [23].

### 5.3.3 Structures

The crystalline structure of the homoepitaxial (In,Mn)As is investigated using XRD. The  $\theta$ - $2\theta$  scan around the InAs (004) reflection in Fig. 5.4(a) shows a broad (In,Mn)As peak located at a higher angle than the InAs (004) peak. It means that the (In,Mn)As layer is under a compressive strain along the out-of-plane direction. The presence of X-ray Pendellösung fringes around InAs (004) proves a good crystalline quality of the (In,Mn)As layer. In order to get more detailed information about the structure of (In,Mn)As, a simulation is performed to fit the experimental XRD data of  $\text{In}_{0.931}\text{Mn}_{0.069}\text{As}$  as shown in Fig. 5.4(a). The fitting reveals a compressive strain  $(a-a_0)/a_0$  of -0.19% for the  $\text{In}_{0.931}\text{Mn}_{0.069}\text{As}$  layer.

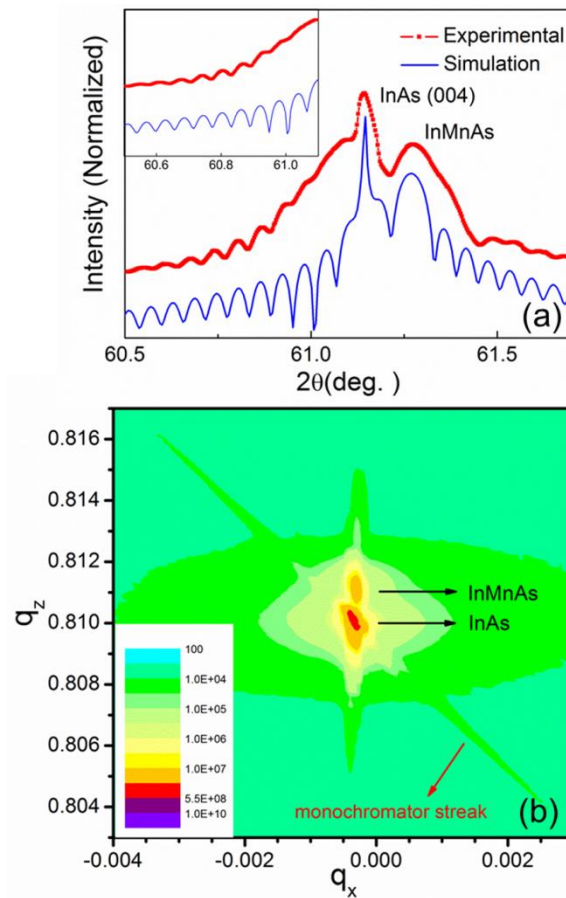


Fig. 5.4 (a)XRD  $\theta$ - $2\theta$  scan (square) and simulation (line) of the (004) reflection for  $\text{In}_{0.931}\text{Mn}_{0.069}\text{As}$  sample (the data have been transformed to  $\lambda=1.54056 \text{ \AA}$ ); (b) Reciprocal space map (RSM) around the (422) reflection.

Figure 5.4(b) shows the reciprocal space map (RSM) for the (422) reflection from the sample  $\text{In}_{0.931}\text{Mn}_{0.069}\text{As}$ . Similar to the (004) reflection, a characteristic (In,Mn)As peak appears at a larger  $q_z$  in the (422) reflection. The peak is located at the same  $q_x$  as the InAs (442) peak. This shows that the (In,Mn)As layer is fully strained on the InAs substrate. The XRD results prove that the (In,Mn)As layer on InAs substrate exhibits

a compressive strain along the perpendicular direction and the strain is not relaxed.

### 5.3.4 X-ray magnetic circular dichroism (XMCD)

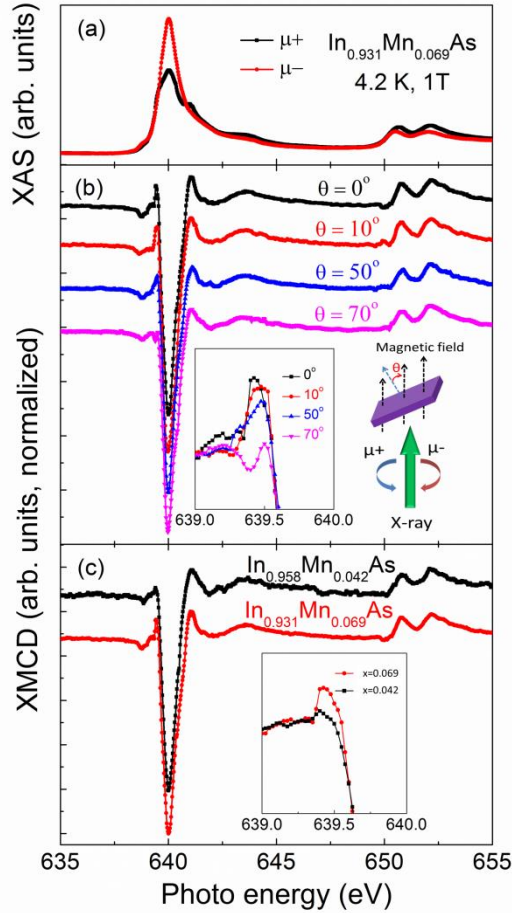


Fig. 5.5 (a) XAS in parallel ( $\mu^+$ ) and antiparallel ( $\mu^-$ ) configurations for  $\text{In}_{0.931}\text{Mn}_{0.069}\text{As}$  measured at 4.2 K under an external field of 1 T applied parallel to the layer surface-plane. (b) XMCD spectra: the sample was rotated from  $\theta=0^\circ$  (the magnetic field is applied perpendicular to the sample surface-plane, schematically shown as the right inset) to  $\theta=70^\circ$ . The inset shows the zoom at the Mn  $L_3$  pre-edge at different angles. (c) XMCD spectra at  $\theta=0^\circ$  for  $\text{In}_{1-x}\text{Mn}_x\text{As}$  films with  $x=0.042$  (square) and  $x=0.069$  (circles). The inset shows the Mn  $L_3$  pre-edge of (In,Mn)As films with different Mn concentrations.

Figure 5.5(a) shows the XAS results of  $\text{In}_{0.931}\text{Mn}_{0.069}\text{As}$  at the Mn  $L_{2,3}$  edges measured in the total electron yield (TEY) mode under a magnetic field of 1 T at 4.2 K. The features around 640 eV and 651 eV correspond to the  $L_3$  ( $2p_{3/2}$  to 3d) and  $L_2$  ( $2p_{1/2}$  to 3d) levels, similar to the situation of (Ga,Mn)As [154]. We did not observe any pronounced multiplet structure around the  $L_3$  edge which indicates that the HCl etching has effectively removed the oxide layer from the (In,Mn)As surface. The XMCD was already estimated in our earlier work, where the maximum asymmetry was around 51 % at the  $L_3$  edge [54]. Tensile strain exists in the in-plane direction and compressive in the out-of-plane direction, which leads to a large uniaxial anisotropy.

This uniaxial magnetic anisotropy is related to the special feature in the pre-edge region at 0.5 eV below the  $L_3$  peak in the XMCD spectrum [145, 155, 156]. Figure 5.5(b) presents the angular dependence of the XMCD spectrum of  $\text{In}_{0.931}\text{Mn}_{0.069}\text{As}$ , where the angular  $\theta$  is varied from  $0^\circ$  (normal incidence) to  $70^\circ$  (grazing incidence). When rotating the sample from normal to grazing angle, the height of the pre-edge shoulder decreases, which means the compressive strain transforms to tensile strain from the out-of-plane to the in-plane direction. This behavior is similar to other DFS materials, *e.g.*  $(\text{Ga,Mn})\text{As}$  and  $(\text{Ga,Mn})(\text{As,P})$  [155, 156], which have a compressive strain along the perpendicular or parallel direction. Figure 5.5(c) displays the XMCD spectra (normalized at the Mn  $L_3$  peak) for  $\text{In}_{1-x}\text{Mn}_x\text{As}$  samples with  $x=0.042$  and  $0.069$  at a normal incident angular. An increase in the pre-edge shoulder indicates that more Mn ions are incorporated into the  $(\text{In,Mn})\text{As}$  lattice which results in a larger compressive strain along the perpendicular direction.

Another evidence to prove the carrier-mediated nature of the ferromagnetism in  $(\text{In,Mn})\text{As}$  layers is magneto-transport. However, due to the narrow bandgap of  $\text{InAs}$ , the substrate is highly conductive, preventing magneto-transport measurements for the  $(\text{In,Mn})\text{As}$  layer. The conducting  $\text{InAs}$  substrate with a large carrier mobility also results in strong Shubnikov-de Haas oscillations in the ferromagnetic resonance (FMR, not shown), over-dominating the features of the  $(\text{In,Mn})\text{As}$  layer. Otherwise, the Gilbert damping coefficient can be obtained by FMR. The Gilbert damping coefficient is an important parameter for spintronics and has been determined to be in the range of 0.12-0.24 for  $(\text{Ga,Mn})\text{As}$  [50].

## 5.4 Conclusion

In summary, we have prepared ferromagnetic  $(\text{In,Mn})\text{As}$  with a perpendicular magnetic anisotropy and a high Curie temperature up to 82 K. The XMCD results also confirm the existence of a perpendicular magnetic anisotropy in  $(\text{In,Mn})\text{As}$  epilayers. To our knowledge, this is the highest  $T_C$  recorded for  $(\text{In,Mn})\text{As}$  with perpendicular magnetic anisotropy. The good crystalline quality of these epilayers is confirmed by the appearance of the Pendellösung fringes around the  $\text{InAs}$  (004) peak in the XRD pattern and by the square-like hysteresis loops along the magnetic easy axis. The inner strain induced by the Mn ion substitution in the  $(\text{In,Mn})\text{As}$  epilayers is responsible for the appearance of a perpendicular magnetic anisotropy.



## Chapter 6

### Interplay between localization and magnetism in (Ga,Mn)As and (In,Mn)As

This chapter is prepared for publication:

Ye Yuan *et al.*, Interplay between localization and magnetism in (Ga,Mn)As and (In,Mn)As, to be submitted (2017)

Although the interplay between hole-mediated ferromagnetism and hole localization has long been recognized as the central issue in dilute ferromagnetic semiconductors (DFSs), its understanding remains in a nascent stage and contradicting approaches are under consideration. Here, we examine the influence of localization on the hole-mediated ferromagnetism in two DFSs with a differing strength of  $p$ - $d$  coupling, (Ga,Mn)As and (In,Mn)As, and obtained by a method resulting in the absence of compensating donors. On the insulating side of the transition, ferromagnetic signatures persist to higher temperatures in (In,Mn)As compared to (Ga,Mn)As with the same Mn concentration. This substantiates theoretical suggestions that stronger  $p$ - $d$  coupling results in an enhanced contribution to localization, which reduces hole-mediated ferromagnetism. Furthermore, our findings support strongly the heterogeneous model of electronic states at the localization boundary and point to the crucial role of weakly localized holes in mediating efficient spin-spin interactions even on the insulator side of the metal-insulator transition.

## 6.1 Introduction

Although the interplay between hole-mediated ferromagnetism and hole localization has long been recognized as the central issue in dilute ferromagnetic semiconductors (DFSs) [13, 14, 38, 45, 49, 112, 157-164], its understanding remains in a nascent stage and contradicting approaches are under consideration [2, 13, 14, 38, 39, 157, 160, 165]. One of the reasons is a strong dependence of localization and key magnetic properties on the concentration of poorly controlled donor defects, such as – in the most thoroughly studied system, i.e., (Ga,Mn)As – Mn interstitials [2] and As antisites [166]. Another reason of the slow progress towards a consensus is an intricate nature, even in non-magnetic semiconductors, of the metal-insulator transition (MIT). In particular, characteristic length scales are too large to allow the MIT to be treated by available *ab initio* methods, whereas theoretical tools, such as the renormalization group formalism, provide merely critical exponents and quantum corrections brought about by diffusion poles, rather than the absolute values of experimentally available quantities [167].

In this paper we present results of systematic charge transport and magnetic studies on a series of  $\text{Ga}_{1-x}\text{Mn}_x\text{As}$  and  $\text{In}_{1-x}\text{Mn}_x\text{As}$  films obtained by Mn ion implantation into semi-insulating GaAs and intrinsic InAs wafers, respectively, followed by subsequent pulsed laser melting (PLM). Neither Mn interstitials nor As antisites are present in samples prepared in this way [168]. Under these rather unique conditions we explore the interplay of magnetism and quantum localization in the Mn concentration range  $x$  from 0.3 to 1.8%, which covers both sides of the MIT. We demonstrate in a quantitative fashion how the system evolves with  $x$  from a paramagnetic (PM) phase (probed down to 1.8 K), to a superparamagnetic (SPM) material, to reach, *via* a mixed phase consisting of percolating ferromagnetic clusters and superparamagnetic grains, a global ferromagnetism (FM) without any superparamagnetism. The absence of superparamagnetism for  $x \geq 1.4\%$  makes our samples, grown by PLM, different from those obtained by molecular beam epitaxy (MBE), in which the measurement procedure employed here reveals often a superparamagnetic component even in films with higher  $x$  [13, 49]. Furthermore, the absence of compensation allows us to determine the hole concentration directly from  $x$ , which enables us to test the *p-d* Zener model quantitatively. We find excellent agreement between our experimental data and the theoretical prediction [14]. A worthwhile finding of our work is a clear demonstration that the *p-d* interaction enhances the hole localization and, thus, diminishes hole-mediated coupling. This results in a *weaker* ferromagnetic signature in the range of low Mn concentrations in (Ga,Mn)As compared to (In,Mn)As in which hole localization is weaker.

## 6.2 Methods

### Sample preparation

The (Ga,Mn)As and (In,Mn)As samples for this study were prepared by Mn ion implantation into semi-insulating GaAs and intrinsic InAs wafers, respectively, followed by subsequent pulsed laser melting (PLM). The implantation energy was 100 keV, and the wafer normal was tilted by  $7^\circ$  with respect to the ion beam to avoid channeling. According to the stopping and range of ions in matter (SRIM) simulation, the longitudinal straggling ( $\Delta R_p$ ) for the Mn distribution in GaAs and InAs is around 31 and 38 nm, respectively. A Coherent XeCl laser (with 308 nm wavelength and 28 ns pulse duration) was employed to recrystallize the samples, and the energy densities were optimized to achieve both the highest crystalline quality and the best randomization of the Mn distribution:  $0.3 \text{ J/cm}^2$  for (Ga,Mn)As and  $0.2 \text{ J/cm}^2$  for (In,Mn)As.

### Secondary-ions mass spectrometry (SIMS)

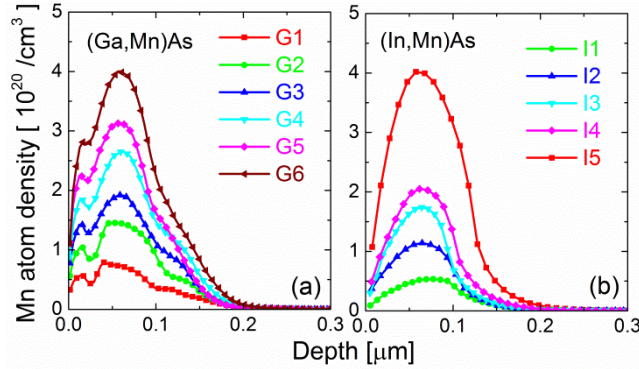


Fig. 6.1 Concentration profiles of Mn in (Ga,Mn)As and (In,Mn)As – SIMS measurement.

Mn concentration profiles were characterized with secondary ions mass spectrometry (SIMS) technique using Cameca IMS 6F microanalyser. SIMS measurement was performed with cesium ( $\text{Cs}^+$ ) primary beam. Mn concentrations were derived from the intensity of  $\text{MnCs}^+$  clusters. Atomic concentration of manganese was calculated on the base of implantation dose and range. The Mn distribution is approximately Gaussian in both (Ga,Mn)As and (In,Mn)As. The Mn concentration  $x$  relevant for the measured  $T_C$  is taken as an average  $x$  within the coherence length (which is of the order of 5 nm) in the regime with maximal  $x$ , as  $T_C$  is determined by the peak Mn concentration in a given sample [2, 13].

### Magnetic and electrical property measurements

Magnetic properties were studied employing a Quantum Design MPMS XL Superconducting Quantum Interference Device (SQUID) magnetometer equipped with a low field option. For the thermo-remnant magnetization (TRM – the temperature dependence of the remnant magnetization measured upon warming)



measurements, the samples were cooled down under a field of 1 kOe, then at the base temperature the field was switched off using a soft quench of the superconducting magnet and the system was warmed up while collecting data. When above the magnetic critical temperature ( $T_C$  – taken here as the temperature where the TRM vanishes), the samples were re-cooled to the starting temperature at the same zero-field conditions while the data recording was continued and entitled as spontaneous magnetization  $M_S$ . All the magnetic measurements were carried out using an about ~20 cm long silicon strip to fix the samples and the adequate experimental code for minute signals measurements was strictly observed [123]. The normalized magnetization per Mn atom was determined by dividing the magnetization by the total number of Mn ions obtained by integrating the distribution of the Mn concentration. The temperature dependent transport measurements were carried out using van der Pauw geometry in a Lakeshore Hall measurement G system.

### 6.3 Results

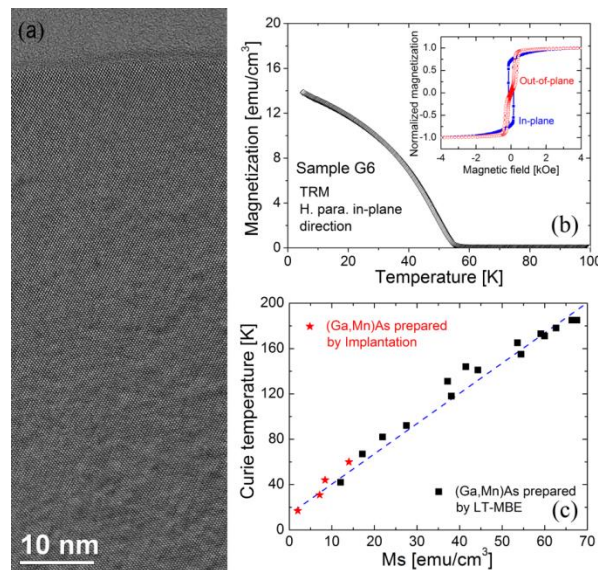


**Fig. 6.2 Structural (a) and magnetic properties (b,c) of (Ga,Mn)As epilayers prepared by ion implantation and PLM.** (a) A cross-sectional high-resolution TEM image of the (Ga,Mn)As sample with 1.8% Mn points to high quality and excludes the presence of any extended lattice defects, amorphous inclusions, and precipitates of another phases. Temperature dependence of magnetization (b), the character of magnetic anisotropy [inset to (b)], and the magnitude of Curie temperature at given spontaneous magnetization  $M_S$  in (Ga,Mn)As obtained by Mn implantation and PLM are identical to optimized (Ga,Mn)As films obtained by LT-MBE [101].

**Epitaxial (Ga,Mn)As covering the MIT regime.** We have prepared both (Ga,Mn)As and (In,Mn)As with very low Mn concentration, as shown in Table. 6.1. To verify the sample quality prepared by our method, we have characterized the samples regarding their structural and magnetic properties. As shown in Fig. 6.2a, the perfect lattice-fringe image in the cross-sectional high-resolution transmission electron

microscopy (HR-TEM) indicates that PLM leads to the complete epitaxial recrystallization in the (Ga,Mn)As layer whose Mn concentration is as high as 1.8%. For the same sample, a concave temperature dependent remnant magnetization (TRM) curve matches the description from the mean-field theory, as shown in Fig. 6.2b. Another convincing evidence to support the epitaxial nature of (Ga,Mn)As on the GaAs substrate is the uniaxial magnetic anisotropy as shown in the inset of Fig. 6.2b. Due to the tensile strain in the (Ga,Mn)As epilayer, an in-plane magnetic easy axis is desired which is the same as the low temperature annealed MBE grown samples.

The magnitude of Curie temperature ( $T_C$ ) in (III,Mn)V DSFs is expected to increase with the hole density  $p$  and an effective Mn concentration  $x_{\text{eff}}$  [14, 101]. The value of  $p$  is controlled by concentrations of substitutional Mn acceptors and compensating donors. In spatially uniform systems,  $x_{\text{eff}}$  is directly determined by the spontaneous magnetization  $M_S$ , and is typically smaller than  $x$  due to antiferromagnetic interactions, for instance, between substitutional and interstitial Mn ions [2, 101]. The determined values of  $x$  and  $T_C$  are summarized in Table 6.1 for our samples. In order to compare our  $T_C$  values to  $T_C(M_S)$  obtained for optimized thin MBE (Ga,Mn)As films [50,101] we take  $M_S = xN_0m_{\text{Mn}}$ , where  $N_0$  is the cation concentration and  $m_{\text{Mn}} = 4.0 \mu_B$  in the case of weak compensation, small magnitude of the hole orbital moment [169, 170], and large spin polarization of the hole liquid. As indicated in Fig. 6.2c our (Ga,Mn)As samples that show FM characteristics follow the trend  $T_C(M_S)$  established for thin films obtained by MBE and low-temperature annealing [101]

Tab. 6.1 The Mn concentration  $x$ , Curie temperature  $T_C$ , and characteristic temperatures of ferromagnetic grains  $T_\sigma$  of the  $\text{Ga}_{1-x}\text{Mn}_x\text{As}$  samples (denoted by G) and the  $\text{In}_{1-x}\text{Mn}_x\text{As}$  samples (denoted by I).

Sample No.	Mn concentration (%)	$T_C$ ( $T_\sigma$ ) (K)
G1	0.35	0
G2	0.66	(7.5)
G3	0.87	17 (13)
G4	1.2	31
G5	1.4	44
G6	1.8	60
I1	0.30	0
I2	0.63	(6)
I3	0.96	14 (11)
I4	1.2	23
I5	2.2	40

In doped semiconductors the critical carrier concentration corresponding to the MIT is usually well described by the Mott formula [2]:

$$p_c^{\frac{1}{3}} a_B = 0.26 \pm 0.05, \quad 6.1$$

$$a_B = \frac{e^2}{8\pi\epsilon_0\epsilon_r E_1}, \quad 6.2$$

where  $a_B$  is the effective Bohr radius,  $p_c$  is the critical hole concentration,  $e$  is the charge of single electron,  $\epsilon_r$  is the static dielectric constant,  $\epsilon_0$  is the vacuum permittivity, and  $E_1$  is the impurity binding energy. For Mn in GaAs,  $\epsilon_r = 12.9$ ,  $E_1 = 112.4$  meV, thus a critical concentration of  $p_c$  ranging from  $0.7 \times 10^{20}$  to  $2.4 \times 10^{20}$   $\text{cm}^{-3}$  is obtained [2, 171]. We compare this theoretical value to the hole concentrations in our samples assuming that each substitutional Mn atom delivers one hole,  $p \cong xN_0$ , where  $N_0 = 2.2 \times 10^{22}$   $\text{cm}^{-3}$  is the cation density in GaAs. The absence of compensation is proved by Rutherford backscattering channeling which showed that (Ga,Mn)As films prepared by ion implantation and PLM are free from Mn interstitial defects [103]. Moreover, owing to the high temperature nature of PLM, the formation of arsenic antisite defects can also be excluded [103]. Under these rather unique conditions we find that the values of  $p$  spans from  $8.8 \times 10^{19}$  to  $4 \times 10^{20}$   $\text{cm}^{-3}$  in samples G1 to G6, respectively. This means, in agreement with our resistance measurements discussed below, that our samples are probing both sides of the MIT. In addition to GaAs, the Mn binding energy of  $E_1 = 30$  meV in InAs and the static dielectric constant  $\epsilon_r = 12.3$  of InAs allow the calculation of the critical concentration of  $p_c$  in (In,Mn)As ranging from  $1.3 \times 10^{18}$  to  $4.0 \times 10^{18}$   $\text{cm}^{-3}$ .

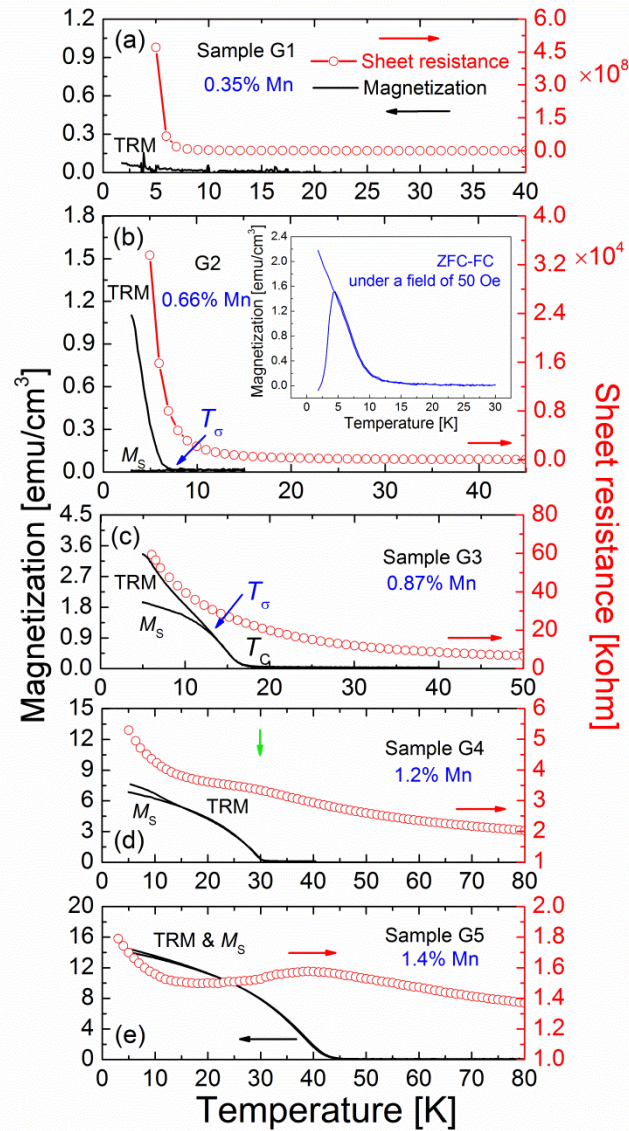


**Fig. 6.3** The interplay between localization and magnetism in (Ga,Mn)As in the vicinity of metal-insulator transition. Temperature dependence of remnant magnetization (lines, left axis) and sheet resistance (circles, right axis) of (Ga,Mn)As (samples G1-G5). The inset to (b) shows ZFC and FC curves for sample G2 in a field of 50 Oe. Upon increasing the Mn concentration, together with the emergence of metallic conductivity, differences between spontaneous magnetization ( $M_S$ ) and thermo-remnant magnetization (TRM) get reduced. This indicates that long-range global ferromagnetic order gradually replaces mesoscopic ferromagnetic order when hole localization diminishes.

### Interplay between localization and magnetism in (Ga,Mn)As at the MIT regime.

In Fig. 6.3, the solid lines and open circles represent the temperature dependent TRM and sheet resistance, respectively. The resistance in the  $G\Omega$  range of sample G1 (Fig. 6.3a) indicates a robust localization of carriers. The conductivity can be described as variable range hopping *via* a Coulomb gap with a characteristic energy of 3.4 meV in the whole temperature range, as shown in Fig. 6.4. There is no detectable remnant

magnetization in this sample, indicating that the FM coupling does not develop for such a low  $x$  value above 2 K – the sample is in a paramagnetic state.

However, clear indications of FM coupling are seen for the remaining samples with  $x \geq 0.66\%$ . Namely, all these samples show the existence of TRM, whose thermal properties change significantly with  $x$ . In particular, upon increasing  $x$  the TRM vanishes at progressively higher temperatures. Furthermore, the TRM curvature changes from a convex for sample G2 with  $x = 0.66\%$ , through a mixed case for sample G3, to a concave one for larger  $x$ . Remarkably, hand in hand with these changes a spontaneous magnetization  $M_S$  becomes visible when the sample is cooled back at the same zero-field conditions under which the TRM was measured. This ferromagnetic response  $M_S$ : (i) appears on cooling at exactly the same temperature  $T_C$  at which the TRM shows up, and (ii)  $M_S$  follows the TRM only when the TRM's curvature is concave, otherwise the  $M_S$  trails below the TRM. As detailed below, information encoded in TRM and  $M_S(T)$  measurements proves sufficient to assess the magnetic constitution of the studied layers.

Sample G2 with  $x = 0.66\%$  is the lowest- $x$  layer exhibiting a non-zero TRM. This is indicative that the FM coupling is present here, but the rapid increase of the resistivity at low temperatures, despite four orders of magnitude lower values than in sample G1, still points to a sizable localization that precludes a long-range (global) ordering mediated by itinerant holes. Indeed, this is the case – the FM coupling is maintained only over a nanometer-range distance.

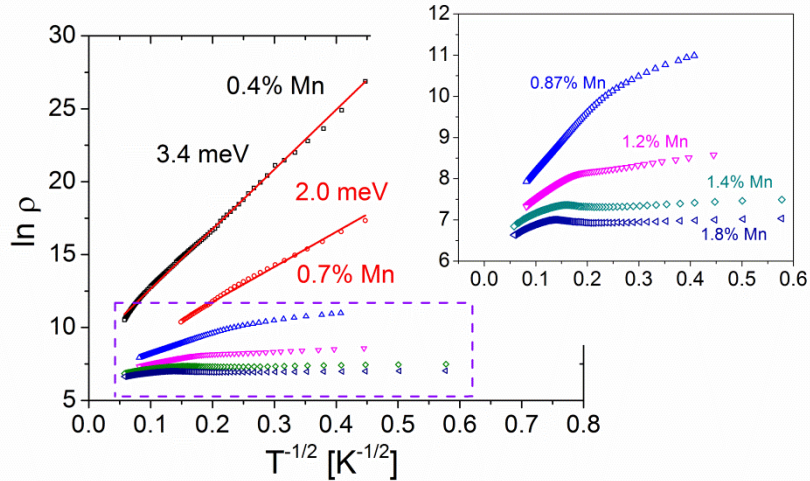


**Fig. 6.4** Temperature dependence of resistivity  $\rho$  in  $(\text{Ga,Mn})\text{As}$  in the absence of an external magnetic field. The results are shown as  $\ln(\rho)$  vs  $T^{-1/2}$ . In samples G1 and G2, the linear dependence dominates across the whole temperature range, supporting the crucial role of hopping mechanism in the electronic transport. However, in other samples with higher Mn concentrations, the conduction mechanism significantly changes, as magnified in the inset.

To substantiate the claim above we resort to low-temperature sample cycling in a weak field of 50 Oe in the well-established protocol of zero-field cooled (ZFC) and the field cooled (FC) manner. The results presented in the inset to Fig. 6.3b convince us of a granular (nonhomogeneous) magnetic state of this sample, as the magnetic behavior is typical for blocked SPM ensembles of magnetic particles. In particular, a maximum on the ZFC curve and a clear bifurcation between ZFC and FC data are both seen at nearly the same temperature, corresponding to the (mean) blocking temperature  $T_B$  of the ensemble. By using the standard formula for the dynamical blocking,  $KV = 25k_B T_B$ , where  $K$ , the anisotropy constant in (Ga,Mn)As, ranges between 5 000 and 50 000 erg/cm<sup>3</sup> [41],  $V$  is the volume of the magnetic particle,  $k_B$  is the Boltzmann constant, and the factor 25 is set by the experimental time scale – about 100 s, in the SQUID magnetometry. This condition implies that  $T_B \cong 5$  K corresponds to a sphere of a diameter between 8 to 20 nm, what indeed confirms a mesoscopic extent of FM coupling in this case. Importantly, the appearance of the granular magnetism does not result from nanometer sized Mn aggregates or other types of short scale Mn inhomogeneities, as their presence is excluded by the TEM analyses (see *e.g.* Fig. 6.2a). The presence of magnetic particles is assigned to the fact that according to the Anderson-Mott character of the MIT – occurring primarily due to localization of band carriers by scattering – the carriers' localization radius increases only gradually from the Bohr radius in the strong localization limit,  $p \rightarrow 0$ , towards infinity at the MIT,  $p \rightarrow p_c$  [14]. Thus, a magnetic nanoscale phase separation, driven by carrier density fluctuations, is present in the vicinity of the localization boundary. In such a case FM grains are embedded in the PM host background, as observed experimentally [13, 161]. At the same time, the presence of randomly oriented nano-sized magnetic grains gives rise to efficient spin-disorder scattering of carries. This enhances localization at  $B = 0$  and leads to a colossal negative magnetoresistance when a magnetic field is applied to polarize the nano-sized ferromagnetic component. Such a colossal negative magnetoresistance has been observed for sample G2 as shown in Fig. 6.5a and also in donor-compensated (Ga,Mn)As MBE films with higher Mn concentrations [55, 172].

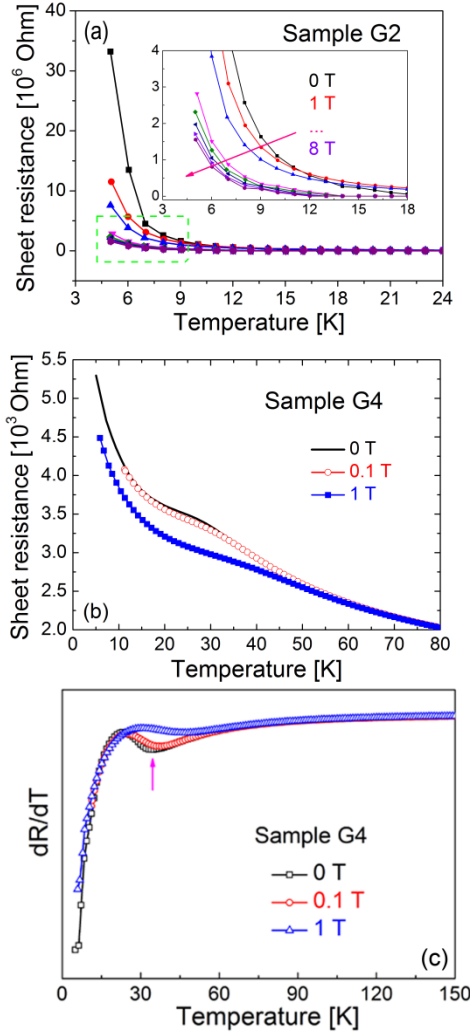


**Fig. 6.5 Temperature dependent magnetoresistance in two (Ga,Mn)As samples.** (a) In the superparamagnetic sample G2, the resistance at 5 K gets reduced by 95% in 8 T, and the effect results from the suppression of hole scattering by randomly orientated FM grains and orbital quantum localization effect. (b) (c) In the ferromagnetic sample G4, the critical spin-disorder scattering of itinerant holes by fluctuating Mn spins near  $T_C$ , disappears when the magnetic field is increased to 1T.

Due to the absence of a long-range magnetic coupling in sample G2, the concept of a Curie temperature as the temperature of the thermodynamic phase transition is not appropriate. However, from our measurements we can assess a maximum temperature up to which the magnetic particles survive,  $T_\sigma$ . From Fig. 6.3b we get  $T_\sigma \cong 7 \text{ K}$  where the TRM vanishes. Finally, we want to point out that  $M_S$  is zero for this sample in the whole studied temperature range. This is yet another strong indication of the mesoscopic scale of the magnetism in this case. On cooling without an external field the magnetic moments of the grains get blocked in random orientations yielding zero net magnetization, although at the remanence it yields a sizeable one.

Upon increasing the Mn concentration to 0.87%, the global ferromagnetism with a transition temperature  $T_C = 17 \text{ K}$  appears, as indicated in Fig. 6.3c. However, a clear

gap which opens between the TRM and  $M_S(T)$  below  $T_C$ , accompanied by a change of the TRM's curvature to a convex one, informs us about the presence of an additional magnetic component possessing similar, superparamagnetic, properties to that observed in sample G2. The value of the TRM –  $M_S$  bifurcation temperature, when accompanied by a change to the convex curvature of the TRM, is a practical assessment of  $T_\sigma$ .

In contrast, global ferromagnetism without any superparamagnetism is found in sample G4 with 1.2% Mn. This is proven by the overlap of curves corresponding to heating and cooling TRM measurements. In this sample a characteristic hump [55, 160] appears in the temperature dependent resistance near  $T_C = 30$  K. In DFSs, the hump comes from critical spin-disorder scattering of itinerant holes by fluctuating Mn spins near  $T_C$ . Such scattering can be suppressed by an external magnetic field (see Fig. 6.5b). This sample exhibits a clear increase of the resistivity upon lowering temperature, which points to its insulating character. In means that global FM signatures set in at lower  $x$  values, thus at lower hole concentrations than metallic behavior.

Both metallic behavior and global ferromagnetism are observed in sample G5 with  $x = 1.4\%$ . A weak resistance increase at low temperature is related to quantum corrections to conductance on the metallic side of the MIT [160]. In this sample, the negative magnetoresistance at low temperatures  $T \ll T_C$  can also be well fitted within the quantum localization scenario as shown in Fig. 6.6 by Eq. 6.3 [173].

$$\frac{\Delta\rho(B)}{\rho(0)} \approx -\frac{\Delta\sigma}{\sigma} = -\frac{n_V e^2 C_0 \rho(B) (eB/\hbar)^{\frac{1}{2}}}{2\pi^2 \hbar} \quad 6.3$$

where  $C_0 \approx 0.605$ ,  $\rho$  is the resistivity,  $\sigma$  is the electrical conductivity,  $e$  is the elemental charge,  $\hbar$  is the reduced Planck constant, and the fitted  $n_V = 1.6$  indicating that almost three subbands contribute to the charge transport. The remarkable fitting curve to the experimental results describes the interaction between spin-polarized holes and uniform magnetism in the metallic (Ga,Mn)As sample.



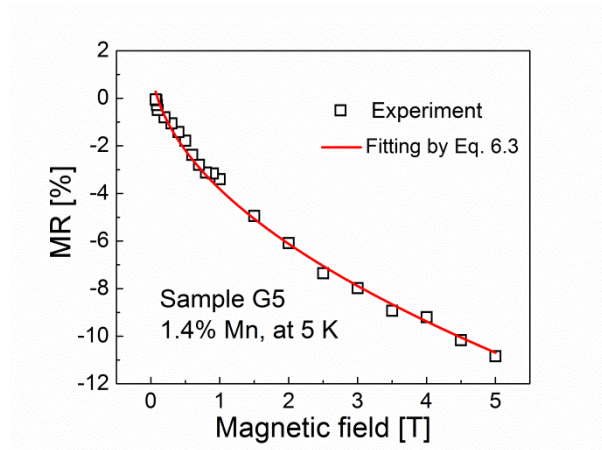


**Fig. 6.6 Quantum localization-induced negative magnetoresistance in metallic (Ga,Mn)As.** Negative magnetoresistance is observed at 5 K in sample G5 in the fields in which Mn spins are saturated (points). A remarkably good fitting (solid line) suggests that single-carrier orbital weak-localization magnetoresistance dominates at low temperatures [173].

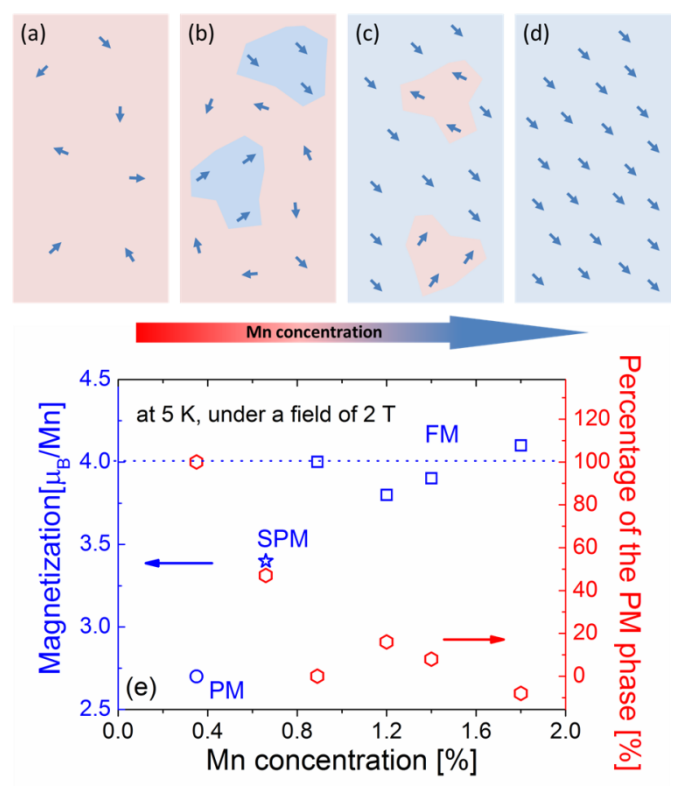


**Fig. 6.7 Descriptions of the transition from the paramagnetic to ferromagnetic phases in (Ga,Mn)As.** (a-d) A schematic diagram of the evolution of magnetic order in (Ga,Mn)As with increasing Mn concentration. (e) Mn concentration dependent magnetization in the paramagnetic (circle), superparamagnetic (star), and ferromagnetic (squares) samples measured under a field of 2 T at 5 K.

The evolution of magnetism with  $x$ , as determined for our samples, is illustrated

schematically in Figs. 6.7a-d. The normalized magnetization per Mn atom is calculated from the magnetization divided by the integrated number of all Mn atoms in the layer. The magnetization has been measured at 5 K and 2 T to saturate both the SPM and FM components. The results are displayed in Fig. 6.7e. They allow us to obtain information on the degree of hole localization and on the relative participation of the ferromagnetic component.

Because of a low Mn and hole concentration  $p = 8.8 \times 10^{19} \text{ cm}^{-3}$  only paramagnetism is observed in sample G1 for which the normalized magnetization is determined to be  $M = 2.8 \mu_B/\text{Mn}$ . This value allows us to find out whether the holes are in the strongly or weakly localized regime in this sample. In the former case, the holes are localized on parent Mn acceptors and the magnetic moment per Mn atom can be calculated from the Brillouin function,

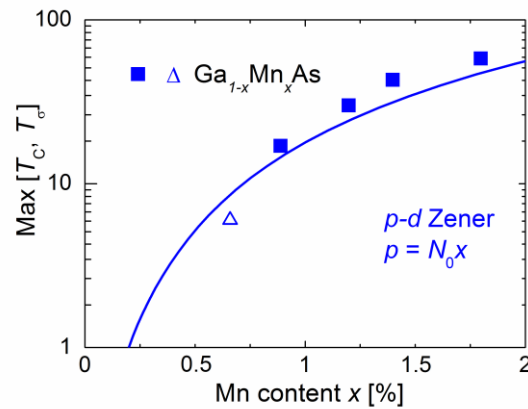
$$M = Jg\mu_B \left[ \frac{2J+1}{2J} \coth\left(\frac{2J+1}{2J}x\right) - \frac{1}{2J} \coth\left(\frac{1}{2J}x\right) \right], \quad 6.4$$

$$x = \frac{Jg\mu_B H}{k_B T}. \quad 6.5$$

where  $J = 1$  and  $g = 2.77$  [174]. This formula leads to  $M = 1.6 \mu_B/\text{Mn}$  at 5 K in 20 kOe, which implies that the model of strong localization is not applicable for the Mn concentration in question. On the other hand assuming  $J = 5/2$  and  $g = 2.0$  the  $M$  is calculated as  $2.7 \mu_B$ , and it is close to the measured value of  $2.8 \mu_B/\text{Mn}$  in sample G1 by the SQUID magnetometry. This is consistent with the fact that the degree of the hole spin polarization is small, as the Fermi level is about 80 meV above the valence band whereas the valence band spin splitting is below 12 meV [175].

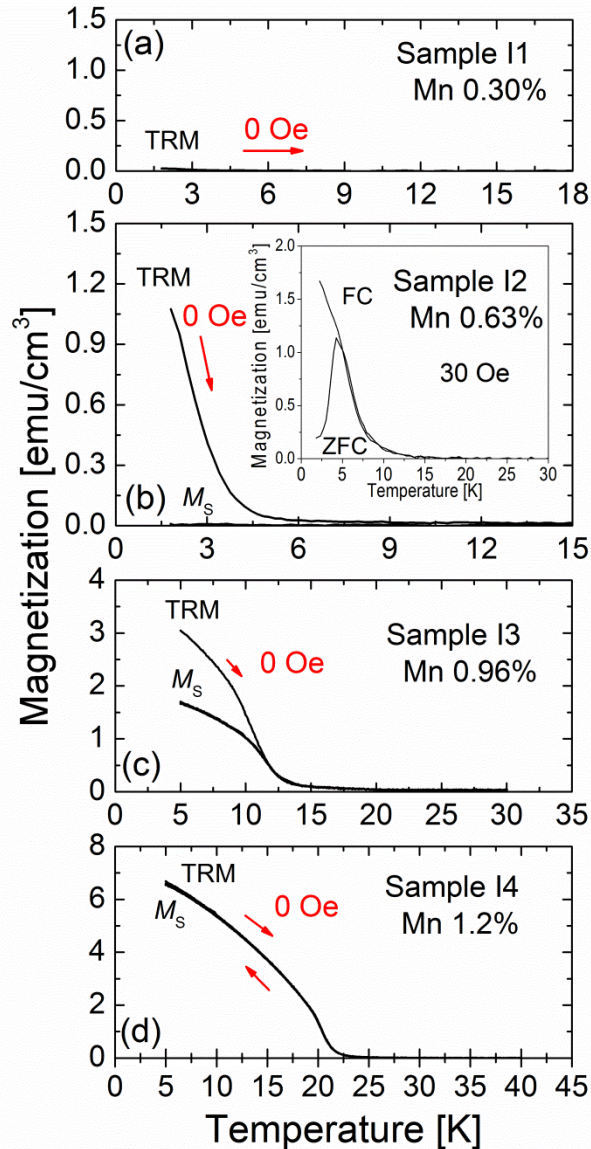
In the SPM sample G2,  $M = 3.4 \mu_B/\text{Mn}$  is observed, indicating that not all Mn spins contribute to the detectable magnetic moment as shown in Fig. 6.7b. Such value can be used for quantitatively evaluating the electronic phase separation between the ferromagnetic and paramagnetic phases in this (Ga,Mn)As system. For sample G2,  $M = 3.4 \mu_B/\text{Mn}$  implies a mixture of the nano-sized hole-rich ferromagnetic phase and the paramagnetic matrix with only very few holes. Therefore, the values of 4 and  $2.8 \mu_B/\text{Mn}$  in the ferromagnetic and paramagnetic regions, respectively, can be used to quantitatively calculate the composition of each phase according to  $4\mu_B(1-y) + 2.8\mu_B y = M_{\text{Mn}}$ , where  $y$  is the percentage of the paramagnetic phase, i.e., of the component without ferromagnetic coupling, and  $M$  is the measured value in Fig. 6e. As the Mn density increases, the percentage of paramagnetic Mn is gradually decreasing: From 100% in sample G1, through 47% in sample G2, finally gets saturated at around 0% in samples G3-G6. The results correspond to the electronic picture given in Figs. 6.3 and 6.7, i.e. the inhomogeneity of the ferromagnetism in the sample in the MIT regime directly comes from the electronic phase separation. Note that, since the implanted Mn atoms are not distributed in a rectangular fashion, but

exhibit a Gaussian shape, a tail with lower Mn concentrations always exists in all samples. However, only a small part of the superparamagnetic phase is seen through TRM measurements in the ferromagnetic samples G4 and G5 (see in Figs. 6.3d and e), indicating the tail with low Mn concentration is negligible.



**Fig. 6.8** The dependence of the  $T_C(T_\sigma)$  vs Mn content matches the Zener model prediction in both SPM and FM (Ga,Mn)As samples. Curie temperatures  $T_C$  (full points) and SP temperatures  $T_\sigma$  (empty triangle) in  $\text{Ga}_{1-x}\text{Mn}_x\text{As}$ . The solid line shows the prediction by the  $p$ - $d$  Zener model for  $\text{Ga}_{1-x}\text{Mn}_x\text{As}$  assuming the absence of compensating donors.

It is interesting to compare the experimental values of  $T_C$  and  $T_\sigma$  to the expectations of the  $p$ - $d$  Zener model. As shown in Fig. 6.8, there is good agreement between the measured and computed values for both insulating and metallic samples. This finding substantiates the applicability of the  $p$ - $d$  Zener model for the description of ferromagnetism mediated by itinerant holes as well as by weakly localized holes.



**Fig. 6.9** The transition from the PM, via SPM, to FM phase in (In,Mn)As samples at the MIT regime. Temperature dependent thermo-remnant magnetization of (In,Mn)As samples of (a) I1, (b) I2, (c) I3, and I4. The inset to (b) shows the temperature dependent magnetization under a field of 30 Oe after field cooling (FC) and zero field cooling (ZFC) for sample I2.

**Magnetic properties of (In,Mn)As at the MIT regime.** The versatility of ion implantation allows us to compare (Ga,Mn)As with (In,Mn)As. Previous studies of (In,Mn)As films obtained by MBE with relatively large Mn concentrations [55, 176] show lower  $T_C$  compared to (Ga,Mn)As, in agreement with theoretical expectations [14, 175]. According to our results presented in Fig. 6.9, an evolution from the paramagnetic phase to the global ferromagnetic state which takes place in (Ga,Mn)As with increasing  $x$  is also observed in (In,Mn)As samples obtained by ion implantation and PLM.

Only paramagnetic behavior is observed in sample I1 with  $x = 0.30\%$  like in the

(Ga,Mn)As sample with  $x = 0.35\%$ . In sample I2, both TRM and a bifurcation between ZFC and FC co-imply the SPM character, as in the case of sample G2. When the Mn concentration reaches 0.96%, the TRM measurement points to the coexistence of superparamagnetism and long-range ferromagnetism, which is similar to the case of the (Ga,Mn)As sample with  $x = 0.87\%$ . Upon further increase of  $x$  to 1.2%, global ferromagnetism dominates, similarly to (Ga,Mn)As with the same  $x$ .

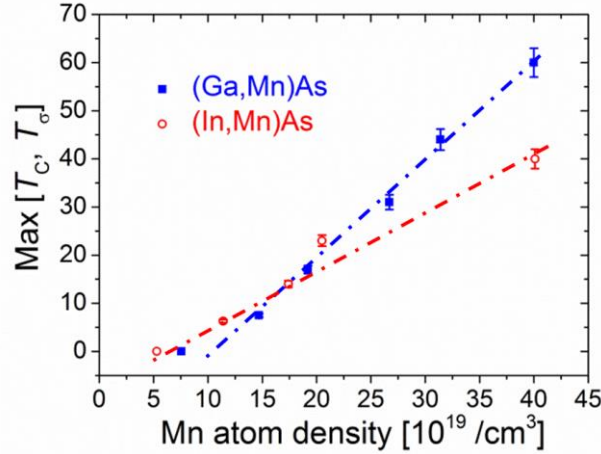


**Fig. 6.10 Influence of the  $p$ - $d$  coupling strength on magnetic properties of (Ga,Mn)As and (In,Mn)As.** The dependence of the the Curie and superparamagnetic temperature ( $T_C$  and  $T_\sigma$ , respectively) on the Mn atom density for (Ga,Mn)As and (In,Mn)As. The dash and dot lines are linear guides for eye for (Ga,Mn)As and (In,Mn)As, respectively.

**The  $p$ - $d$  coupling contribution to the magnetic behaviour at the MIT regime.** The Curie and SPM temperatures,  $T_C$  and  $T_\sigma$ , respectively of a series of (Ga,Mn)As and (In,Mn)As samples with sequentially increasing Mn densities are shown in Fig. 6.10. Interestingly, an approximately linear dependence of Max [ $T_C, T_\sigma$ ] vs. the Mn concentration is found for both materials, however, with differing slopes. In the regime of  $N \leq 1.9 \times 10^{20} \text{ cm}^{-3}$ , the (Ga,Mn)As samples exhibit a lower  $T_C$  or  $T_\sigma$  at given Mn concentrations, i.e., weaker ferromagnetism compared to (In,Mn)As, while in the regime of  $N > 1.9 \times 10^{20} \text{ cm}^{-3}$ , higher Curie temperatures are observed in (Ga,Mn)As. This remarkable observation substantiates experimentally the dual role of  $p$ - $d$  exchange coupling in DFSs, as discussed theoretically previously [177]. Deeper in the metallic phase, a larger  $p$ - $d$  interaction makes the hole-mediated ferromagnetism stronger, so that  $T_C$  in (Ga,Mn)As is higher than in (In,Mn)As, as observed previously [55, 112, 176]. However, in addition to controlling ferromagnetic coupling, a larger  $p$ - $d$  hybridization shifts the MIT to higher hole concentrations, the effect being stronger in (Ga,Mn)As than in (In,Mn)As in which the bond length is longer. The enhanced hole localization makes ferromagnetic features weaker in (Ga,Mn)As compared to (In,Mn)As in the limit of low hole densities.

## 6.4 Discussion

Through combining systematic studies of electrical and magnetic properties, we have presented experimental evidences supporting the heterogeneous model of electronic states at the localization boundary in (Ga,Mn)As and (In,Mn)As without compensating donors. A transition from an insulating (hopping) to a metallic-like conductance is observed, which is accompanied by a gradual build-up of long-range magnetic coupling, as well as by an increase of the Curie temperature. The  $p$ - $d$  Zener model prediction is consistent with the measured  $T_C$  values in metallic samples as well as with the magnitudes of  $T_C$  and  $T_\sigma$  on the insulator side of the transition, where the ferromagnetic coupling is mediated by weakly localized holes. Furthermore, in the low Mn concentration doped samples, the interplay between localization and magnetism results in higher  $T_C$  in (In,Mn)As compared to (Ga,Mn)As in which the stronger  $p$ - $d$  coupling enhances localization.



## Chapter 7

# Summary and outlook

### 7.1 Summary

In this thesis, the Mn doped III-V dilute ferromagnetic semiconductors (DFSs), including (Ga,Mn)P, (In,Mn)As, as well as (Ga,Mn)As, were successfully prepared by ion implantation and pulsed laser melting. Moreover, an investigation on their structural, magnetic, and electrical properties was systematically performed to establish the relation between carrier localization and magnetism inside the DFSs layer.

The highly epitaxial structure of DFS layer on III-V semiconductor substrates driven by pulsed laser induced liquid epitaxial regrowth was proven by high resolution TEM, and Rutherford backscattering spectrometry: Neither Mn-rich clusters nor interstitial Mn atoms are detected in the material.

In Raman spectra, an additional vibration mode due to the fact that the carrier plasma couples with the LO phonon through macroscopic electric fields proves the *p*-type conductivity in Mn-doped DFSs. Moreover, as in (Ga,Mn)As, the anomalous Hall effect in (Ga,Mn)P sample directly gives the evidence of spin splitting phenomena. The appearance of the strong uniaxial magnetic anisotropy in all three different materials excludes the possibility of detectable second-phase induced ferromagnetism. Interestingly, this uniaxial magnetic anisotropy can be modified by different laser energies during PLM by manipulating the generation of magnetic domains.

In addition to (Ga,Mn)P, (In,Mn)As with a perpendicular magnetic anisotropy and a high Curie temperature up to 77 K is also obtained from ion implantation. The XMCD results also confirm the existence of a perpendicular magnetic anisotropy in (In,Mn)As epilayers. To our knowledge, this is the highest  $T_C$  recorded for (In,Mn)As with perpendicular magnetic anisotropy. The good crystalline quality of these epilayers is confirmed by the Pendellösung fringes around the InAs (004) peak in XRD patterns and the square-like hysteresis loops along the magnetic easy axis. The



inner strain induced by the Mn ions substituted in the (In,Mn)As epilayers plays a critical role in the appearance of a perpendicular magnetic anisotropy in this system.

It is worth noting that the interplay between localization and magnetism, particularly in the regime of the insulator to metal transition (IMT), is investigated through the comparison between (In,Mn)As, (Ga,Mn)As, and (Ga,Mn)P. In both (In,Mn)As and (Ga,Mn)As, the long-range global ferromagnetic coupling is gradually built up accompanied by the transition from insulating to metallic phase as the Mn concentration increases. However, the ferromagnetic coupling appears at lower Mn concentration in (In,Mn)As than in (Ga,Mn)As, resulting from the different  $p-d$  coupling strength between Mn local spins and holes. In (Ga,Mn)P, a much stronger  $p-d$  coupling drives the Mn impurity in a much deeper position in the band gap (400 meV above the top of valence band), leading to the insulating electrical behavior. In this case, the super-exchange interaction is used to explain the detected long-range ferromagnetic signal.

## 7.2 Outlook

### (1) Tuning magnetic properties through modifying $p-d$ coupling strength

The interplay between magnetism and localization is investigated in this thesis particularly in the insulator-metal transition regime in different III-Mn-V dilute ferromagnetic semiconductors. It is strongly influenced by the  $p-d$  coupling between carrier and Mn local spins. The finished work was concentrated on varying the Mn concentration in (In,Mn)As and (Ga,Mn)As to obtain different localization degree. An interesting attempt would be a fine manipulation of the  $p-d$  coupling strength, thus to modify the electric and magnetic properties including magnetization and Curie temperature.

As predicted, when Ga atoms gradually substitute the In sites in (In,Mn)As, the  $p-d$  coupling strength will be enhanced by the reduction of lattice parameter. As a consequence, both magnetization and Curie temperature increase, meanwhile, the sample becomes more insulating resulting from more localized nature of holes.

### (2) Modifying magnetic polaron/electronic phase separation in (Ga,Mn)P and (Ga,Mn)As by bias gating

According to our recent cooperative work with Prof. Jens Müller in University of Frankfurt am Main, two different mechanisms for explaining the hole-mediated ferromagnetism are re-proven in two different DFSSs, (Ga,Mn)P and (Ga,Mn)As. By

firstly employing fluctuation spectroscopy, obvious noise signals are seen in both (Ga,Mn)P and insulating (Ga,Mn)As samples at the Curie temperature, indicating the contribution from the disorder which results from the competition between Mn-Mn long-range ferromagnetic coupling and thermal fluctuations. Interestingly, two totally different shapes of the noise peaks measured for (Ga,Mn)P and (Ga,Mn)As reveal the distinct mechanisms in two DFSs. A sharp peak in the noise spectrum of (Ga,Mn)P indicates the formation of magnetic polarons, however, a platform-like noise peak in (Ga,Mn)As can be explained by the electronic phase separation as shown in Fig. 7.1. It is worth noting that no clear noise peak is observed in metallic (Ga,Mn)As, excluding the existence of either magnetic polaron or electronic phase separation.

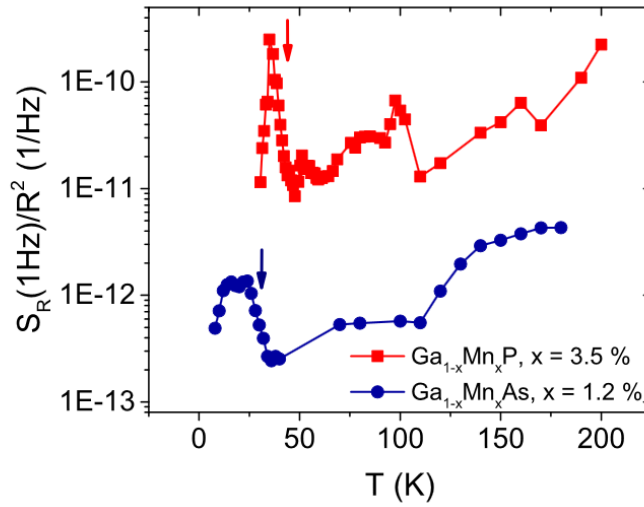


Fig. 7.1 Temperature-dependent noise magnitude of a  $\text{Ga}_{1-x}\text{Mn}_x\text{As}$  sample with Mn concentration of 1.2% and a  $\text{Ga}_{1-x}\text{Mn}_x\text{P}$  sample ( $x = 3.5\%$ ), both showing an increase of noise just below  $T_C$ . The Curie temperatures are marked with arrows (unpublished results).

Due to the fact that the noise peak only shows up in insulating DFS samples, we believe that the noise behavior in fluctuation spectra will be strongly influenced when the DFS sample goes through the insulator-metal transition.

We aim at investigations on the noise spectrum for (Ga,Mn)As and (Ga,Mn)P DFSs which is tuned by bias voltage gating in the regime of insulator-metal transition. The strategy is:

- (1) (Ga,Mn)As and (Ga,Mn)P with different Mn concentrations are prepared by LT-MBE / ion implantation.
- (2) The sample with Hall bar geometry is made by wet etching method.
- (3) A  $\text{HfO}_2$  layer will be prepared by atomic layer deposition, acting as the dielectric layer for a MOS structure to realize the electric gating.
- (4) The noise related behaviors will be measured by fluctuation spectroscopy when the sample is tuned by bias voltage gating.

The employment of this new technique of fluctuation spectroscopy will be definitely helpful to understand the physics in DFSs with different  $p$ - $d$  coupling strengths, particularly in the regime of insulator-metal transition.

# Bibliography

1. Kasuya, T.; Yanase, A., Anomalous Transport Phenomena in Eu-Chalcogenide Alloys. *Rev. Mod. Phys.* 1968, **40**, 684.
2. Dietl, T.; Ohno, H., Dilute ferromagnetic semiconductors: Physics and spintronic structures. *Rev. Mod. Phys.* 2014, **86**, 187.
3. Ohno, H., Making nonmagnetic semiconductors ferromagnetic. *Science* 1998, 281, 951-956.
4. Jungwirth, T.; Niu, Q.; MacDonald, A. H., Anomalous Hall effect in ferromagnetic semiconductors. *Phys. Rev. Lett.* 2002, **88**, 207208.
5. Onoda, M.; Nagaosa, N., Topological nature of anomalous Hall effect in ferromagnets. *J. Phys. Soc. Jpn.* 2002, **71**, 19-22.
6. Ciorga, M.; Einwanger, A.; Sadowski, J.; Wegscheider, W.; Weiss, D., Tunneling anisotropic magnetoresistance effect in a p(+)-(Ga,Mn)As/n(+)-GaAs Esaki diode. *Phys. Status Solidi A* 2007, **204**, 186-190.
7. Sankowski, P.; Kacman, P.; Majewski, J. A.; Dietl, T., Spin-dependent tunneling in modulated structures of (Ga,Mn)As. *Phys. Rev. B* 2007, **75**, 045306.
8. Elsen, M.; Jaffres, H.; Mattana, R.; Thevenard, L.; Lemaitre, A.; George, J. M., Spin-polarized tunneling as a probe of the electronic properties of Ga<sub>1-x</sub>Mn<sub>x</sub>As heterostructures. *Phys. Rev. B* 2007, **76**, 144415.
9. Brey, L.; Tejedor, C.; Fernandez-Rossier, J., Tunnel magnetoresistance in GaMnAs: Going beyond julliere formula. *Appl. Phys. Lett.* 2004, **85**, 1996-1998.
10. Sinova, J.; Jungwirth, T.; Liu, X.; Sasaki, Y.; Furdyna, J. K.; Atkinson, W. A.; MacDonald, A. H., Magnetization relaxation in (Ga,Mn)As ferromagnetic semiconductors. *Phys. Rev. B* 2004, **69**, 085209.
11. Chiba, D.; Sato, Y.; Kita, T.; Matsukura, F.; Ohno, H., Current-driven magnetization reversal in a ferromagnetic semiconductor (Ga,Mn)As/GaAs/(Ga,Mn)As tunnel junction. *Phys. Rev. Lett.* 2004, **93**, 216602.
12. Chiba, D.; Sawicki, M.; Nishitani, Y.; Nakatani, Y.; Matsukura, F.; Ohno, H., Magnetization vector manipulation by electric fields. *Nature* 2008, **455**, 515-518.
13. Sawicki, M.; Chiba, D.; Korbecka, A.; Nishitani, Y.; Majewski, J. A.; Matsukura, F.; Dietl, T.; Ohno, H., Experimental probing of the interplay between ferromagnetism and localization in (Ga,Mn)As. *Nat. Phys.* 2010, **6**, 22-25.
14. Dietl, T.; Ohno, H.; Matsukura, F.; Cibert, J.; Ferrand, D., Zener model description of ferromagnetism in zinc-blende magnetic semiconductors. *Science* 2000, **287**, 1019-1022.
15. Ferrand, D.; Bourgognon, C.; Cibert, J.; Wasiela, A.; Tatarenko, S.; d'Aubigne, Y. M.; Bonanni, A.; Stifter, D.; Sitter, H.; van Khoi, L.; Kolesnik, S.; Jaroszynski, J.; Sawicki, M.; Andrearczyk, T.; Dietl, T., Indication of ferromagnetic ordering in p-Zn<sub>1-x</sub>Mn<sub>x</sub>Te. *Physica B* 2000, **284**, 1177-1178.
16. Hai, P. N.; Anh, L. D.; Mohan, S.; Tamegai, T.; Kodzuka, M.; Ohkubo, T.; Hono, K.; Tanaka, M., Growth and characterization of n-type electron-induced ferromagnetic semiconductor (In,Fe)As. *Appl. Phys. Lett.* 2012, **101**, 182403.
17. Hai, P. N.; Anh, L. D.; Tanaka, M., Electron effective mass in n-type electron-induced ferromagnetic semiconductor (In,Fe)As: Evidence of conduction band transport. *Appl. Phys. Lett.* 2012, **101**, 252410.
18. Kobayashi, M.; Anh, L. D.; Hai, P. N.; Takeda, Y.; Sakamoto, S.; Kadono, T.; Okane, T.; Saitoh, Y.;

- Yamagami, H.; Harada, Y.; Oshima, M.; Tanaka, M.; Fujimori, A., Spin and orbital magnetic moments of Fe in the n-type ferromagnetic semiconductor (In,Fe)As. *Appl. Phys. Lett.* 2014, **105**, 032403.
19. Sasaki, D.; Anh, L. D.; Hai, P. N.; Tanaka, M., Interplay between strain, quantum confinement, and ferromagnetism in strained ferromagnetic semiconductor (In,Fe)As thin films. *Appl. Phys. Lett.* 2014, **104**, 142406.
20. Anh, L. D.; Hai, P. N.; Kasahara, Y.; Iwasa, Y.; Tanaka, M., Modulation of ferromagnetism in (In,Fe)As quantum wells via electrically controlled deformation of the electron wave functions. *Phys. Rev. B* 2015, **92**, 161201.
21. Bonanni, A.; Dietl, T., A story of high-temperature ferromagnetism in semiconductors. *Chem. Soc. Rev.* 2010, **39**, 528-539.
22. Dietl, T.; Ohno, H.; Matsukura, F., Hole-mediated ferromagnetism in tetrahedrally coordinated semiconductors. *Phys. Rev. B* 2001, **63**, 195205.
23. Sawicki, M.; Matsukura, F.; Idziaszek, A.; Dietl, T.; Schott, G. M.; Ruester, C.; Gould, C.; Karczewski, G.; Schmidt, G.; Molenkamp, L. W., Temperature dependent magnetic anisotropy in (Ga,Mn)As layers. *Phys. Rev. B* 2004, **70**, 245325.
24. Thevenard, L.; Largeau, L.; Mauguin, O.; Lemaitre, A.; Theys, B., Tuning the ferromagnetic properties of hydrogenated GaMnAs. *Appl. Phys. Lett.* 2005, **87**, 182506.
25. Yahyaoui, M.; Testelin, C.; Gourdon, C.; Boujdaria, K., The influence of the epitaxial strain on the magnetic anisotropy in ferromagnetic (Ga,Mn)(As,P)/GaAs thin films. *J. Appl. Phys.* 2012, **111**, 033902.
26. Lemaitre, A.; Miard, A.; Travers, L.; Mauguin, O.; Largeau, L.; Gourdon, C.; Jeudy, V.; Tran, M.; George, J. M., Strain control of the magnetic anisotropy in (Ga,Mn)(As,P) ferromagnetic semiconductor layers. *Appl. Phys. Lett.* 2008, **93**, 021123.
27. Casiraghi, A.; Rushforth, A. W.; Wang, M.; Farley, N. R. S.; Wadley, P.; Hall, J. L.; Staddon, C. R.; Edmonds, K. W.; Campion, R. P.; Foxon, C. T.; Gallagher, B. L., Tuning perpendicular magnetic anisotropy in (Ga,Mn)(As,P) by thermal annealing. *Appl. Phys. Lett.* 2010, **97**, 122504.
28. Stefanowicz, S.; Kunert, G.; Simserides, C.; Majewski, J. A.; Stefanowicz, W.; Kruse, C.; Figge, S.; Li, T.; Jakiela, R.; Trohidou, K. N.; Bonanni, A.; Hommel, D.; Sawicki, M.; Dietl, T., Phase diagram and critical behavior of the random ferromagnet  $Ga_{1-x}Mn_xN$ . *Phys. Rev. B* 2013, **88**, 081201.
29. Twardowski, A.; Swagten, H. J. M.; Dejonge, W. J. M.; Demianiuk, M., Magnetic-Behavior of the Diluted Magnetic Semiconductor  $Zn_{1-x}Mn_xSe$ . *Phys. Rev. B* 1987, **36**, 7013-7023.
30. Karczewski, G.; Sawicki, M.; Ivanov, V.; Ruester, C.; Grabecki, G.; Matsukura, F.; Molenkamp, L. W.; Dietl, T., Ferromagnetism in (Zn,Cr)Se layers grown by molecular beam epitaxy. *J. Supercond.* 2003, **16**, 55-58.
31. Saito, H.; Zayets, V.; Yamagata, S.; Ando, K., Room-temperature ferromagnetism in a II-VI diluted magnetic semiconductor  $Zn_{1-x}Cr_xTe$ . *Phys. Rev. Lett.* 2003, **90**, 207202.
32. Sawicki, M.; Devillers, T.; Galeski, S.; Simserides, C.; Dobkowska, S.; Faina, B.; Grois, A.; Navarro-Quezada, A.; Trohidou, K. N.; Majewski, J. A.; Dietl, T.; Bonanni, A., Origin of low-temperature magnetic ordering in  $Ga_{1-x}Mn_xN$ . *Phys. Rev. B* 2012, **85**, 205204.
33. Dietl, T.; Matsukura, F.; Ohno, H., Ferromagnetism of magnetic semiconductors: Zhang-Rice limit. *Phys. Rev. B* 2002, **66**, 033203.
34. Sato, K.; Dederics, P. H.; Katayama-Yoshida, H., Curie temperatures of III-V diluted magnetic semiconductors calculated from first principles. *Europhys. Lett.* 2003, **61**, 403-408.
35. Berciu, M.; Bhatt, R. N., Effects of disorder on ferromagnetism in diluted magnetic

- semiconductors. *Phys. Rev. Lett.* 2001, **87**, 107203.
36. Mahadevan, P.; Zunger, A., Trends in ferromagnetism, hole localization, and acceptor level depth for Mn substitution in GaN, GaP, GaAs, and GaSb. *Appl. Phys. Lett.* 2004, **85**, 2860-2862.
37. Erwin, S. C.; Petukhov, A. G., Self-compensation in manganese-doped ferromagnetic semiconductors. *Phys. Rev. Lett.* 2002, **89**, 227201.
38. Alberi, K.; Yu, K. M.; Stone, P. R.; Dubon, O. D.; Walukiewicz, W.; Wojtowicz, T.; Liu, X.; Furdyna, J. K., Formation of Mn-derived impurity band in III-Mn-V alloys by valence band anticrossing. *Phys. Rev. B* 2008, **78**, 075201.
39. Dobrowolska, M.; Tivakornsasithorn, K.; Liu, X.; Furdyna, J. K.; Berciu, M.; Yu, K. M.; Walukiewicz, W., Controlling the Curie temperature in (Ga,Mn)As through location of the Fermi level within the impurity band. *Nat. Mater.* 2012, **11**, 444-449.
40. Jungwirth, T.; Sinova, J.; MacDonald, A. H.; Gallagher, B. L.; Novak, V.; Edmonds, K. W.; Rushforth, A. W.; Champion, R. P.; Foxon, C. T.; Eaves, L.; Olejnik, E.; Masek, J.; Yang, S. R. E.; Wunderlich, J.; Gould, C.; Molenkamp, L. W.; Dietl, T.; Ohno, H., Character of states near the Fermi level in (Ga,Mn)As: Impurity to valence band crossover. *Phys. Rev. B* 2007, **76**, 125206.
41. Sawicki, M., Magnetic properties of (Ga,Mn)As. *J. Magn. Magn. Mater.* 2006, **300**, 1-6.
42. Neumaier, D.; Turek, M.; Wurstbauer, U.; Vogl, A.; Utz, M.; Wegscheider, W.; Weiss, D., All-Electrical Measurement of the Density of States in (Ga,Mn)As. *Phys. Rev. Lett.* 2009, **103**, 087203.
43. Zhou, S. Q.; Li, L.; Yuan, Y.; Rushforth, A. W.; Chen, L.; Wang, Y. T.; Bottger, R.; Heller, R.; Zhao, J. H.; Edmonds, K. W.; Champion, R. P.; Gallagher, B. L.; Timm, C.; Helm, M., Precise tuning of the Curie temperature of (Ga, Mn)As-based magnetic semiconductors by hole compensation: Support for valence-band ferromagnetism. *Phys. Rev. B* 2016, **94**, 075205.
44. Edmonds, K. W.; Gallagher, B. L.; Wang, M.; Rushforth, A. W.; Makarovsky, O.; Patane, A.; Champion, R. P.; Foxon, C. T.; Novak, V.; Jungwirth, T., Correspondence on “Controlling the Curie temperature in (Ga,Mn)As through localization of the Fermi level within the impurity band” by M. Dobrowolska et al. *arXiv:1211.3860*.
45. Gray, A. X.; Minar, J.; Ueda, S.; Stone, P. R.; Yamashita, Y.; Fujii, J.; Braun, J.; Plucinski, L.; Schneider, C. M.; Panaccione, G.; Ebert, H.; Dubon, O. D.; Kobayashi, K.; Fadley, C. S., Bulk electronic structure of the dilute magnetic semiconductor  $\text{Ga}_{1-x}\text{Mn}_x\text{As}$  through hard X-ray angle-resolved photoemission. *Nat. Mater.* 2012, **11**, 957-962.
46. Wang, M.; Marshall, R. A.; Edmonds, K. W.; Rushforth, A. W.; Champion, R. P.; Gallagher, B. L., Determining Curie temperatures in dilute ferromagnetic semiconductors: High Curie temperature (Ga,Mn)As. *Appl. Phys. Lett.* 2014, **104**, 132406.
47. Potashnik, S. J.; Ku, K. C.; Mahendiran, R.; Chun, S. H.; Wang, R. F.; Samarth, N.; Schiffer, P., Saturated ferromagnetism and magnetization deficit in optimally annealed  $\text{Ga}_{1-x}\text{Mn}_x\text{As}$  epilayers. *Phys. Rev. B* 2002, **66**, 012408.
48. Yu, K. M.; Walukiewicz, W.; Wojtowicz, T.; Lim, W. L.; Liu, X.; Bindley, U.; Dobrowolska, M.; Furdyna, J. K., Curie temperature limit in ferromagnetic  $\text{Ga}_{1-x}\text{Mn}_x\text{As}$ . *Phys. Rev. B* 2003, **68**, 041308(R).
49. Chen, L.; Matsukura, F.; Ohno, H., Electric-Field Modulation of Damping Constant in a Ferromagnetic Semiconductor (Ga,Mn)As. *Phys. Rev. Lett.* 2015, **115**, 057204.
50. Nemeč, P.; Rozkotová, E.; Tesarova, N.; Trojanek, F.; De Ranieri, E.; Olejnik, K.; Zemen, J.; Novak, V.; Cukr, M.; Maly, P.; Jungwirth, T., Experimental observation of the optical spin transfer torque. *Nat. Phys.* 2012, **8**, 411-415.

51. Sinova, J.; Jungwirth, T.; Liu, X.; Sasaki, Y.; Furdyna, J. K.; Atkinson, W. A.; MacDonald, A. H., Magnetization relaxation in (Ga,Mn)As ferromagnetic semiconductors. *Phys. Rev. B* 2004, **69**, 085209.
52. Yamanouchi, M.; Chiba, D.; Matsukura, F.; Dietl, T.; Ohno, H., Velocity of domain-wall motion induced by electrical current in the ferromagnetic semiconductor (Ga,Mn)As. *Phys. Rev. Lett.* 2006, **96**, 096601.
53. Ohno, H.; Chiba, D.; Matsukura, F.; Omiya, T.; Abe, E.; Dietl, T.; Ohno, Y.; Ohtani, K., Electric-field control of ferromagnetism. *Nature* 2000, **408**, 944-946.
54. Zhou, S. Q.; Wang, Y. T.; Jiang, Z. N.; Weschke, E.; Helm, M., Ferromagnetic InMnAs on InAs Prepared by Ion Implantation and Pulsed Laser Annealing. *Appl. Phys. Express* 2012, **5**, 093007.
55. Ohno, H.; Munekata, H.; Penney, T.; Vonmolnar, S.; Chang, L. L., Magnetotransport Properties of p-Type (In,Mn)As Diluted Magnetic III-V Semiconductors. *Phys. Rev. Lett.* 1992, **68**, 2664-2667.
56. Schallenberg, T.; Munekata, H., Preparation of ferromagnetic (In,Mn)As with a high Curie temperature of 90 K. *Appl. Phys. Lett.* 2006, **89**, 042507.
57. Yuan, Y.; Wang, Y.; Gao, K.; Khalid, M.; Wu, C.; Zhang, W.; Munnik, F.; Weschke, E.; Baehtz, C.; Skorupa, W.; Helm, M.; Zhou, S., High Curie temperature and perpendicular magnetic anisotropy in homoepitaxial InMnAs films. *J. Phys. D: Appl. Phys.* 2015, **48**, 235002.
58. Novak, J.; Soltys, J.; Elias, P.; Hasenohrl, S.; Vavra, I., Study of the growth and structural properties of InMnAs dots grown on high-index surfaces by MOVPE. *Mater. Sci. Semicon. Proc.* 2010, **13**, 167-172.
59. Scarpulla, M. A.; Cardozo, B. L.; Farshchi, R.; Oo, W. M. H.; McCluskey, M. D.; Yu, K. M.; Dubon, O. D., Ferromagnetism in Ga<sub>1-x</sub>Mn<sub>x</sub>P: Evidence for inter-Mn exchange mediated by localized holes within a detached impurity band. *Phys. Rev. Lett.* 2005, **95**, 207204.
60. Yuan, Y.; Wang, Y. T.; Khalid, M.; Gao, K.; Prucnal, S.; Gordan, O. D.; Salvan, G.; Zahn, D. R. T.; Skorupa, W.; Helm, M.; Zhou, S. Q., Ferromagnetic GaMnP Prepared by Ion Implantation and Pulsed Laser Annealing. *IEEE Trans. Magnetics* 2014, **50**, 2401304.
61. Stefanowicz, W.; Sztenkiel, D.; Faina, B.; Grois, A.; Rovezzi, M.; Devillers, T.; d'Acapito, F.; Navarro-Quezada, A.; Li, T.; Jakiela, R.; Sawicki, M.; Dietl, T.; Bonanni, A., Structural and paramagnetic properties of dilute Ga<sub>1-x</sub>Mn<sub>x</sub>N. *Phys. Rev. B* 2010, **81**, 235210.
62. Sarigiannidou, E.; Wilhelm, F.; Monroy, E.; Galera, R. M.; Bellet-Amalric, E.; Rogalev, A.; Goulon, J.; Cibert, J.; Mariette, H., Intrinsic ferromagnetism in wurtzite (Ga,Mn)N semiconductor. *Phys. Rev. B* 2006, **74**, 041306.
63. Kunert, G.; Dobkowska, S.; Li, T.; Reuther, H.; Kruse, C.; Figge, S.; Jakiela, R.; Bonanni, A.; Grenzer, J.; Stefanowicz, W.; von Borany, J.; Sawicki, M.; Dietl, T.; Hommel, D., Ga<sub>1-x</sub>Mn<sub>x</sub>N epitaxial films with high magnetization. *Appl. Phys. Lett.* 2012, **101**, 022413.
64. Wojtowicz, T.; Lim, W. L.; Liu, X.; Cywinski, G.; Kutrowski, M.; Titova, L. V.; Yee, K.; Dobrowolska, M.; Furdyna, J. K.; Yu, K. M.; Walukiewicz, W.; Kim, G. B.; Cheon, M.; Chen, X.; Wang, S. M.; Luo, H.; Vurgaftman, I.; Meyer, J. R., Growth and properties of ferromagnetic In<sub>1-x</sub>Mn<sub>x</sub>Sb alloys. *Physica E* 2004, **20**, 325-332.
65. Yanagi, S.; Kuga, K.; Slupinski, T.; Munekata, H., Carrier-induced ferromagnetic order in the narrow gap III-V magnetic alloy semiconductor (In,Mn)Sb. *Physica E* 2004, **20**, 333-337.
66. Peters, J. A.; Parashar, N. D.; Rangaraju, N.; Wessels, B. W., Magnetotransport properties of InMnSb magnetic semiconductor thin films. *Phys. Rev. B* 2010, **82**, 205207.
67. Peters, J. A.; Rangaraju, N.; Feeser, C.; Wessels, B. W., Spin-dependent magnetotransport in a p-InMnSb/n-InSb magnetic semiconductor heterojunction. *Appl. Phys. Lett.* 2011, **98**, 193506.

68. Khalid, M.; Weschke, E.; Skorupa, W.; Helm, M.; Zhou, S. Q., Ferromagnetism and impurity band in a magnetic semiconductor: InMnP. *Phys. Rev. B* 2014, **89**, 043906
69. Bonanni, A.; Sawicki, M.; Devillers, T.; Stefanowicz, W.; Faina, B.; Li, T.; Winkler, T. E.; Sztienkiel, D.; Navarro-Quezada, A.; Rovezzi, M.; Jakiela, R.; Grois, A.; Wegscheider, M.; Jantsch, W.; Suffczynski, J.; D'Acapito, F.; Meingast, A.; Kothleitner, G.; Dietl, T., Experimental probing of exchange interactions between localized spins in the dilute magnetic insulator (Ga,Mn)N. *Phys. Rev. B* 2011, **84**, 035206.
70. Clerjaud, B., Transition-Metal Impurities in III-V Compounds. *J. Phys. C: Solid State* 1985, **18**, 3615-3661.
71. Khalid, M.; Gao, K.; Weschke, E.; Hubner, R.; Baecht, C.; Gordan, O.; Salvan, G.; Zahn, D. R. T.; Skorupa, W.; Helm, M.; Zhou, S. Q., A comprehensive study of the magnetic, structural, and transport properties of the III-V ferromagnetic semiconductor InMnP. *J. Appl. Phys.* 2015, **117**, 043906.
72. Wojtowicz, T.; Cywinski, G.; Lim, W. L.; Liu, X.; Dobrowolska, M.; Furdyna, J. K.; Yu, K. M.; Walukiewicz, W.; Kim, G. B.; Cheon, M.; Chen, X.; Wang, S. M.; Luo, H., In<sub>1-x</sub>Mn<sub>x</sub>Sb - a narrow-gap ferromagnetic semiconductor. *Appl. Phys. Lett.* 2003, **82**, 4310-4312.
73. Mihaly, G.; Csontos, M.; Bordacs, S.; Kezsmarki, I.; Wojtowicz, T.; Liu, X.; Janko, B.; Furdyna, J. K., Anomalous hall effect in the (In,Mn)Sb dilute magnetic semiconductor. *Phys. Rev. Lett.* 2008, **100**, 107201.
74. Csontos, M.; Wojtowicz, T.; Liu, X.; Dobrowolska, M.; Janko, B.; Furdyna, J. K.; Mihaly, G., Magnetic scattering of spin polarized carriers in (In,Mn)Sb dilute magnetic semiconductor. *Phys. Rev. Lett.* 2005, **95**, 227203.
75. Csontos, M.; Mihaly, G.; Janko, B.; Wojtowicz, T.; Liu, X.; Furdyna, J. K., Pressure-induced ferromagnetism in (In,Mn)Sb dilute magnetic semiconductor. *Nat. Mater.* 2005, **4**, 447-449.
76. Jungwirth, T.; Sinova, J.; Wang, K. Y.; Edmonds, K. W.; Campion, R. P.; Gallagher, B. L.; Foxon, C. T.; Niu, Q.; MacDonald, A. H., Dc-transport properties of ferromagnetic (Ga,Mn)As semiconductors. *Appl. Phys. Lett.* 2003, **83**, 320-322.
77. Chun, S. H.; Kim, Y. S.; Choi, H. K.; Jeong, I. T.; Lee, W. O.; Suh, K. S.; Oh, Y. S.; Kim, K. H.; Khim, Z. G.; Woo, J. C.; Park, Y. D., Interplay between carrier and impurity concentrations in annealed Ga<sub>1-x</sub>Mn<sub>x</sub>As: Intrinsic anomalous Hall effect. *Phys. Rev. Lett.* 2007, **98**, 026601.
78. Glunk, M.; Daeubler, J.; Schoch, W.; Sauer, R.; Limmer, W., Scaling relation of the anomalous Hall effect in (Ga,Mn)As. *Phys. Rev. B* 2009, **80**, 125204.
79. Gregg, J. F.; Petej, I.; Jouguelet, E.; Dennis, C., Spin electronics. *J. Phys. D: Appl. Phys.* 2002, **35**, R121-R155.
80. Chappert, C.; Fert, A.; Van Dau, F. N., The emergence of spin electronics in data storage. *Nat. Mater.* 2007, **6**, 813-823.
81. Tanaka, M.; Higo, Y., Large tunneling magnetoresistance in GaMnAs/AlAs/GaMnAs ferromagnetic semiconductor tunnel junctions. *Phys. Rev. Lett.* 2001, **87**, 026602.
82. Chiba, D.; Matsukura, F.; Ohno, H., Tunneling magnetoresistance in (Ga,Mn)As-based heterostructures with a GaAs barrier. *Physica E* 2004, **21**, 966-969.
83. Mattana, R.; Elsen, M.; George, J. M.; Jaffres, H.; Van Dau, F. N.; Fert, A.; Wyczisk, M. F.; Olivier, J.; Galtier, P.; Lepine, B.; Guivarc'h, A.; Jezequel, G., Chemical profile and magnetoresistance of Ga<sub>1-x</sub>Mn<sub>x</sub>As/GaAs/AlAs/GaAs/Ga<sub>1-x</sub>Mn<sub>x</sub>As tunnel junctions. *Phys. Rev. B* 2005, **71**, 075206.
84. Saito, H.; Yuasa, S.; Ando, K., Origin of the tunnel anisotropic magnetoresistance in Ga<sub>1-x</sub>Mn<sub>x</sub>As/ZnSe/Ga<sub>1-x</sub>Mn<sub>x</sub>As magnetic tunnel junctions of II-VI/III-V heterostructures. *Phys. Rev.*



*Lett.* 2005, **95**, 086604.

85. Saffarzadeh, A.; Shokri, A. A., Quantum theory of tunneling magnetoresistance in GaMnAs/GaAs/GaMnAs heterostructures. *J. Magn. Magn. Mater.* 2006, **305**, 141-146.
86. Gould, C.; Ruster, C.; Jungwirth, T.; Girgis, E.; Schott, G. M.; Giraud, R.; Brunner, K.; Schmidt, G.; Molenkamp, L. W., Tunneling anisotropic magnetoresistance: A spin-valve-like tunnel magnetoresistance using a single magnetic layer. *Phys. Rev. Lett.* 2004, **93**, 117203.
87. Giraud, R.; Gryglas, M.; Thevenard, L.; Lemaitre, A.; Faini, G., Voltage-controlled tunneling anisotropic magnetoresistance of a ferromagnetic p(++)-(Ga,Mn)As/n(+)-GaAs Zener-Esaki diode. *Appl. Phys. Lett.* 2005, **87**, 2137903.
88. Ruster, C.; Gould, C.; Jungwirth, T.; Sinova, J.; Schott, G. M.; Giraud, R.; Brunner, K.; Schmidt, G.; Molenkamp, L. W., Very large tunneling anisotropic magnetoresistance of a (Ga,Mn)As/GaAs/(Ga,Mn)As stack. *Phys. Rev. Lett.* 2005, **94**, 027203.
89. Sinova, J.; Jungwirth, T.; Cerne, J., Magneto-transport and magneto-optical properties of ferromagnetic (III,Mn)V semiconductors: A review. *Intrum. J. Mod. Phys. B* 2004, **18**, 1083-1118.
90. De Ranieri, E.; Roy, P. E.; Fang, D.; Vehstedt, E. K.; Irvine, A. C.; Heiss, D.; Casiraghi, A.; Campion, R. P.; Gallagher, B. L.; Jungwirth, T.; Wunderlich, J., Piezoelectric control of the mobility of a domain wall driven by adiabatic and non-adiabatic torques. *Nat. Mater.* 2013, **12**, 808-814.
91. Chernyshov, A.; Overby, M.; Liu, X. Y.; Furdyna, J. K.; Lyanda-Geller, Y.; Rokhinson, L. P., Evidence for reversible control of magnetization in a ferromagnetic material by means of spin-orbit magnetic field. *Nat. Phys.* 2009, **5**, 656-659.
92. Endo, M.; Matsukura, F.; Ohno, H., Current induced effective magnetic field and magnetization reversal in uniaxial anisotropy (Ga,Mn)As. *Appl. Phys. Lett.* 2010, **97**, 3520514.
93. Ziegler, J. F., Srim-2003. *Nucl. Instrum. Meth. B* 2004, **219**, 1027-1036.
94. Yuan, Y.; Hübner, R.; Xu, C.; Wang, M.; Slawomir, P.; Jakiela, R.; Weschke, E.; Facsko, S.; Helm, M.; Sawicki, M.; Dietl, T.; Zhou, S., Self-assemble of Fe cations into ferromagnetic nano-lamellar structures in (In,Fe)As, to be submitted.
95. White, C. W.; Wilson, S. R.; Appleton, B. R.; Young, F. W., Supersaturated Substitutional Alloys Formed by Ion-Implantation and Pulsed Laser Annealing of Group-III and Group-V Dopants in Silicon. *J. Appl. Phys.* 1980, **51**, 738-749.
96. Ohno, Y.; Young, D. K.; Beschoten, B.; Matsukura, F.; Ohno, H.; Awschalom, D. D., Electrical spin injection in a ferromagnetic semiconductor heterostructure. *Nature* 1999, **402**, 790-792.
97. Prinz, G. A., Magnetoelectronics (vol 282, pg 1660, 1998). *Science* 1999, 283, 330-330.
98. Awschalom, D. D.; Kawakami, R. K., Magnetoelectronics - Teaching magnets new tricks. *Nature* 2000, **408**, 923-924.
99. Chiba, D.; Yamanouchi, M.; Matsukura, F.; Ohno, H., Electrical manipulation of magnetization reversal in a ferromagnetic semiconductor. *Science* 2003, **301**, 943-945.
100. Ku, K. C.; Potashnik, S. J.; Wang, R. F.; Chun, S. H.; Schiffer, P.; Samarth, N.; Seong, M. J.; Mascarenhas, A.; Johnston-Halperin, E.; Myers, R. C.; Gossard, A. C.; Awschalom, D. D., Highly enhanced Curie temperature in low-temperature annealed (Ga,Mn)As epilayers. *Appl. Phys. Lett.* 2003, **82**, 2302-2304.
101. Wang, M.; Campion, R. P.; Rushforth, A. W.; Edmonds, K. W.; Foxon, C. T.; Gallagher, B. L., Achieving high Curie temperature in (Ga,Mn)As. *Appl. Phys. Lett.* 2008, **93**, 132103.
102. Scarpulla, M. A.; Dubon, O. D.; Yu, K. M.; Monteiro, O.; Pillai, M. R.; Aziz, M. J.; Ridgway, M. C., Ferromagnetic Ga<sub>1-x</sub>Mn<sub>x</sub>As produced by ion implantation and pulsed-laser melting. *Appl. Phys. Lett.*

2003, **82**, 1251-1253.

103. Burger, D.; Zhou, S. Q.; Pandey, M.; Viswanadham, C. S.; Grenzer, J.; Roshchupkina, O.; Anwand, W.; Reuther, H.; Gottschalch, V.; Helm, M.; Schmidt, H., Application of pulsed laser annealing to ferromagnetic GaMnAs. *Phys. Rev. B* 2010, **81**, 115202.

104. Stone, P. R.; Scarpulla, M. A.; Farshchi, R.; Sharp, I. D.; Haller, E. E.; Dubon, O. D.; Yu, K. M.; Beeman, J. W.; Arenholz, E.; Denlinger, J. D.; Ohldag, H., Mn  $L_{3,2}$  X-ray absorption and magnetic circular dichroism in ferromagnetic Ga<sub>1-x</sub>Mn<sub>x</sub>P. *Appl. Phys. Lett.* 2006, **89**, 012504.

105. Bihler, C.; Kraus, M.; Brandt, M. S.; Goennenwein, S. T. B.; Opel, M.; Scarpulla, M. A.; Farshchi, R.; Estrada, D. M.; Dubon, O. D., Suppression of hole-mediated ferromagnetism in Ga<sub>1-x</sub>Mn<sub>x</sub>P by hydrogen. *J. Appl. Phys.* 2008, **104**, 013908.

106. Dubon, O. D.; Scarpulla, M. A.; Farshchi, R.; Yu, K. M., Doping and defect control of ferromagnetic semiconductors formed by ion implantation and pulsed-laser melting. *Physica B* 2006, **376**, 630-634.

107. Ohno, H.; Shen, A.; Matsukura, F.; Oiwa, A.; Endo, A.; Katsumoto, S.; Iye, Y., (Ga,Mn)As: A new diluted magnetic semiconductor based on GaAs. *Appl. Phys. Lett.* 1996, **69**, 363-365.

108. Zhou, Y. Y.; Liu, X.; Furdyna, J. K.; Scarpulla, M. A.; Dubon, O. D., Ferromagnetic resonance investigation of magnetic anisotropy in Ga<sub>1-x</sub>Mn<sub>x</sub>As synthesized by ion implantation and pulsed laser melting. *Phys. Rev. B* 2009, **80**, 224403.

109. Bihler, C.; Kraus, M.; Huebl, H.; Brandt, M. S.; Goennenwein, S. T. B.; Opel, M., Magnetocrystalline anisotropy and magnetization reversal in Ga<sub>1-x</sub>Mn<sub>x</sub>P synthesized by ion implantation and pulsed-laser melting. *Phys. Rev. B* 2007, **75**, 214419.

110. Wang, M.; Edmonds, K. W.; Gallagher, B. L.; Rushforth, A. W.; Makarovskiy, O.; Patane, A.; Campion, R. P.; Foxon, C. T.; Novak, V.; Jungwirth, T., High Curie temperatures at low compensation in the ferromagnetic semiconductor (Ga,Mn)As. *Phys. Rev. B* 2013, **87**, 121301.

111. Omiya, T.; Matsukura, F.; Dietl, T.; Ohno, Y.; Sakon, T.; Motokawa, M.; Ohno, H., Magnetotransport properties of (Ga,Mn)As investigated at low temperature and high magnetic field. *Physica E* 2000, **7**, 976-980.

112. Matsukura, F.; Ohno, H.; Shen, A.; Sugawara, Y., Transport properties and origin of ferromagnetism in (Ga,Mn)As. *Phys. Rev. B* 1998, **57**, R2037-R2040.

113. Limmer, W.; Glunk, M.; Mascheck, S.; Koeder, A.; Klarer, D.; Schoch, W.; Thonke, K.; Sauer, R.; Waag, A., Coupled plasmon-LO-phonon modes in Ga<sub>1-x</sub>Mn<sub>x</sub>As. *Phys. Rev. B* 2002, **66**, 205209.

114. Yu, K. M.; Walukiewicz, W.; Wojtowicz, T.; Denlinger, J.; Scarpulla, M. A.; Liu, X.; Furdyna, J. K., Effect of film thickness on the incorporation of Mn interstitials in Ga<sub>1-x</sub>Mn<sub>x</sub>As. *Appl. Phys. Lett.* 2005, **86**, 042102.

115. Scarpulla, M. A.; Farshchi, R.; Stone, P. R.; Chopdekar, R. V.; Yu, K. M.; Suzuki, Y.; Dubon, O. D., Electrical transport and ferromagnetism in Ga<sub>1-x</sub>Mn<sub>x</sub>As synthesized by ion implantation and pulsed-laser melting. *J. Appl. Phys.* 2008, **103**, 073913.

116. Moreno, M.; Trampert, A.; Jenichen, B.; Daweritz, L.; Ploog, K. H., Correlation of structure and magnetism in GaAs with embedded Mn(Ga)As magnetic nanoclusters. *J. Appl. Phys.* 2002, **92**, 4672-4677.

117. Khalid, M.; Prucnal, S.; Liedke, M. O.; Gao, K.; Facsko, S.; Skorupa, W.; Helm, M.; Zhou, S. Q., Synthesis and characterization of MnAs and MnP nanoclusters embedded in III-V semiconductors. *Mater. Res. Express* 2014, **1**, 026105.

118. Burger, D.; Zhou, S. Q.; Grenzer, J.; Reuther, H.; Anwand, W.; Gottschalch, V.; Helm, M.;

- Schmidt, H., The influence of annealing on manganese implanted GaAs films. *Nucl. Instrum. Meth. B* 2009, **267**, 1626-1629.
119. Bouzerar, R.; Maca, F.; Kudrnovsky, J.; Bergqvist, L., Effect of P-anion codoping on the Curie temperature of GaMnAs diluted magnetic semiconductors. *Phys. Rev. B* 2010, **82**, 035207.
120. Masek, J.; Kudrnovsky, J.; Maca, F.; Sinova, J.; MacDonald, A. H.; Campion, R. P.; Gallagher, B. L.; Jungwirth, T., Mn-doped Ga(As,P) and (Al,Ga)As ferromagnetic semiconductors: Electronic structure calculations. *Phys. Rev. B* 2007, **75**, 045202.
121. Bouzerar, R.; Bouzerar, G., Unified picture for diluted magnetic semiconductors. *Epl-Europhys. Lett.* 2010, **92**, 47006.
122. Wood, R. F.; Geist, G. A., Modeling of Nonequilibrium Melting and Solidification in Laser-Irradiated Materials. *Phys. Rev. B* 1986, **34**, 2606-2620.
123. Sawicki, M.; Stefanowicz, W.; Ney, A., Sensitive SQUID magnetometry for studying nanomagnetism. *Semicond. Sci. Technol.* 2011, **26**, 064006.
124. Lima, T. A. L.; Wahl, U.; Augustyns, V.; Silva, D. J.; Costa, A.; Houben, K.; Edmonds, K. W.; Gallagher, B. L.; Campion, R. P.; Van Bael, M. J.; da Silva, M. R.; Correia, J. G.; Araujo, J. P.; Temst, K.; Vantomme, A.; Pereira, L. M. C., Identification of the interstitial Mn site in ferromagnetic (Ga,Mn)As. *Appl. Phys. Lett.* 2015, **106**, 012406.
125. Benzeggouta, D.; Khazen, K.; Vickridge, I.; von Bardeleben, H. J.; Chen, L.; Yu, X. Z.; Zhao, J. H., Quantitative determination of the Mn site distribution in ultrathin Ga<sub>0.80</sub>Mn<sub>0.20</sub>As layers with high critical temperatures: A Rutherford backscattering channeling investigation. *Phys. Rev. B* 2014, **89**, 115323.
126. Limmer, W.; Glunk, M.; Schoch, W.; Koder, A.; Kling, R.; Sauer, R.; Waag, A., Micro-Raman scattering study of Ga<sub>1-x</sub>Mn<sub>x</sub>As. *Physica E* 2002, **13**, 589-592.
127. Islam, M. R.; Chen, N. F.; Yamada, M., Raman scattering study on Ga<sub>1-x</sub>Mn<sub>x</sub>As prepared by Mn ions implantation, deposition and post-annealing. *Cryst. Res. Technol.* 2009, **44**, 215-220.
128. Irmer, G.; Wenzel, M.; Monecke, J., Light scattering by a multicomponent plasma coupled with longitudinal-optical phonons: Raman spectra of p-type GaAs:Zn. *Phys. Rev. B* 1997, **56**, 9524-9538.
129. Pastor, D.; Olea, J.; Toledano-Luque, M.; Martil, I.; Gonzalez-Diaz, G.; Ibanez, J.; Cusco, R.; Artus, L., Laser thermal annealing effects on single crystal gallium phosphide. *J. Appl. Phys.* 2009, **106**, 053510.
130. Vitali, G.; Pizzuto, C.; Zollo, G.; Karpuzov, D.; Kalitzova, M.; van der Heide, P.; Scamarcio, G.; Spagnolo, V.; Chiavarone, L.; Manno, D., Structural reordering and electrical activation of ion-implanted GaAs and InP due to laser annealing in a controlled atmosphere. *Phys. Rev. B* 1999, **59**, 2986-2994.
131. Newville, M., IFEFFIT: interactive XAFS analysis and FEFF fitting. *J. Synchrotron Radiat.* 2001, **8**, 322-324.
132. Ravel, B.; Newville, M., ATHENA, ARTEMIS, HEPHAESTUS: data analysis for X-ray absorption spectroscopy using IFEFFIT. *J. Synchrotron Radiat* 2005, **12**, 537-541.
133. Ankudinov, A. L.; Ravel, B.; Rehr, J. J.; Conradson, S. D., Real-space multiple-scattering calculation and interpretation of x-ray-absorption near-edge structure. *Phys. Rev. B* 1998, **58**, 7565-7576.
134. Dietl, T.; Sato, K.; Fukushima, T.; Bonanni, A.; Jamet, M.; Barski, A.; Kuroda, S.; Tanaka, M.; Hai, P. N.; Katayama-Yoshida, H., Spinodal nanodecomposition in semiconductors doped with transition metals. *Rev. Mod. Phys.* 2015, **87**, 1311-1377.

135. Dietl, T., A ten-year perspective on dilute magnetic semiconductors and oxides. *Nat. Mater.* 2010, **9**, 965-974.
136. Burch, K. S.; Awschalom, D. D.; Basov, D. N., Optical properties of III-Mn-V ferromagnetic semiconductors. *J. Magn. Magn. Mater.* 2008, **320**, 3207-3228.
137. Yamanouchi, M.; Chiba, D.; Matsukura, F.; Ohno, H., Current-induced domain-wall switching in a ferromagnetic semiconductor structure. *Nature* 2004, **428**, 539-542.
138. Adam, J. P.; Vernier, N.; Ferre, J.; Thiaville, A.; Jeudy, V.; Lemaitre, A.; Thevenard, L.; Faini, G., Nonadiabatic spin-transfer torque in (Ga,Mn)As with perpendicular anisotropy. *Phys. Rev. B* 2009, **80**, 193204.
139. Wang, K. Y.; Edmonds, K. W.; Irvine, A. C.; Tataru, G.; De Ranieri, E.; Wunderlich, J.; Olejnik, K.; Rushforth, A. W.; Champion, R. P.; Williams, D. A.; Foxon, C. T.; Gallagher, B. L., Current-driven domain wall motion across a wide temperature range in a (Ga,Mn)(As,P) device. *Appl. Phys. Lett.* 2010, **97**, 262102.
140. Gorchon, J.; Curiale, J.; Lemaitre, A.; Moisan, N.; Cubukcu, M.; Malinowski, G.; Ulysse, C.; Faini, G.; von Bardeleben, H. J.; Jeudy, V., Stochastic Current-Induced Magnetization Switching in a Single Semiconducting Ferromagnetic Layer. *Phys. Rev. Lett.* 2014, **112**, 026601.
141. Rushforth, A. W.; Wang, M.; Farley, N. R. S.; Champion, R. P.; Edmonds, K. W.; Staddon, C. R.; Foxon, C. T.; Gallagher, B. L., Molecular beam epitaxy grown (Ga,Mn)(As,P) with perpendicular to plane magnetic easy axis. *J. Appl. Phys.* 2008, **104**, 073908.
142. Cubukcu, M.; von Bardeleben, H. J.; Khazen, K.; Cantin, J. L.; Mauguin, O.; Largeau, L.; Lemaitre, A., Adjustable anisotropy in ferromagnetic (Ga,Mn)(As,P) layered alloys. *Phys. Rev. B* 2010, **81**, 041202.
143. Glunk, M.; Daeubler, J.; Dreher, L.; Schwaiger, S.; Schoch, W.; Sauer, R.; Limmer, W.; Brandlmaier, A.; Goennenwein, S. T. B.; Bihler, C.; Brandt, M. S., Magnetic anisotropy in (Ga,Mn)As: Influence of epitaxial strain and hole concentration. *Phys. Rev. B* 2009, **79**, 195206.
144. Takamura, K.; Matsukura, F.; Chiba, D.; Ohno, H., Magnetic properties of (Al,Ga,Mn)As. *Appl. Phys. Lett.* 2002, **81**, 2590-2592.
145. Edmonds, K. W.; van der Laan, G.; Farley, N. R. S.; Arenholz, E.; Champion, R. P.; Foxon, C. T.; Gallagher, B. L., Strain dependence of the Mn anisotropy in ferromagnetic semiconductors observed by X-ray magnetic circular dichroism. *Phys. Rev. B* 2008, **77**, 113205.
146. Casiraghi, A.; Rushforth, A. W.; Wang, M.; Farley, N. R. S.; Wadley, P.; Hall, J. L.; Staddon, C. R.; Edmonds, K. W.; Champion, R. P.; Foxon, C. T.; Gallagher, B. L., Tuning perpendicular magnetic anisotropy in (Ga,Mn)(As,P) by thermal annealing. *Appl. Phys. Lett.* 2010, **97**, 122504
147. Vurgaftman, I.; Meyer, J. R.; Ram-Mohan, L. R., Band parameters for III-V compound semiconductors and their alloys. *J. Appl. Phys.* 2001, **89**, 5815-5875.
148. Munekata, H.; Ohno, H.; Vonmolnar, S.; Segmuller, A.; Chang, L. L.; Esaki, L., Diluted Magnetic III-V Semiconductors. *Phys. Rev. Lett.* 1989, **63**, 1849-1852.
149. Fritzsche, C. R.; Rothemund, W., Sputtering during Ion-Implantation into Gallium-Arsenide. *Appl. Phys.* 1975, **7**, 39-44.
150. Korzhavyi, P. A.; Abrikosov, I. A.; Smirnova, E. A.; Bergqvist, L.; Mohn, P.; Mathieu, R.; Svedlindh, P.; Sadowski, J.; Isaev, E. I.; Vekilov, Y. K.; Eriksson, O., Defect-induced magnetic structure in (Ga<sub>1-x</sub>Mn<sub>x</sub>)As. *Phys. Rev. Lett.* 2002, **88**, 187202.
151. Liu, X.; Lim, W. L.; Titova, L. V.; Dobrowolska, M.; Furdyna, J. K.; Kutrowski, M.; Wojtowicz, T., Perpendicular magnetization reversal, magnetic anisotropy, multistep spin switching, and domain

- nucleation and expansion in  $\text{Ga}_{1-x}\text{Mn}_x\text{As}$  films. *J. Appl. Phys.* 2005, **98**, 063904.
152. Wellmann, P. J.; Garcia, J. M.; Feng, J. L.; Petroff, P. M., Formation of nanoscale ferromagnetic MnAs crystallites in low-temperature grown GaAs. *Appl. Phys. Lett.* 1997, **71**, 2532-2534.
153. Ando, K.; Chiba, A.; Tanoue, H., Uniaxial magnetic anisotropy of submicron MnAs ferromagnets in GaAs semiconductors. *Appl. Phys. Lett.* 1998, **73**, 387-389.
154. Edmonds, K. W.; Farley, N. R. S.; Champion, R. P.; Foxon, C. T.; Gallagher, B. L.; Johal, T. K.; van der Laan, G.; MacKenzie, M.; Chapman, J. N.; Arenholz, E., Surface effects in Mn  $L_{3,2}$  X-ray absorption spectra from (Ga,Mn)As. *Appl. Phys. Lett.* 2004, **84**, 4065-4067.
155. Edmonds, K. W.; van der Laan, G.; Freeman, A. A.; Farley, N. R. S.; Johal, T. K.; Champion, R. P.; Foxon, C. T.; Gallagher, B. L.; Arenholz, E., Angle-dependent X-ray magnetic circular dichroism from (Ga,Mn)As: Anisotropy and identification of hybridized states. *Phys. Rev. Lett.* 2006, **96**, 117207.
156. Wadley, P.; Casiraghi, A.; Wang, M.; Edmonds, K. W.; Champion, R. P.; Rushforth, A. W.; Gallagher, B. L.; Staddon, C. R.; Wang, K. Y.; van der Laan, G.; Arenholz, E., Polarized X-ray spectroscopy of quaternary ferromagnetic semiconductor (Ga,Mn)(As,P) thin films. *Appl. Phys. Lett.* 2011, **99**, 022502.
157. Kaminski, A.; Das Sarma, S., Polaron percolation in diluted magnetic semiconductors. *Phys. Rev. Lett.* 2002, **88**, 247202
158. Mayr, M.; Alvarez, G.; Dagotto, E., Global versus local ferromagnetism in a model for diluted magnetic semiconductors studied with Monte Carlo techniques. *Phys. Rev. B* 2002, **65**, 241202.
159. Sheu, B. L.; Myers, R. C.; Tang, J. M.; Samarth, N.; Awschalom, D. D.; Schiffer, P.; Flatte, M. E., Onset of ferromagnetism in low-doped  $\text{Ga}_{1-x}\text{Mn}_x\text{As}$ . *Phys. Rev. Lett.* 2007, **99**, 227205.
160. Dietl, T., Interplay between carrier localization and magnetism in diluted magnetic and ferromagnetic semiconductors. *J. Phys. Soc. Jpn.* 2008, **77**, 031005
161. Richardella, A.; Roushan, P.; Mack, S.; Zhou, B.; Huse, D. A.; Awschalom, D. D.; Yazdani, A., Visualizing Critical Correlations Near the Metal-Insulator Transition in  $\text{Ga}_{1-x}\text{Mn}_x\text{As}$ . *Science* 2010, **327**, 665-669.
162. Kobayashi, M.; Muneta, I.; Takeda, Y.; Harada, Y.; Fujimori, A.; Krempasky, J.; Schmitt, T.; Ohya, S.; Tanaka, M.; Oshima, M.; Strocov, V. N., Unveiling the impurity band induced ferromagnetism in the magnetic semiconductor (Ga,Mn)As. *Phys. Rev. B* 2014, **89**, 205204.
163. Souma, S.; Chen, L.; Oszwaldowski, R.; Sato, T.; Matsukura, F.; Dietl, T.; Ohno, H.; Takahashi, T., Fermi level position, Coulomb gap, and Dresselhaus splitting in (Ga,Mn)As. *Sci. Rep.* 2016, **6**, 27266.
164. Kanski, J.; Ilver, L.; Karlsson, K.; Ulfat, I.; Leandersson, M.; Sadowski, J.; Di Marco, I., Electronic structure of (Ga,Mn)As revisited. *New journal of Physics* 2017, **19**, 023006.
165. Ohya, S.; Takata, K.; Tanaka, M., Nearly non-magnetic valence band of the ferromagnetic semiconductor GaMnAs. *Nat. Phys.* 2011, **7**, 342-347.
166. Myers, R. C.; Sheu, B. L.; Jackson, A. W.; Gossard, A. C.; Schiffer, P.; Samarth, N.; Awschalom, D. D., Antisite effect on hole-mediated ferromagnetism in (Ga,Mn)As. *Phys. Rev. B* 2006, **74**, 155203.
167. Abrahams, E., 50 Years of Anderson Localization 2010.
168. Cho, Y. J.; Scarpulla, M. A.; Liu, X.; Zhou, Y. Y.; Dubon, O. D.; Furdyna, J. K., Magnetic cluster phases of Mn-interstitial-free (Ga,Mn)As. *AIP Conf. Proc.* 2007, **893**, 1221.
169. Wadley, P.; Freeman, A. A.; Edmonds, K. W.; van der Laan, G.; Chauhan, J. S.; Champion, R. P.; Rushforth, A. W.; Gallagher, B. L.; Foxon, C. T.; Wilhelm, F.; Smekhova, A. G.; Rogalev, A., Element-resolved orbital polarization in (III,Mn)As ferromagnetic semiconductors from K-edge X-ray magnetic circular dichroism. *Phys. Rev. B* 2010, **81**, 235208.

170. Sliwa, C.; Dietl, T., Orbital magnetization in dilute ferromagnetic semiconductors. *Phys Rev B* 2014, **90**, 045202.
171. Linnarsson, M.; Janzen, E.; Monemar, B.; Kleverman, M.; Thilderkvist, A., Electronic structure of the GaAs:Mn-Ga center. *Phys. Rev. B* 1997, **55**, 6938-6944.
172. Oiwa, A.; Katsumoto, S.; Endo, A.; Hirasawa, M.; Iye, Y.; Ohno, H.; Matsukura, F.; Shen, A.; Sugawara, Y., Nonmetal-metal-nonmetal transition and large negative magnetoresistance in (Ga,Mn)As/GaAs. *Solid State Commun.* 1997, **103**, 209-213.
173. Matsukura, F.; Sawicki, M.; Dietl, T.; Chiba, D.; Ohno, H., Magnetotransport properties of metallic (Ga,Mn)As films with compressive and tensile strain. *Physica E* 2004, **21**, 1032-1036.
174. Schneider, J.; Kaufmann, U.; Wilkening, W.; Baeumler, M.; Kohl, F., Electronic-Structure of the Neutral Manganese Acceptor in Gallium-Arsenide. *Phys. Rev. Lett.* 1987, **59**, 240-243.
175. Dietl, T.; Ohno, H.; Matsukura, F., Hole-mediated ferromagnetism in tetrahedrally coordinated semiconductors. *Phys. Rev. B* 2001, **63**, 195205
176. Schallenberg, T.; Munekata, H., Preparation of ferromagnetic (In,Mn)As with a high Curie temperature of 90 K. *Appl. Phys. Lett.* 2006, **89**, 042507
177. Dietl, T., Hole states in wide band-gap diluted magnetic semiconductors and oxides. *Phys. Rev. B* 2008, **77**, 085208.

## Appendix A

# Publication list

### Thesis-related:

- [1] Y. Yuan, Y. Wang, M. Khalid, K. Gao, S. Prucnal, O. D. Gordan, G. Salvan, D. R. T. Zahn, W. Skorupa, M. Helm, and S. Zhou, Ferromagnetic GaMnP prepared by Ion implantation and pulsed laser annealing, *IEEE Trans. Magnetics*, **50**, 2401304 (2014).
- [2] Y. Yuan, Y. Wang, K. Gao, M. Khalid, C. Wu, W. Zhang, F. Munnik, E. Weschke, C. Baehtz, W. Skorupa, M. Helm, S. Zhou, High Curie temperature and perpendicular magnetic anisotropy in homoepitaxial InMnAs films, *J. Phys D: Appl. Phys.*, **48**, 235002 (2015).
- [3] Y. Yuan, R. Hübner, F. Liu, M. Sawicki, O. Gordan, G. Salvan, D. R. T. Zahn, D. Banerjee, C. Baehtz, M. Helm, and S. Zhou, Ferromagnetic Mn-implanted GaP: Microstructures vs magnetic properties, *ACS Appl. Mater. Interfaces*, **8**, 3912-3918 (2016).
- [4] Y. Yuan, C. Xu, R. Hübner, R. Jakiela, R. Böttger, T. Dietl, M. Helm, M. Sawicki, and S. Zhou, Interplay between localization and magnetism in (Ga,Mn)As and (In,Mn)As, *Phys. Rev. Materials*, **1**, 054401 (2017).

## Non-thesis-related:

- [1] L. Li, Y. Yuan, Y. Zhang, T. Namiki, K. Nishimura, R. Pottgen, and S. Zhou, Giant low field magnetocaloric effect and field-induced metamagnetic transition in TmZn, *Appl. Phys. Lett.*, **107**, 132401 (2015).
- [2] L. Li, Y. Yuan, Y. Zhang, R. Pottgen, and S. Zhou, Magnetic phase transitions and large magnetic entropy change with a wide temperature span in HoZn, *J. Alloy Comp.*, **643**, 147-151 (2015).
- [3] L. Li, Y. Yuan, C. Xu, Y. Qi, and S. Zhou, Observation of large magnetocaloric effect in equiatomic binary compound ErZn, *AIP Advances*, **7**, 056401 (2017).
- [4] S. Zhou, L. Li, Y. Yuan, A. W. Rushforth, L. Chen, Y. Wang, R. Böttger, R. Heller, J. Zhao, K. W. Edmonds, R. P. Champion, B. L. Gallagher, C. Timm, and M. Helm, Precise tuning of the Curie temperature of (Ga,Mn)As-based magnetic semiconductors by hole compensation: Support for valence-band ferromagnetism, *Phys. Rev. B*, **94**, 075205 (2016).
- [5] L. Meng, C. Xu, Y. Yuan, Y. Qi, S. Zhou and L. Li, Magnetic properties and giant reversible magnetocaloric effect in GdCoC<sub>2</sub>, *RSC Adv.*, **6**, 74765 (2016).
- [6] M. Xu, K. Gao, J. Wu, H. Cai, Y. Yuan, S. Prucnal, R. Hübner, W. Skorupa, M. Helm, and S. Zhou, Polycrystalline ZnTe thin film on silicon synthesized by pulsed laser deposition and subsequent pulsed laser melting, *Mater. Res. Express*, **3**, 036403 (2016).
- [7] X. Pan, Y. Shuai, C. Wu, W. Luo, X. Sun, Y. Yuan, S. Zhou, X. Ou, and W. Zhang, Resistive switching behavior in single crystal SrTiO<sub>3</sub> annealed by laser, *Appl. Surf. Sci.*, **389**, 1104-1107 (2016).
- [8] F. Liu, S. Prucnal, R. Hübner, Y. Yuan, W. Skorupa, M. Helm, and S. Zhou, Suppressing the cellular breakdown in silicon supersaturated with titanium, *J. Phys. D: Appl. Phys.*, **49**, 245104 (2016).
- [9] E. Gan'shina, L. Golik, Z. Kun'kova, I. Bykov, A. Novikov, A. Rukovishnikov, Y. Yuan, G. Zykov, R. Böttger, and S. Zhou, Transversal Kerr effect of In<sub>1-x</sub>Mn<sub>x</sub>As layers prepared by ion implantation followed by pulsed laser annealing, *Jpn. J. Appl. Phys.*, **55**, 07MF02 (2016).
- [10] Y. Liu, S. Prucnal, S. Zhou, Z. Li, L. Guo, X. Chen, Y. Yuan, F. Liu, and M. Helm, Intrinsic diamagnetism in the Weyl semimetal TaAs, *J. Magn. Magn. Mater.*, **408**, 73-76 (2016).
- [11] Y. Liu, R. Pan, X. Zhang, J. Han, Q. Yuan, Y. Tian, Y. Yuan, F. Liu, Y. Wang, A. T. N'Diaye, E. Arenholz, X. Chen, Y. Sun, B. Song, and S. Zhou,



Vacancy defect complexes in silicon: Charges and spin order, *Phys. Rev. B*, **94**, 195204 (2016).

- [12] Y. Liu, Y. Yuan, F. Liu, R. Böttger, W. Anwand, Y. Wang, A. Semisalova, A. Ponomaryov, X. Lu, A. T. N'Diaye, E. Arenholz, V. Heera, W. Skorupa, M. Helm, S. Zhou, Interaction between magnetic moments and itinerant carriers in *d*0 ferromagnetic SiC, *Phys. Rev. B*, **95**, 195309 (2017)

## **Appendix B**

# **Curriculum Vitae**

## **B.1 Personal data**

Name: Ye Yuan

Birthday: 23. Nov. 1987

Birth place: Heilongjiang, China

## **B.2 Education**

Aug. 2007 - Jul. 2011 Bachelor of Engineering

Harbin Institute of Technology, China

Aug. 2011 - Jul. 2013 Master of Engineering

Harbin Institute of Technology, China

Oct. 2013 - Jul. 2017 PhD student

Helmholtz-Zentrum Dresden-Rossendorf  
Technische Universität Dresden